VIETNAM NATIONAL UNIVERSITY
UNIVERSITY OF SCIENCE

Duong Thi Thanh Nhan

INVESTIGATION OF THE CRYSTAL STRUCTURE AND CRITICAL PARAMETERS OF MgB_2 SUPERCONDUCTORS THROUGH ADDITION AND ION IRRADIATION

DISSERTATION FOR DOCTOR OF PHILOSOPHY IN PHYSICS

Hanoi - 2026

VIETNAM NATIONAL UNIVERSITY

UNIVERSITY OF SCIENCE

Duong Thi Thanh Nhan

INVESTIGATION OF CRYSTAL STRUCTURE AND CRITICAL PARAMETERS OF MgB_2 SUPERCONDUCTORS THROUGH ADDITION AND ION IRRADIATION

Major: Thermal Physics

Code: 9440102.07

DISSERTATION FOR DOCTOR OF PHILOSOPHY IN PHYSICS

SUPERVISOR: Assoc.Prof. Dr. Tran Hai Duc

Hanoi - 2026

DECLARATION

I hereby declare that this research is my own work. The results written in collaboration with other authors have been approved by the co-authors prior to being included in the dissertation. The results presented in the dissertation are truthful and have not been published in any other works.

Author

Duong Thi Thanh Nhan

In loving memory of my beloved elders,
Phan Trung Thành and Dương Phúc Điểu

This dissertation is dedicated to my late father-in-law and my late uncle, whose unwavering faith gave me the courage to return to academia. Beyond its scientific focus on superconductivity, this work is a heartfelt tribute offered to both of them with my deepest respect, gratitude, and love.

Thank you for the strength, determination, and quiet encouragement you gave me. Your love continues to guide my path, even in your absence.

ACKNOWLEDGMENTS

Pursuing a doctoral degree has been a profound commitment. While the journey brought unforeseen obstacles, I was fortunate to be guided by an exceptional supervisor and supported by wonderful colleagues. Their mentorship and collaboration have been instrumental in advancing my knowledge and developing my capacity for independent research.

First, I wish to extend my deepest and most heartfelt gratitude to my supervisor, Assoc. Prof. Dr. Tran Hai Duc, at Faculty of Physics, VNU - University of Science. I have been incredibly fortunate to benefit from his exceptional guidance, unwavering support, and invaluable insights, which enabled me to bring this dissertation to fruition. His incisive comments and constructive critiques not only shaped the direction of my research but also elevated my standards as a researcher. I am truly grateful for the dedication and mentorship he so generously offered throughout this journey.

Second, I would like to express my profound gratitude to the esteemed members of my dissertation committee. Beyond their precise feedback and rigorous assessment, their constructive suggestions served as an invaluable source of academic enlightenment. The expertise and dedication they brought to evaluating my work not only elevated the quality of this dissertation to its highest potential but also provided me with profound lessons that will inspire my future scientific endeavors

Third, I would like to extend my sincere gratitude to my lab-mates, colleagues, and friends, whose enthusiasm and invaluable support significantly aided my research. I am also deeply grateful to the faculty members and staff across the various functional departments. In particular, I am deeply grateful to Dr. Le Minh Tien (Hanoi University of Science and Technology), as well as Prof. Nguyen Hoang Nam, Dr. Pham The An, Dr. Nguyen The Nghia and Dr. Nguyen Thanh Binh (VNU University of Science) for providing essential administrative and technical assistance. Furthermore, I highly value the fruitful collaboration with the research groups of Prof.

Tuson Park (Sungkyunkwan University, Korea); Prof. Soo-Kien Chen (University Putra Malaysia, Malaysia). Their generous assistance has been crucial in facilitating the successful completion of my doctoral program. Additionally, this work is funded by Vietnam National Foundation for Science and Technology Development (NAFOSTED) under grant number 103.02-2023.78, and I would like to thank them for sponsoring my research.

Lastly, I wish to express my deepest gratitude to my family for their unconditional support, constant encouragement, and spiritual strength throughout this challenging journey. Their enduring love has been a profound source of motivation for me to overcome every obstacle and achieve my goals. Words cannot fully express my gratitude for the sacrifices they made and their unwavering confidence in me.

Hanoi, 2026

Duong Thi Thanh Nhan

CONTENTS

DECLARATION

ACKNOWLEDGMENTS

LIST OF NOTATIONS AND ABBREVIATIONS 3

LIST OF TABLES 4

LIST OF FIGURES 5

INTRODUCTION 8

CHAPTER 1. LITERATURE OVERVIEW 12

1.1 Superconductors 13

1.2 Several important theoretical models applied for superconductors 21

1.3 Overview on MgB_2 superconductor 27

1.4 Motivation 39

CHAPTER 2. EXPERIMENTS 41

2.1 Sample fabrications 41

2.2 Fabrication of MgB_2 films 44

2.3 Sample investigations 48

2.4 Conclusion of chapter 2 52

CHAPTER 3. ENHANCEMENTS OF SUPERCONDUCTING PROPERTIES IN MAGNESIUM DIBORIDE BY CO-ADDITION OF MAGNESIUM AND SILICON CARBIDE 53

3.1 Investigation of critical temperature in (SiC + Mg + MgB_2) bulks 56

3.2 Enhancements of upper critical fields of (SiC + Mg + MgB_2) bulks 59

3.3 Enhancements of critical current density in (SiC + Mg + MgB_2) bulks 61

3.4 Pinning mechanism in the pure and (SiC + Mg + MgB_2) bulks 63

3.5 Conclusion of chapter 3 66

CHAPTER 4. INVESTIGATION OF THE CRYSTAL STRUCTURE AND SUPERCONDUCTING PROPERTIES IN MAGNESIUM DIBORIDE USING IRRADIATION OF NIOBIUM IONS 67

4.1 Simulation of the Nb-irradiation processes 70

4.2 Variations of the crystal structure in MgB_2 films before and after irradiation by Nb ions 72

4.4 Superconductivity of pristine and Nb-ion irradiated MgB_2 films..... 81

4.5. Conclusions of chapter 4 90

CHAPTER 5. INVESTIGATION OF THE CRYSTAL STRUCTURE AND SUPERCONDUCTING PROPERTIES IN MAGNESIUM DIBORIDE USING IRRADIATION OF NICKEL IONS 91

5.1. Simulation of the Ni-irradiation processes 94

5.2. Variations of the crystal structure in MgB_2 films before and after irradiation by Ni ions 96

5.3 Superconductivity of pristine and Ni-ion irradiated MgB_2 films 102

5.4. The best enhancement of J_c in MgB_2 bulks and films 110

5.5. Conclusions of chapter 5 112

CONCLUSIONS..... 114

LIST OF PUBLICATIONS..... 116

REFERENCES..... 117

LIST OF NOTATIONS AND ABBREVIATIONS

Notations	Explain
ξ_c	*c*-axis coherence length
λ	penetration depth
$\lambda_{Cu\text{-}K\alpha}$	Cu-K_α radiation wavelength
J_c	critical current density
J	normalized critical current density ($j = J_c/J_c\ (0)$)
J_{sv}	critical current density in single vortex regime
T_c	critical temperature
EPC	electron-phonon coupling
FWHM	full width at half maximum
ΔM	magnetization hysteresis width
B_{irr}	irreversibility field
B_{c1}	lower critical field
B_{c2}	upper critical field
F_L	Lorentz force density
F_p	pinning force density
$F_{p,max}$	maximum value of pinning force density
f_p	normalized pinning force density ($f_p = F_p/F_{p,max}$)
b_{peak}	normalized field at maximum of flux pinning force density
κ	Ginzburg–Landau parameter
HTS	high temperature superconductor
HPCVD	hybrid physical-chemical vapor deposition
PCs	pining centers
PPMS	physical property measurement system

LIST OF TABLES

Table 1.1. Details of pinning mechanism in type II superconductors. [19] *27*
Table 2.1. The series of MgB_2 bulks and fabricated conditions *44*
Table 2.2. Conditions for fabricating of pristine MgB_2 thin films *47*
Table 2.3. Ni-ions and Nb-ions irradiated MgB_2 films and ion doses details *48*
Table 3.1. The series of bulk MgB_2 and fabrication conditions *55*
Table 3.2. T_c and B_{c2} of pure and (SiC + Mg + MgB_2) bulks *61*
Table 4.1. Name of films and the doses for Nb-ion irradiations *71*
Table 4.2. The results of calculated the c-axis parameters *74*
Table 4.3. The results of calculating the tensile strain (ε) *76*
Table 4.4. Values of Raman peak centers, FWHM of E_{2g} peak, electron-phonon coupling, and Θ_D of the pristine and Nb-ion irradiated MgB_2 films *81*
Table 4.5. T_c of pristine and Nb-ion irradiated MgB_2 films *83*
Table 4.6. The β values for pristine and Nb-ion irradiated MgB_2 films *87*
Table 5.1. Name of films and the doses for Ni-ion irradiations *92*
Table 5.2. The results of calculating the c-axis parameters *98*
Table 5.3. Values of Raman peak centers, FWHM of E_{2g} peak, electron-phonon coupling, and Θ_D of the pristine and Ni-ion irradiated MgB_2 films *102*
Table 5.4. T_c of pristine and Ni-ion irradiated MgB_2 films *104*
Table 5.5. T_c in the recent work using Fe magnetic-ions [102] *105*
Table 5.6. The β values for pristine and Ni-ion irradiated MgB_2 films *108*

LIST OF FIGURES

***Figure 1.1**. The critical temperatures of superconductors from 1900 to 2020..... 16*

***Figure 1.2.** Critical surfaces of (a) type-I, (b) type-II superconductors [18]..... 18*

***Figure 1.3.** 3D picture of vortex matter (red) in defect structures (yellow) with different dimensions [61] 19*

***Figure 1.4.** Illustration of dissipation caused by migrating vortices in homogeneous superconductors [61] 21*

***Figure 1.5.** Schematic of field dependence of collective pinning regimes in type-II superconductors. [8] 22*

***Figure 1.6.** The hexagonal structure pure MgB_2 [75] 28*

***Figure 1.7**. The Fermi surface of MgB_2 [74] 29*

***Figure 1.8.** The temperature dependence of resistivity and magnetic susceptibility (inset). [74] 30*

***Figure 1.9**. The magnetic field dependence of J_c for in-situ MgB_2 ..... 32*

***Figure 1.10.** Field dependence of J_c for pure and ZnO-buffered MgB_2 films at (a) 5 K and (b) 20 K 34*

***Figure 1.11**. Magnetic field dependence of J_c for pure and SiC-buffered MgB_2 films. 35*

***Figure 1.12.** Enhancements of J_c in MgB_2 films using the O-ion irradiation. [82] 36*

***Figure 1.13.** Enhanced field performance of J_c in irradiated MB400nm and MB800nm films..... 37*

***Figure 1.14**. Enhancements of J_c in MgB_2 films by using the Co-ion irradiation. [43] 39*

***Figure 2.1.** Scheme of fabrication of pure MgB_2 bulks..... 41*

***Figure 2.2**. Scheme of fabrication of (Mg + MgB_2) bulks 42*

***Figure 2.3.** Scheme of fabrication of (y wt.% SiC + Mg + MgB_2) bulks..... 43*

***Figure 2.4**. The scheme of fabricating MgB_2 films in the chamber..... 45*

***Figure 2.5.** The HUS-5SDH-2 tandem pelletron accelerator system 48*

Figure 3.1. *Plot of in-field resistivity versus temperature of MgB_2 bulks 57*

Figure 3.2. *Normalized zero-field resistivity ($\rho/\rho_{40\,K}$) versus temperature of the MgB_2 bulks..... 58*

Figure 3.3. *The $Bc2$ versus temperature for pure and (SiC + Mg + MgB_2) bulks.. 60*

Figure 3.4. *J_c of pure and (SiC + Mg + MgB_2) bulks at 10 K, 15 K, 25 K, and 30 K 62*

Figure 3.5. *Normalized pinning force density $fp = Fp/Fp,max$ versus reduced field b ($b = B/Bpeak$) of pure and (SiC + Mg + MgB_2) bulks at 15 K..... 63*

Figure 3.6. *Flux-pinning mechanism in pure and (SiC + Mg + MgB_2) bulks fitted by Dew-Hughes model..... 65*

Figure 4.1. *(a) Mean projected range and (b) vacancy depth profile for 1 MeV Nb-ion irradiated MgB_2 film on c-cut Al_2O_3 substrate..... 70*

Figure 4.2. *XRD diagram of the pristine and Nb-ion irradiated MgB_2 films..... 72*

Figure 4.3. *AFM images: (a) pristine and (b) Nb-5E13 films..... 76*

Figure 4.4. *Raman spectroscopy and parameter analysis of pristine and Nb-irradiated MgB_2 films..... 78*

Figure 4.5. *Magnetization versus temperature (M-T) curves of the pristine and Nb-ion irradiated MgB_2 films. 81*

Figure 4.6. *J_c versus magnetic field of pristine and Nb-ion irradiated MgB_2 films measured at (a) 7 K, (b) 10 K, (c) 15 K, (d) 20 K, (e) 25 K and (f) 30 K..... 84*

Figure 4.7. *Double logarithmic scaled field dependence of evolution of the J_c under applied magnetic field for Nb-ion irradiated MgB_2 films 86*

Figure 4.8. *Plot of normalized volume pinning force f_p, on normalized field b of the pristine and Nb-ion irradiated $MgB2$ films..... 88*

Figure 5.1. *(a) Mean projected range and (b) vacancy depth profile for 1 MeV Ni-ion irradiated MgB_2 film on c-cut Al_2O_3 substrate..... 95*

Figure 5.2. *XRD diagram of the pristine and Ni-ion irradiated MgB_2 films..... 96*

Figure 5.3. *AFM images: (a) pristine and (b) Ni-5E13 films..... 98*

Figure 5.4. *Raman spectroscopy and parameter analysis of pristine and Ni-irradiated MgB_2 films 100*
Figure 5.5. *Magnetization versus temperature (M-T) curves of the pristine and Ni-ion irradiated MgB_2 films, ... 103*
Figure 5.6. *J_c versus magnetic field of the pristine and Ni-ion irradiated MgB_2 films (a) 5 K, (b) 20 K 105*
Figure 5.7. *Variations of J_c at 5 K (a) and 20 K (b) with increasing Ni-ion dose across different fields, showing high-field enhancements 106*
Figure 5.8. *Double logarithmic scaled field dependence of evolution of the J_c under applied magnetic field for Ni-ion irradiated MgB_2 films 107*
Figure 5.9. *Plot of normalized volume pinning force f_p 109*
Figure 5.10. *The best enhancements of J_c in MgB_2 bulks and films at 10 K..... 111*

INTRODUCTION

a. Rationale for topic selection

Discovered in 2001 as a superconductor with a critical temperature (T_c) of ~39 K, magnesium diboride (MgB_2) has attracted widespread attention. This compound is a promising candidate for practical applications including MRI, superconducting fault current limiters (SFCLs), and cryogenic power transmission. Compared to standard low-temperature superconductors (e.g., NbTi and Nb_3Sn), MgB_2 offers a higher T_c, lower anisotropy, and easier processing. Consequently, it enables operation in the intermediate 20 - 30 K range using compact cryocoolers, removing the need for liquid helium. Despite these advantages, the widespread use of MgB_2 remains limited by two intrinsic challenges: (i) the rapid decrease of critical current density (J_c) under applied magnetic fields due to weak flux pinning, and (ii) the relatively low upper critical field (B_{c2}) compared with more complex high-temperature superconductors. These limitations restrict the performance of MgB_2 conductors in high-field environments. Therefore, much research effort has been directed toward improving flux pinning strength and enhancing B_{c2} while maintaining a sufficiently high T_c and good grain connectivity.

Two complementary strategies have proven particularly effective in this regard: addition and ion irradiation. Addition with carbon or carbon-containing compounds (such as SiC, carbon nanotubes, or graphene oxide) can substitute boron sites in the MgB_2 lattice, increasing electron scattering and lattice strain. This substitution effectively enhances B_{c2} and the irreversibility field (B_{irr}) while generating nanoscale pinning centers. However, over-doping may lead to the formation of secondary phases and a decline in T_c. On the other hand, controlled ion irradiation may introduce artificial defects such as point defects or columnar tracks, depending on the ion species, energies, and doses. These defects act as additional flux pinning centers, improving in-field J_c without significantly altering the addition.

In MgB_2 bulks, addition (such as with carbon or nano-oxides) is widely

recognized as the most effective method to enhance superconductivity and flux pinning. However, applying this approach directly to materials often induces phase segregation and rapidly reduces T_c. To overcome these limitations, finding suitable additives plays a decisive role in mitigating T_c degradation.

In MgB_2 films, ion irradiation has emerged as a superior method to enhance critical parameters J_c, T_c. Ion irradiation introduces controlled, artificial pinning centers - such as point-like defects and lattice distortions - without altering the crystal structure of the materials. Since excessive irradiation might damage superconductivity, the exact link between irradiation-induced crystal structural alterations and flux pinning improvements is unclear. Investigation of MgB_2 films for functioning superconducting wires requires a careful study of these processes.

To shed light on these issues, the doctoral thesis entitled **"Investigation of the crystal structure and critical parameters of MgB_2 superconductors through addition and ion irradiation"** was initiated.

In the dissertation, both approaches are systematically combined to investigate their influence on the structural and superconducting properties of MgB_2. The addition method will be performed by co-adding Mg and SiC in MgB_2 bulks. Ion irradiation will be performed using Ni and Nb ions at controlled ion parameters, supported by Stopping and Range of Ions in Matter (SRIM) simulations to model defect profiles. The correlation between the crystal structure (lattice parameters, strain, and defect distribution) will be characterized by using the X-ray diffraction (XRD), Raman spectroscopy, and Atomic Force Microscopy (AFM) measurements. The superconducting parameters (T_c, J_c, and B_{c2}) measured by using the Physical Properties Measurement System (PPMS) will be analyzed.

b. The purpose, objectives, and scope of the research

Research purpose: This research aims to enhance the critical parameters of MgB_2 superconductors, thereby improving their superconductivity in high-field for practical applications such as superconducting wires and tapes. To achieve this, the study employs a dual-track approach to comprehensively evaluate and contrast bulk

and thin-film forms, aiming to overcome current material limitations.

Within this approach, bulk MgB_2 with additives is studied to analyze the mechanisms of modification, where adding with SiC and excess Mg serves to reduce grain size, mitigate T_c degradation, and enhance pinning. Concurrently, thin films fabricated via HPCVD are analyzed to explore physical defect-engineering through Nb and Ni ion irradiation. While the former relies on chemical additives, the latter utilizes ion bombardment to introduce precise, nanoscale artificial pinning centers without altering chemical stoichiometry. By evaluating both approaches, this research aims to improve a comprehensive framework for tailoring superconducting properties across different material dimensions

Research objectives: To fulfill the purpose outlined above, the investigation focuses on the following specific objectives:

Sample synthesis and fabrication: To synthesize bulk MgB_2 samples via solid-state reaction with systematically varied SiC and Mg co-dopant concentrations under controlled sintering profiles, and to deposit pristine MgB_2 thin films onto designated substrates using HPCVD for subsequent ion irradiation.

Defect engineering via metallic ion irradiation: To subject the HPCVD-grown thin films to Nb and Ni ion irradiation by systematically varying fluences to generate distinct profiles of point defects, clusters, or columnar tracks.

Material characterization: To evaluate and compare changes in crystal structure, lattice parameters, phase purity, and grain boundaries of both bulk and thin-film forms, while measuring superconducting parameters including J_c, T_c, and B_{c2}

Performance evaluation and mechanism analysis: To analyze the effects of chemical co-adding in bulk samples and physical ion irradiation in thin films, establishing a baseline to correlate crystal lattice variations with macroscopic flux pinning behaviors for enhanced in-field performance.

Research scope: The scope of this scientific research is strictly specified to keep the depth and empirical emphasis within the following bounds:

- *Material choice and processing methods:* The investigation is limited to

MgB_2 as a single superconducting compound and is strictly confined to two branches of processing: chemical co-adding for bulks samples and physical ion irradiation for thin films. Only the HPCVD process is utilized for pristine thin-film fabrication.

- *Chemical and physical modifiers:* The chemical modification of the bulk phase is limited to the binary addition of SiC and Mg powder. The post-treatment of the thin films is strictly confined to irradiation by ions (Nb and Ni) within the safe energy range in an effort to avoid total amorphization of the material.

- *Measurement horizons:* The evaluation is limited to microstructural crystal dynamics, surface morphology (for films), and critical state, in-field superconducting performance.

c. The scientific novelty

The academic and scientific relevance of this study is the enhancement of superconducting characteristics in MgB_2. In particular, the scientific importance includes:

- Understanding bulk modification mechanisms: The work presents the experimental evidence for utilizing co-adding (SiC + Mg) to enhance the superconducting performance and flux pinning in bulk MgB_2.

- Characterization of thin film defect dynamics: The work explores the role of physical defects created by Ni and Nb ion bombardment in enhancing the superconducting characteristics of high purity, HPCVD-grown thin films.

- Understanding vortex pinning mechanism: The work offers a balanced view to understand pinning mechanisms by studying addition in bulk samples and irradiation in thin films. In this sense, it assesses the extent to which these complementary techniques constrain vortex motions in high fields, hence providing valuable insights to solid-state physics and superconducting materials research.

In addition to theoretical understanding, this work provides crucial data to advance the development of MgB_2 superconductors for practical applications and focuses on informing superconducting wire and tape production. Furthermore, it identifies which parameters improve J_c in fields for both configurations, providing a

foundation for the development of high-field superconductors used in MRI systems, and superconducting cables.

d. New findings of the thesis

+ *Impressive maintenance of the T_c after addition or irradiation:* The simultaneous addition of Mg and SiC to bulk MgB_2 samples preserved T_c above 37 K. The T_c of thin-films was maintained above 32 K after irradiation. There were impressive results in maintaining T_c compared with domestic and international studies, overcoming the common disadvantage of the sharp reduction in T_c encountered upon addition or irradiation.

+ *Discovery of a shift in the flux-pinning mechanism through ion irradiation:* It was demonstrated that a partial shift of the pinning mechanism from normal surface pinning to normal point pinning occurs in the high-magnetic-field region in MgB_2 thin films after Nb and Ni ion irradiation.

+ *Discovery of relatively strong pinning induced by Ni ions:* Ni ion irradiation produced a transition from a weak-pinning to a relatively strong-pinning mechanism. At 5 K, the pinning strength in the sample irradiated with a dose of 3×10^{13} ion/cm² yielded $\beta = 0.67$ (approaching the theoretical value of $\beta = 5$ for the strong-pinning).

+ *Elucidation of the stronger J_c enhancement via ion tracks:* It was established that Ni ion irradiation yields a stronger enhancement of the critical current density J_c in high magnetic fields than Nb ion irradiation. The dissertation clarified that the origin of this phenomenon lies in the higher and more uniform density of point defects within the film, in the form of ion tracks and lattice distortion.

+ *Precise determination of the irradiation-dose thresholds yielding the best J_c enhancement:* The dissertation identified the precise quantitative values yielding the optimal J_c enhancement for each ion species in 400-nm-thick MgB_2 thin films (fabricated by HPCVD): for Nb ions (1 MeV), the optimal dose is 7×10^{13} ion/cm²; for Ni ions (1 MeV), the optimal irradiation dose is 3×10^{13} ion/cm². In both cases T_c is maintained above 30 K, entirely suitable for practical applications without the need for liquid-helium cooling.

Chapter 1. LITERATURE OVERVIEW

Scientifically, several physics phenomena are the results of mutual interactions; thus, extreme-condition research frequently discovers unanticipated properties of materials that might be crucial to technological developments. Superconductivity also illustrates this realization. In recent decades, superconductivity has moved from lab curiosity to practical research. In the beginning chapter, the thesis provides an overview of the fascinating world of superconductivity. To keep the dissertation within reasonable limits, it was necessary to briefly summarize some topics.

1.1 Superconductors

1.1.1 Superconductor developments

In 1911, Kamerlingh-Onnes discovered that mercury resistance was very low below 4.2K, making measurement difficult. In further investigations with advanced equipment, he quickly discovered that the observed effect was not the predicted resistance decline. Resistance varied within a few hundredths. Resistance appeared to rise suddenly rather than fall. A word for this unusual phenomenon was found: **superconducting**. The discovery of superconductivity was of great scientific importance, as evidenced by Kamerlingh - Onnes being awarded the Nobel Prize in physics in 1913. [47]

In 1933, the perfect diamagnetism of superconductors was discovered by W. Meissner and R. Ochsenfeld [72]. Superconductors have more than simply electrical resistance dropping below the critical temperature. Except for a narrow exterior layer, superconductors reject magnetic fields. This characteristic is "ideal diamagnetism" or the "Meissner-Ochsenfeld effect."

In 1935**,** Fritz and Heinz London formulated “The London equations” [69]. These are a pair of phenomenological equations that describe the electrodynamics of superconductors. They explain two key properties of superconductors: perfect

conductivity (zero electrical resistance) and the Meissner effect (expulsion of magnetic fields). The key concept “penetration depth” λ_L characterizes the distance a magnetic field penetrates into a superconductor given in the equations.

In 1957, the BCS hypothesis by J. Bardeen, L. N. Cooper, and J. R. Schrieffer revolutionized superconductivity [5]. In 1972, they won the Nobel Prize in Physics for their innovative hypothesis. Electrons form pairs to generate a new state during the superconducting transition. According to quantum physics, they create a unified matter wave with a defined phase in this condition. The quantized vibrations of the crystal lattice, called "phonons," help electrons interact in this environment.

In 1974, D. Dew-Hughes showed “Flux pinning mechanisms in type II - superconductors” [19]. Important parts of this paper are: (1) *Flux Pinning Mechanisms*: This classified the interaction of defects in superconductors with magnetic flux lines, thereby pinning them to inhibit dissipation. (2) *Scaling rules*: The study developed scaling rules for pinning forces that did not need the assumption of flux-lattice elasticity. (3) Dew-Hughes found certain functional forms, which are sometimes called the *Dew-Hughes model*, that show how pinning strength changes with magnetic field.

In 1986, J. G. Bednorz and K. A. Müller discovered copper oxide superconductors, a major advance. Two scientists were honoured with the Nobel Prize in physics in 1987 for their remarkable discovery. The authors found that this material loses resistance at 30 K. In 1987, two scientists discovered “Susceptibility Measurements Support High-T_c Superconductivity in the Ba-La-Cu-O system”. It's surprising the paper got little attention. The superconducting observation was dubious. The samples included non-electrical phases. Thus, their particular electrical resistance was high. A texture phase transition may have caused the resistance decline. Therefore, further data was needed to prove superconductivity in these samples. [26,27]

From 1986 to 1999, there was a surge of excitement when it was discovered that S. Tanaka's group in Japan was able to replicate the groundbreaking findings of

Bednorz and Müller [26]. Since then, labs worldwide have studied these novel oxides. Soon, this exceptional scientific effort yielded outstanding results. La-Sr-Cu-O superconductors with transition temperatures exceeding 40 K have been created. Researchers found Y-Ba-Cu-O transition temperatures exceeding 80 K after a few weeks [36]. From this time, labs worldwide have studied these novel oxides. Soon, these Press conferences were used more than scientific publications to publicize new results. Media eagerly monitored this development. One might envisage several important technological uses of superconductivity above the boiling point of liquid nitrogen (T = 77 K).

In 2001, superconductivity of MgB_2 was found with T_c = 39 K [75]. It's quite remarkable that the discovery of superconductivity in MgB_2, didn't happen until the early 2000s, despite the fact that this material had been commercially available for quite some time. This discovery sparked significant interest within the physics community, leading to important advancements in understanding the properties of this material over the next two years. MgB_2 exhibits behaviour that is reminiscent of the behaviour seen in traditional metallic superconductors.

In 2008, the excitement surrounding the discovery of the iron compounds was also significant. These compounds, such as $LaFeAsO_{0.89}F_{0.11}$ or $Ba_{0.6}KFe_2As_2$, exhibit impressive T_c up to 55 K [39]. These materials have layers of iron-arsenic that serve as the central building block, similar to the copper oxide planes found in cuprates.

YBCO achieved picosecond room-temperature superconductivity in 2014 utilizing brief pulses of infrared laser light to distort its crystal structure [70]. Undiscovered superhard materials like heavily doped beta-titanium Au were suggested as T_c superconductors in 2017. This superconductor would have a temperature that is much higher than that of HgBaCaCuO (135 K, but under a pressure of 30 GPa, it can go as high as T_c = 164K), and it may even reach 233 K, which would be greater than that of hydrogen hydroxide. According to the findings of a significant amount of study, nickel might instead substitute copper in some perovskites, therefore providing an extra path to room temperature.

The breakthrough in high-temperature superconductors has expanded superconductivity beyond organic life-incompatible temperatures. Future discoveries of materials that display superconducting phenomena at or above room temperature are anticipated. Meanwhile, lower temperatures are becoming more realistic for daily use. Refrigerators and cold boxes are popular home equipment. Refrigeration technology has advanced recently. Modern cryo-coolers may reach 30 K or 4.2K. Many industries cool using liquid nitrogen. Thus, superconductivity will become more integrated into our everyday lives, especially in energy technologies and microelectronics.

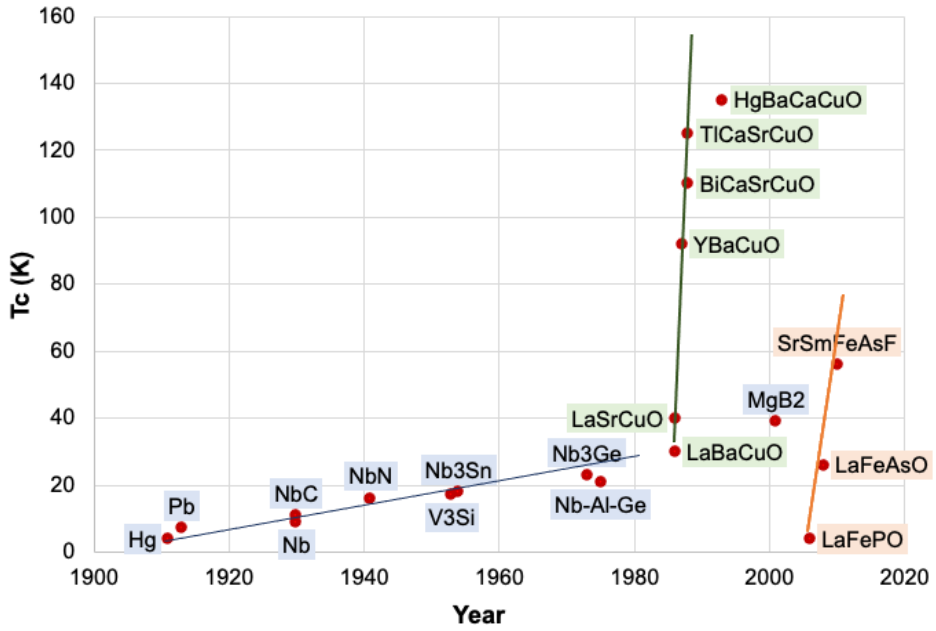


***Figure 1.1**. The critical temperatures of superconductors from 1900 to 2020*

Figure 1.1 illustrates the progression of critical temperatures since their initial discovery by Kamerlingh-Onnes from 1900 to 2020. In this figure, three research directions in superconductivity development have been identified.

1.1.2 Critical parameters of a superconductor

For a superconductor, the superconducting state is established only if the working temperature (T), operation field (B) and the flowing current (I) were all below the so-called critical parameters:

Critical temperature (T_c): temperatures below which superconductors are superconducting with zero magnetic field intensity and electric current.

Critical (magnetic) field strength (B_c): magnetic field strength equivalent to superconducting condensation energy at zero. Note: B_c varies with temperature.

Lower critical (magnetic) field strength (B_{c1}): magnetic field strength which equals superconducting condensation energy at zero. Note: B_{c1} is temperature - dependent.

Upper critical (magnetic) field strength (B_{c2}): Maximum magnetic field strength below which a type II superconductor is mixed. Note: B_{c2} is affected by temperature.

Critical current (I_c): The greatest direct current without resistance. Temperature and magnetic field intensity affect I_c.

Critical current density (J_c): the electric current density at the critical current utilizing the conductor's entire cross-section or the non-stabilizer portion if there is a stabilizer.

1.1.3 Type-I and type-II superconductors

Depending on the magnetic behaviors of the superconductors, two types of superconductors have been classified:

1.1.3.1. Type-I superconductors

Type I superconductors have a critical field, the greatest magnetic field they can withstand before losing superconductivity. Some Type-I superconductors have several hundred Gauss critical fields. These materials may only work under low magnetic fields.[5] [72]. Type-I superconductors have some drawbacks. Low critical field limits its use to circumstances requiring extremely low magnetic fields. Their exceptionally low critical temperature requires cooling to very low temperatures to exhibit superconductivity. Cryogenic cooling systems are complicated and expensive to maintain, therefore this presents technological challenges.

1.1.3.2. Type-II superconductor

Type-II superconductors have numerous critical fields and display a mixed state of superconductivity and normal conductivity when subjected to a magnetic field. Figure 1.2 depicts a schematic representation of the essential surfaces of type I and type II superconductors. A defining feature of type-II superconductors is their many critical fields. These materials display two critical parameters: B_{c1}, B_{c2}. B_{c1} denotes the threshold at which the material shifts from the superconducting state to the mixed state, whereas B_{c2} indicates the maximum magnetic field that the material can endure before completely losing its superconducting properties. [5,19,62]

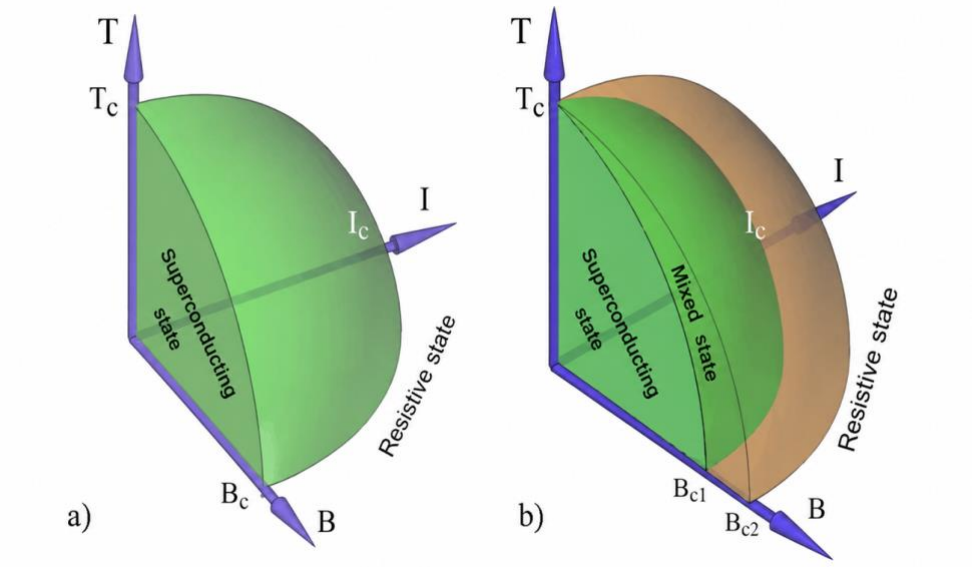


Figure 1.2. *Critical surfaces of (a) type-I, (b) type-II superconductors [18]*

In the mixed state, type-II superconductors show flux pinning. The material's structure traps magnetic flux lines, creating patches of normal conductivity surrounded by superconductivity. Structural faults may immobilize trapped flux lines, making them resistant to magnetic field fluctuations. [5,19,62]. A significant benefit is their elevated critical field, enabling them to withstand much larger magnetic fields

than type-I superconductors. This makes them advantageous for applications like magnetic resonance imaging and high-energy physics investigations.

1.1.4. Vortices in type-II superconductors

1.1.4.1. Typical characteristics of vortices

In type-II superconductors, vortices are indicative of the mixed state, when the material displays both superconducting and normal conducting characteristics. Vortices arise when magnetic field lines penetrate the material and get trapped in limited areas of normal conductivity, leading to a circulating current around the magnetic field lines. Understanding vortex dynamics is essential for the analysis and use of type-II superconductors. Vortices in type-II superconductors are characterized by their size, density, and dynamics. [5,13,19]

The behavior of vortices in type-II superconductors is complex and affected by several factors, including temperature, magnetic field strength, and material properties. A crucial factor affecting vortex dynamics is vortex pinning, which occurs when defects or impurities inside the material immobilize vortices. Pinning is essential since it may restrict vortex movement and energy dissipation, hence improving the superconducting properties of the material [8].

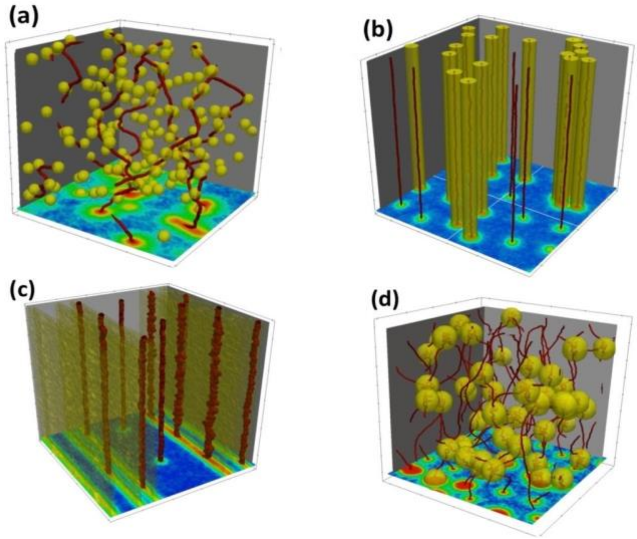


Figure 1.3. *3D picture of vortex matter (red) in defect structures (yellow) with different dimensions [61]*

Figure 1.3: (a) random atomic or point defects (b) linear defects (irradiation-induced tracks, synthesized self-assembled nanorods, dislocations), (c) planar defects (twin boundaries, stacking faults, layered structures), (d) large random defects (rare earth oxide precipitates, irradiation collision cascades, defect clusters, voids). All figures represent solutions of the time dependent Ginzburg-Landau equations. The bottom plane cuts show the amplitude distribution of the superconducting order parameter or condensate density (blue: high, red: low).

The examination of vortices in type-II superconductors has significant ramifications for the advancement of novel superconducting materials and the engineering of superconducting devices. Researchers are developing novel materials with enhanced vortex pinning capabilities, resulting in more efficient and dependable materials for energy storage and transmission applications. Comprehending vortex dynamics may assist researchers in developing superconducting devices that exhibit greater resistance to magnetic field variations and other noise sources.

1.1.4.2. Issue of vortex motion in type-II superconductors

High-power uses of superconductors emphasize their ability to transmit substantial lossless currents. The behavior of the superconductor is essentially governed by the interplay between internal currents and the various vortex states that arise in response to an external magnetic field or are generated by the currents themselves. An external electric current density **J** generates a Lorentz force on the vortex line, aligned perpendicular to both the current direction and the unit vector n along the line, represented as $\boldsymbol{F_L} = (\Phi_0/c)\boldsymbol{J} \times \boldsymbol{n}$, as seen in Figure 1.4.

An applied electric current (**J**) generates a Lorentz force $\boldsymbol{F_L}$ on vortices, acting perpendicular to the current direction, therefore pushing them with velocity *v*. The vortex motion generates a constrained electric field (**E**) that is proportional to *v* and perpendicular to its direction. This signifies that (**E**) is parallel to (**J**), correlating with a restricted flux-flow resistance.

In a homogeneous superconductor, this force propels the vortex at velocity *v*, constrained by the Bardeen-Stephen friction viscosity η, which arises from the normal

quasiparticles inside the vortex core, expressed as $\boldsymbol{v} = \boldsymbol{F_L/\eta}$. The motion of vortices induced by the Lorenz force produces a limited electric field proportional to velocity, expressed as $\boldsymbol{E} = \boldsymbol{B} \times \boldsymbol{v}/c$, which is orthogonal to the velocity and aligned with the electric current, resulting in energy dissipation and a finite flux-flow resistivity.

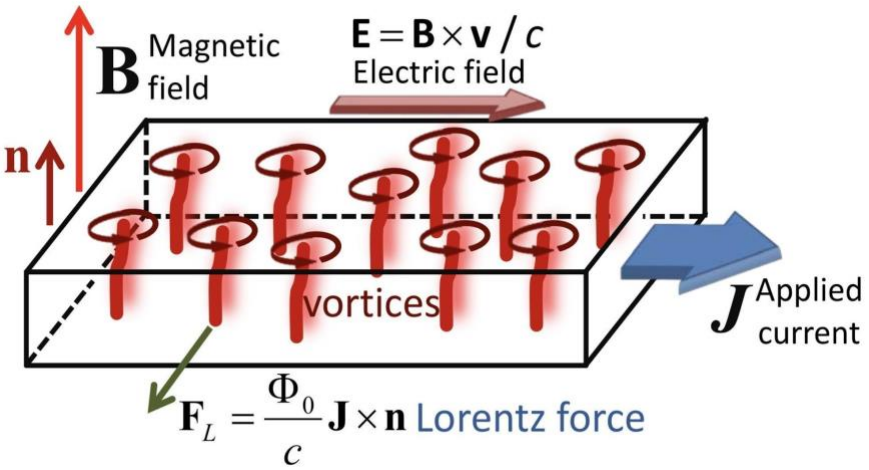


Figure 1.4. *Illustration of dissipation caused by migrating vortices in homogeneous superconductors [61]*

In summary, vortices in type-II superconductors represent a complicated and significant characteristic of these materials. Vortices form when magnetic field lines infiltrate the material and get ensnared in regions of standard conductivity, resulting in a circulating current. Comprehending vortex behavior is crucial for the advancement of novel superconducting materials and the engineering of superconducting gadgets. The investigation of vortices in type-II superconductors is a dynamic field of research, with scientists striving to discover novel materials and processes that might enhance the superconducting characteristics of these materials.

1.2 Several important theoretical models applied for superconductors

1.2.1 Bean's model

Bean's critical state model can be used to compute the J_c of superconductors from magnetization hysteresis (M-H) loops [7,6].

To generate the curve $\boldsymbol{H} = \mu_0 \times \boldsymbol{J_c}$ Ampere's law was used, and the

computation of magnetization was performed using the formula $M = B/\mu_0 - H$. The magnetic flux density was determined using the equation:

$$B = \frac{1}{v} \int H dv \tag{1.1}$$

which followed the definition. In the end, the link between magnetization and J_c is represented by the equation $J_c = a \times d$, where d is the characteristic length, and is a numerical component that is dependent on the shape of the sample, and $\Delta M = M^+ - M^-$ is the height of the hysteresis loop (For a thin film, $a = 30$).

1.2.2 Collective pinning theory in type-II superconductors

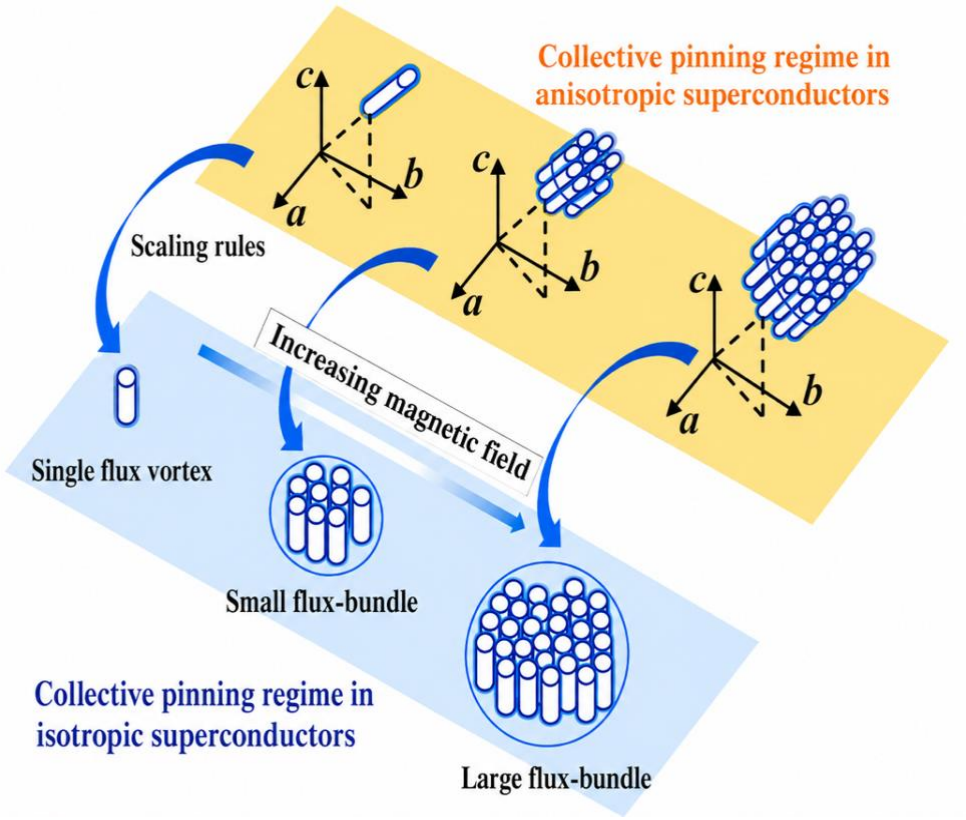


Figure 1.5. *Schematic of field dependence of collective pinning regimes in type-II superconductors. [8]*

One of the most effective frameworks for studying interactions among vortices in type-II superconductors is collective pinning theory. Within this approach, vortices are treated as interacting entities whose behavior is governed not only by their mutual interactions but also by their coupling to the surrounding material. Consequently, the

field dependence of the J_c and the mechanisms of flux pinning in HTS can be systematically analyzed using this theory. Building on this understanding, collective pinning theory describes vortex behavior as arising from multiple interacting factors, including thermal fluctuations and elastic or plastic deformations of the vortex lattice.

The theory assumes that vortices do not act independently but instead form correlated systems whose dynamics are governed by the intrinsic properties of the superconducting material. Another key parameter is the J_c, defined as the maximum current the superconductor can carry without losing its superconducting state. In type-II superconductors, J_c is strongly influenced by both vortex density and their interaction with the pinning landscape. By understanding and optimizing these collective effects, it is possible to enhance the performance of superconducting materials. Figure 1.5 illustrates the evolution of collective pinning regimes with increasing magnetic field.

1.2.2.1. Collective pinning theory for bulk superconductors

As presented in Figure 1.5, the collective pinning regimes were separated basing on the vortex interaction. When the applied field (B) was lower than the value called as a small bundle (B_{sb}), the vortex system is in the single-vortex pinning regime, and the value of J_c remains essentially independent of the applied field [8]

$$B_{sb} = \beta_{sb} \frac{J_{sv}}{J_0} B_{c2}, \quad (1.2)$$

In this expression, $\beta_{sb} \approx 5$ was the dimensionless coefficient, $J_0 = 4B_c/3\sqrt{6}\mu_0\lambda$ is depairing current density. The thermodynamic critical field was given by $B_c = \Phi_0/2\sqrt{2}\pi\lambda\xi$, while $B_{c2} = \mu_0\Phi_0/2\pi\xi^2$. Here J_{sv} denoted J_c in the single vortex regime, λ was the penetration depth and ξ was the coherence length of a type-II superconductor. The constant $\mu_0 = 4\pi \times 10^{-7}$ H/m was permeability of vacuum, and $\Phi_0 \sim 2.067 \times 10^{-15}$ Wb was the flux quantum. When an individual vortex is pinned at a single defect site, the vortex system is said to be in the single-vortex pinning regime. In this regime, the pinning force is determined by the displacement of the vortex from the pinning center. As the applied magnetic field increases beyond B_{sb}, the system

transitions into the small-bundle pinning regime. In this case, a limited number of vortices are collectively pinned within localized regions, forming vortex bundles. The pinning force is then governed by the displacement of these bundles relative to the pinning centers. Accordingly, the field dependence of the J_c in this regime follows an exponential behavior:

$$J_c = J_c(0).\exp\left[-\left(\frac{B}{B_0}\right)^{\frac{3}{2}}\right], \tag{1.3}$$

In this expression, $J_c(0)$ and B_0 are fitting parameters. Collective pinning theory has been widely employed to investigate a range of phenomena in type-II superconductors, including vortex behavior in materials with complex pinning landscapes, vortex dynamics under applied magnetic fields, and the influence of thermal fluctuations on vortex motion.

1.2.2.2 Collective pinning theory for thin film superconductors

The concept of collective pinning was first introduced by A. Larkin and Y. Ovchinnikov in 1979 [62]. The single-vortex pinning regime corresponds to low magnetic fields (B_{c1}), where an individual defect can effectively pin a single vortex. In this regime, energy dissipation is negligible because the Lorentz force is weak, and the intervortex spacing, $a_0 \approx 1.07(\phi_0/B)^{0.5}$, is sufficiently large that vortex–vortex interactions can be ignored. As a result, the J_c remains nearly independent of the magnetic field, leading to a plateau in the $J_c(B)$ curve. However, a single defect is generally insufficient to pin an entire vortex line. Instead, the combined effect of many defects plays a crucial role in determining vortex behavior. As the magnetic field increases, vortex–vortex interactions and Lorentz forces become comparable to or exceed individual pinning forces, leading to a transition into the collective pinning regime. In this framework, pinning arises from statistical fluctuations in the spatial distribution and strength of defects, rather than from individual pinning centers acting independently. When a density n_i of defects exerts an elementary pinning force F_{pin}, the total pinning force acting on a vortex segment of length L can be approximated

as to $F_{pin} \approx f_{pin}\sqrt{n_i \xi L}$. Collective pinning typically occurs in materials with a high density of weak pinning centers. In this regime, the critical current density becomes field-dependent and follows a power-law behavior:

$$J_c(H) \propto B^{-\beta}, \tag{1.4}$$

where $\beta < 1$. The exponent β provides a useful measure of the pinning strength and can be used to evaluate the effectiveness of flux pinning in superconducting samples.

1.2.3 Flux pinning mechanisms in type-II superconductor

Magnetic flux pin performance in type II superconductors was examined in connection to vortices-pin center interactions and magnetic pin center geometry. Without considering the magnetic vortex network's elasticity model, experimental results confirm the hypothesis. Magnetic pinning functions well explain experimental force density curves in large κ and strong magnetic pinning systems.

Four parameters determine flux pinning force density:

(i) The local interaction strength depends on the magnetic pin centers' superconducting properties relative to the lattice.

(ii) To calculate the local equilibrium value of B, the micro-pin structure must be larger and further than the penetration depth λ of each superconductor. Size of magnetic pin centers compared to magnetic inter-vortex distance affects interaction length and shape.

(iv) The magnetic vortex network's stiffness, which influences its displacement under a local magnetic pin force, is entirely elastic, restricted by surrounding magnetic vortices, or powerful enough to break the network and enable the vortex to act independently. [8,62]

1.2.3.1 Interaction types

Magnetic vortices may approach equilibrium if the size (a) and distance (l) of the magnetic pin centers exceed λ. This modification causes magnetic pinning by creating a Bean-Livington potential barrier to magnetic vortices at the pin center and superconducting matrix. This is magnetic interaction. If a or l is smaller than λ,

magnetic equilibrium cannot be achieved. The superconducting parameters deviate from the superconducting matrix; therefore, the magnetic vortices' free energy is in the magnetic pin centers' range. [6,19]

1.2.3.2 Pinning center types

Magnetic vortices interact with pinning centers due to their superconducting properties differing from those of the matrix. The disparity in size dictates the intensity of engagement. Alterations in critical temperature, magnetic field, or Ginzburg-Landau parameter κ may signify minor fluctuations. The characteristics of non-superconducting magnetic pin cores exhibit significant variability. The optimal pinning capacity occurs when the pin centers exhibit ferromagnetism. Common metals, insulators, and holes are non-superconducting particles. The nature of non-superconducting particles does not affect their magnetic pinning strength. If the binding effect turns non-superconducting metal particles into superconductors with a route smaller than the superconducting material's coherence length, the superconductivity may alter κ. Two kinds of magnetic pin centers exist: conventional and $\Delta\kappa$-type pins. [19]

1.2.3.3 Geometry of the pinning centers

Dew-Hughes has developed a model to describe flux-pinning in type-II superconductors, informed by the geometry of the pinning centers and the interactions between individual flux lines and these centers. The normalized flux pinning force density in relation to the normalized field modified function is often utilized: $f_p \sim b^p(1\text{-}b)^q$, where, $f_p = F_p/F_{p,max}$ is the normalized pinning force density, $b = B/B_{irr}$ is the normalized field, p and q are fitting parameters used to determine the pinning center properties. The position of maximum F_p, named as b_{peak}, is estimated by $b_{peak} = p/(p + q)$. All sorts of pinning centers are listed in Table 1.1.

Table 1.1. *Details of pinning mechanism in type II superconductors. [19]*

Type of Interaction	Type of center	Geometry of pin	Pinning function	Pinning parameters	Position of maximum	Max. Const.
Magnetic	Volume	Normal	$Ab^{1/2}(1-b)$	$p = 1/2$ $q = 1$	$b_{peak} = 0.33$	A = 2.56
		$\Delta\kappa$	$Bb^{1/2}(1-2b)$	$p = 1/2$ $q = 2$	$b_{peak} = 0.16$	B = 0.27
Core	Volume	Normal	$C(1-b)^2$	$p = 0$ $q = 2$	-	C = 1.00
		$\Delta\kappa$	$Db(1-b)$	$p = 1$ $q = 1$	$b_{peak} = 0.5$	D = 4.00
	Surface	Normal	$Eb^{1/2}(1-b)^2$	$p = 1/2$ $q = 2$	$b_{peak} = 0.2$	E = 3.50
		$\Delta\kappa$	$Fb^{3/2}(1-b)$	$p = 3/2$ $q = 1$	$b_{peak} = 0.6$	F = 5.37
	Point	Normal	$Gb(1-b)^2$	$p = 1$ $q = 2$	$b_{peak} = 0.33$	G = 6.76
		$\Delta\kappa$	$Hb^2(1-b)$	$p = 2$ $q = 1$	$b_{peak} = 0.67$	H = 6.76

1.3 Overview on MgB_2 superconductor

In this section, MgB_2 superconductors and the history of the scientific studies of superconducting involving will be introduced. The information focuses on the recent publication about MgB_2 materials in order to summarize some advantages and disadvantages of previous research and determine the objectives, content and research methods of the dissertation.

1.3.1 Crystal structure of MgB_2

MgB_2 has a straightforward crystal structure known as AlB_2 -type. The lattice parameters for this compound are a = 3.086 Å and c = 3.524 Å, and it belongs to the space group P6/mmm. In this structure, depicted in Figure 1.6, the (B) layers are stacked in an alternating pattern with (Mg) layers.

The (B) layers create a honeycomb lattice in 2 dimensions, with each B atom

being surrounded by 3 other B atoms. This arrangement forms an equilateral triangle with a B-B. The layers of Mg are arranged in a triangular lattice, where the distance between Mg atoms is exactly equal to the lattice parameter a. Every Mg atom is located at the center of a hexagonal prism made up of B atoms, with a distance of 2.5 Å between the B and Mg atoms. This AlB_2-type structure remains unchanged regardless of temperature fluctuations or external pressure.

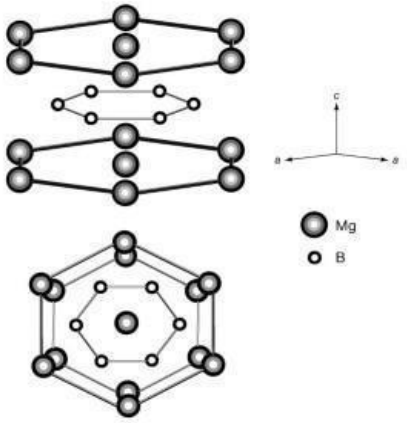


Figure 1.6. *The hexagonal structure pure MgB_2 [75]*

Figure 1.7 illustrates the Fermi surface of MgB_2. It is composed of two cylindrical sheets surrounding line A, originating from the bands with minimal k_z dispersion. In addition, there are 2 tubular networks that arise from the bands: one for antibonding electron-type sheets and another for bonding hole-type sheets. Experimental studies have been carried out to examine the Fermi surface by utilizing the de Haas van Alphen effect.

The band structure of MgB_2consists of two σ bands that are formed through the bonding of $P_{x,y}$ orbitals, along with two π bands that arise from the bonding and antibonding hybridization of P_z orbitals. The two σ bands, which correspond to the bonding orbitals of the *B* sublattice, display a behavior characteristic of holes. The σ holes are concentrated along the ΓA direction of the Brillouin zone, particularly within the B planes, and exhibit a clear two-dimensional characteristic. Contrastingly, the two π bands display a three-dimensional characteristic, with one being hole-type and the other being electron-type. Chemical substitutions can be used to selectively

dope the σ and π bands by replacing the B and Mg sites in this band structure. The σ and π bands at the Fermi level contribute almost equally to the overall density of states. The charge density distribution reveals the significant covalent character of the B-B bond, whereas the Mg atoms are fully ionized and in a divalent state. [74,75]

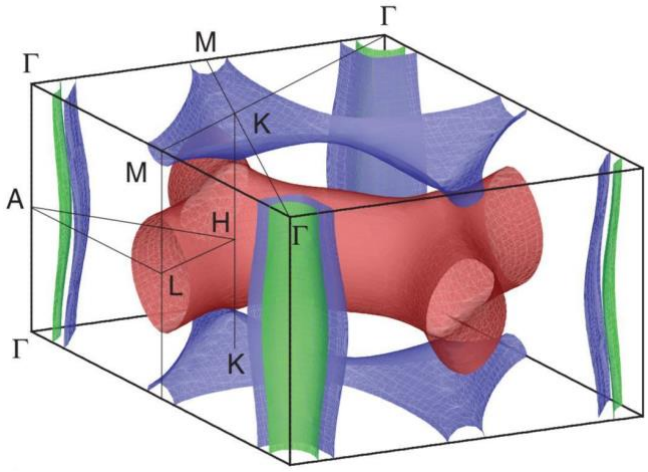


Figure 1.7*. The Fermi surface of MgB_2 [74]*

Currently, extensive study has elucidated all the essential physical mechanisms that determine the superconducting and normal state behavior of MgB_2. The main characteristic of this material is primarily attributed to the existence of two bands and two energy gaps, which have a significant impact on its properties. Furthermore, the majority of MgB_2's characteristics are highly influenced by the rates of intraband and interband scattering. This means that, in theory, these features can be intentionally modified through appropriate chemical substitutions and irradiation.

MgB_2 - a "medium temperature" superconductor - was identified as a BCS-type superconductor that relies on electron-phonon interaction for pairing. Its T_c of 39K was found to be 70% greater than that of Nb_3Ge, which was previously the highest value of T_c for this pairing, see Figure 1.8. The high value T_c piqued interest right away, especially for applications that need cryocoolers, which are smaller and far more effective at greater load temperatures. When theoretical calculations revealed that superconductivity occurred in two different bands of carriers, the σ and

π bands, each with its own energy gap, $\sigma \sim 7.5$ and $\pi \sim 2.3$ meV, which open at the Fermi level, MgB_2 became of special interest in science.

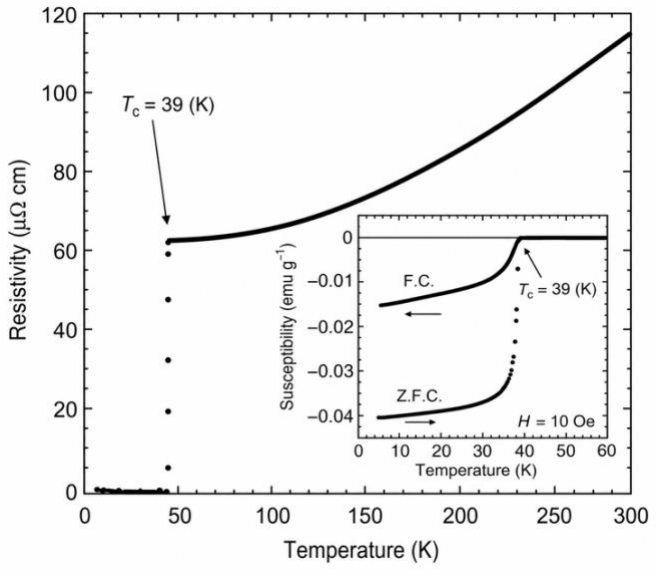


Figure 1.8. *The temperature dependence of resistivity and magnetic susceptibility (inset). [74]*

Measurements like specific heat [10,108], tunneling [11,49], and point contact [97] quickly revealed the two energy disparities. Since the 1950s, multiple-gap superconductivity has been studied theoretically. However, the absence of definite evidence for the predicted behavior in the compounds that are currently on the market seemed to suggest that this process had little practical significance. It is now evident that to witness multi-gap superconductivity, inter-band impurity scattering must be negligible in order to prevent the weakly and strongly coupled Cooper pairs from being mixed. This pair-breaking mechanism reduces T_c in MgB_2 to an isotropic value, estimated to be approximately 20 K, by mediating the order parameters, resulting in the merging of the two gaps into one.

1.3.2 Some power applications of the MgB_2 superconductor

Because of its relatively high $T_c \sim 39$ K and exceptionally large value self-field $J_c > 1$ MA/cm² at temperatures below 20 K, MgB_2 is widely regarded as a highly

practical superconductor for operation in liquid hydrogen environments (around 20 K) and under low magnetic fields. In addition, its low cost and light weight further enhance its potential for both civilian and aerospace applications. At present, companies such as Italy's ASG-Columbus Superconductors, the United States' Hyper Tech, and China's Western Superconducting Technologies (WST) have made significant contributions to the commercialization of MgB_2. Utilizing commercially available MgB_2 wires and tapes, a range of applications has been realized, including superconducting cables, magnets, and wind turbine generators. The following section outlines the progress made by several representative companies in advancing MgB_2 -based technologies.

1.3.3. Studies on improvements of the flux-pinning properties in MgB_2 bulks

1.3.3.1. Substitution/additions into MgB_2 bulks

Chemical substitutions using non-magnetic elements seem to be the most effective approach for enhancing the superconducting characteristics of MgB_2 in high-field applications. Carbon doping in MgB_2 using pure carbon and other carbon-containing compounds, including carbohydrates [60,65,87,98] carbon nanotubes [51,91], B_4C[80,112], and SiC[21,30,32,103], has shown enhancement of superconducting characteristics, particularly B_{irr}, B_{c2}, and J_c under high magnetic fields. Doping rare earth oxides [31] alongside carbon, magnetic nanoparticles, and co-doping rare earth elements with carbon [77], has been shown to enhance the superconducting properties of MgB_2. The influence of graphene doping on the superconducting properties of MgB_2 has been recently investigated.

In contrast to conventional carbon sources, where J_c is lowered, graphene-doped MgB_2 shows a significant increase in $J_c$with little drop in T_c. Kumar *et al.* investigated the structural and superconducting characteristics of graphene (GO) doped MgB_2 [95]. Sintering at 850 ˚C in a reduced *Ar/H₂* (9:1) environment yielded bulk polycrystalline samples with $MgB_2 + x$ structures, where *x* represents the weight percentage of GO (*x* = 0, 1, 2, 3, 5, 7, and 10). In the whole magnetic field range (0 -

8 T), samples x = 1, 2, and 3 showed a considerable increase in J_c when compared to the undoped sample. Aside from J_c, the doped samples with x = 1, 2, and 3 exhibited moderate increases B_{irr} and B_{c2}. Furthermore, up to a doping level of 10%, T_c remained unchanged.

Figure 1.9. revealed the J_c enhancements for in-situ MgB_2 samples with the co-additions of Si nanoparticles and LaB_6. With increasing Si nanoparticles addition from 0 to 5 wt.%, the J_c at 3T and 20 K increased from 1.1 kA/cm² to 2.8 kA/cm², indicating enhanced flux pinning under high magnetic fields. However, the simultaneous addition of LaB_6 and Si nanoparticles resulted in a reduction of both self-field and in-field J_c.

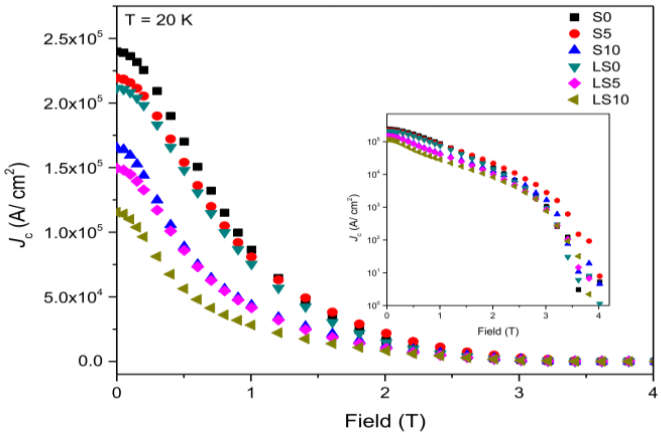


***Figure 1.9**. The magnetic field dependence of J_c for in-situ MgB_2*

Samples is shown for specimens containing x wt.% Si nano (denoted as S0, S5, and S10) and those co-doped with 0.03 mol LaB_6 alongside x wt.% nano-Si (denoted as LS0, LS5, and LS10), measured at 20 K. [35]

This decrease is likely attributed to the excessive formation of impurity phases such as Mg_2Si and LaB_6, which disrupt superconducting pathways and limit effective current flow within the samples. The onset T_c of the undoped sample was 37.5 K and showed a slight decline with increasing levels of co-doping. Flux pinning analysis further revealed that samples with Si nanoparticles addition exhibited higher pinning

forces compared to the pristine sample, confirming the beneficial role of Si nanoparticles in improving vortex pinning. [35]

Kim *et al.* studied the influence of charcoal doping on the superconducting characteristics of *in-situ* processed MgB_2 bulk samples [55]. The charcoal powder was attrition milled for 1 hour, 3 hours, and 6 hours using ZrO_2 balls. The milled charcoal powders were combined with magnesium and boron powders to yield $Mg(B_{0.975}C_{0.025})_2$. $Mg(B_{0.975}C_{0.025})_2$ stoichiometric compact mixes were heat-treated for 0.5 h at 900°C in Ar gas. The samples' T_c fell when the size of the charcoal powder was lowered. $Mg(B_{0.975}C_{0.025})_2$ generated with large-sized charcoal powder showed a lower J_c than pure MgB_2. However, in $Mg(B_{0.975}C_{0.025})_2$ generated with small-size charcoal powder, a crossover of J_c value was seen at high magnetic fields of around 4T. When tiny-size charcoal was used as a dopant, carbon diffusion into the boron site was facilitated, resulting in a rise in J_c.

1.3.3.2. Irradiation on MgB_2 bulks

Superconducting properties are very vulnerable to structural defects. Irradiation has been found to be a viable strategy for raising the critical currents of high-T_c superconductors by introducing defects that may act as pinning centers, preventing vortices from migrating around T_c. The effects of defect scattering (due to various irradiations) on T_c multiband superconductors have been investigated. MgB_2, a two-band superconductor, may have defects that obscure variations on the Fermi surface. Unfortunately, no significant changes in T_c or increases in critical current have been recorded in MgB_2. Several studies are critical for understanding how irradiation and defects influence superconducting properties. Eventually, γ-rays are an important source of irradiation since they may penetrate superconductors and induce defects throughout the sample. Several studies have been published on how γ irradiation influences the properties of high - T_c superconductors. However, all the studies seem to reveal that irradiation with ions on bulk materials of MgB_2 had no significant effect on T_c or other superconducting characteristics. [52,90]

1.3.4. Studies on improvements of the flux-pinning properties in MgB_2 films

1.3.4.1. Introductions of buffered layers

One of the most popular buffered layers to help to enhance J_c in MgB_2 films was ZnO as presented in Figure 1.10. Overall, increasing the thickness of the ZnO buffer layer can enhance the J_c of MgB_2 films due to the introduction of additional flux pinning centers, such as point defects and grain boundaries. However, excessive impurity incorporation at higher ZnO thickness leads to the formation of voids and secondary phases, resulting in significant structural inhomogeneity. These imperfections reduce the effective cross-sectional area available for current transport, thereby degrading the field-dependent J_c, as observed in the MB40 film.

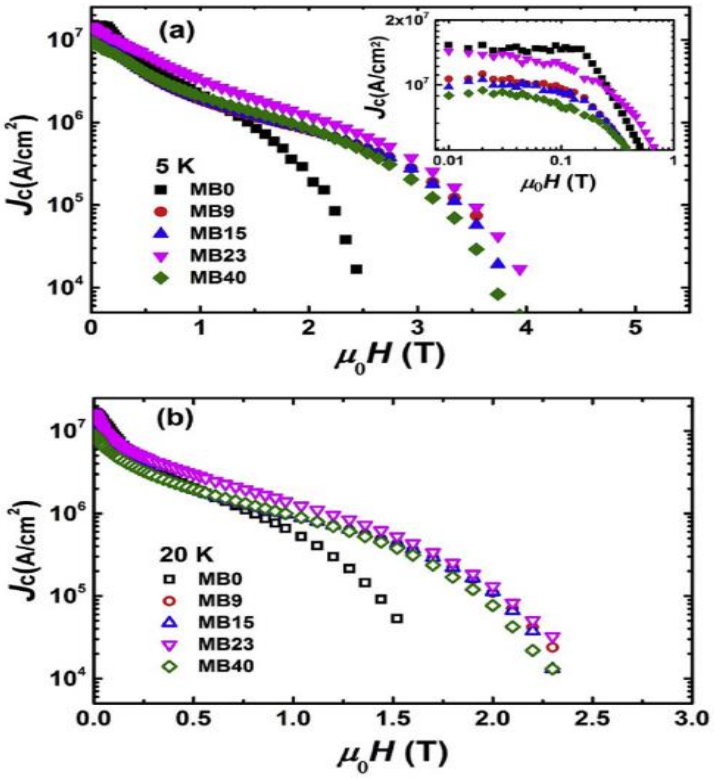


Figure 1.10. *Field dependence of J_c for pure and ZnO-buffered MgB_2 films at (a) 5 K and (b) 20 K*

(shows that all samples incorporating ZnO buffer layers exhibit higher values of J_c at $\mu_0 H > 1.5$ T (at 5 K) compared to the unbuffered film.[83])

Compared with MgB_2 films fabricated using other techniques, the values J_c in this work exhibit a more rapid decline with increasing magnetic field. Nevertheless, films produced by alternative methods often suffer from lower and less reproducible T_c. Although such films may contain a high density of defects and disorder that can enhance flux pinning, the overall impact of these structural irregularities remains complex and not yet fully understood.

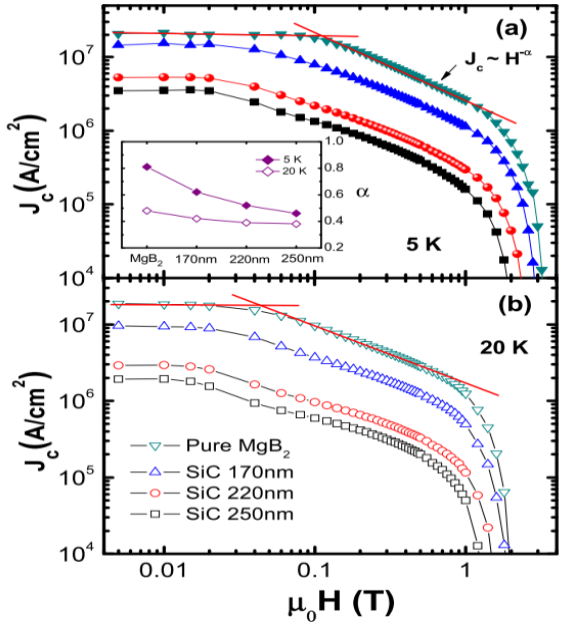


***Figure 1.11**. Magnetic field dependence of J_c for pure and SiC-buffered MgB_2 films. (Double-logarithmic plots for films deposited on Hastelloy substrates with varying buffer layer thicknesses, measured at (a) 5 K and (b) 20 K)* [48]

Among various dopants, silicon carbide (SiC) has been shown to be highly effective in enhancing the superconducting properties of MgB_2. In literatures [48], it has been demonstrated that the J_c of MgB_2 films can be significantly improved by incorporating SiC in the form of crystalline buffer layers deposited on Al_2O_3 substrates. Building on these results, they have investigated the effectiveness of applying the SiC buffer layer to MgB_2 films grown on a metallic substrate, specifically Hastelloy. Hastelloy is widely used in coated conductor applications and is therefore a promising candidate for MgB_2 superconducting wires and tapes. The

SiC buffer layer serves multiple purposes: it suppresses metal diffusion into the MgB_2 films, reduces interfacial delamination between the Hastelloy substrate and the MgB_2 layer, and may also enable carbon diffusion into the MgB_2 structure. This carbon incorporation, analogous to C doping, is expected to enhance both the J_c and flux pinning properties as presented in Figure 1.11.

1.3.4.2. Ion irradiations

The ion irradiations have been shown to be relatively effective in creating (i) columnar defects when the high energies of ~ GeV or TeV were employed, or (ii) ion-tracks/dislocations/lattice distortions when the energies of ≤ MeV were performed. Most of the recent studies have focused on the case (ii) since the energies of ≤ MeV could help to investigate the more details in the formation of ion-tracks, effect of projected range on the improvements of flux pinning properties in superconducting films.

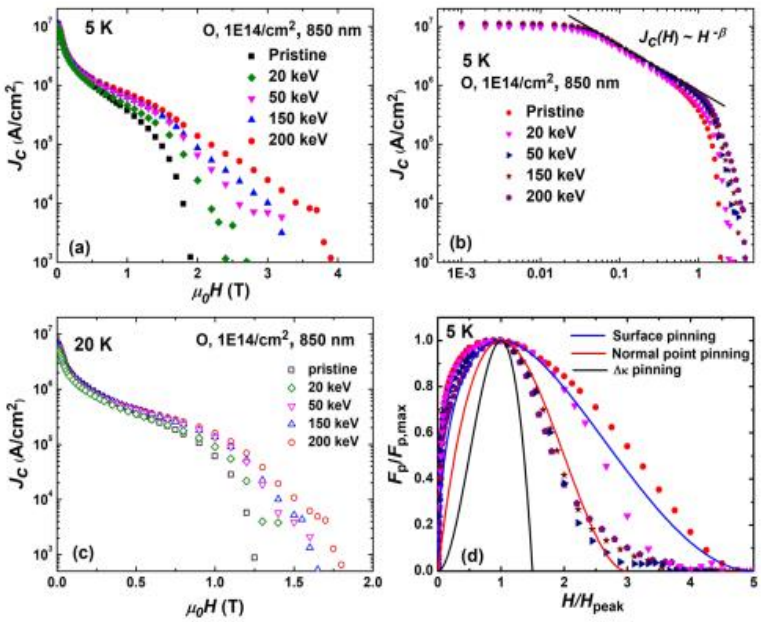


Figure 1.12. *Enhancements of J_c in MgB_2 films using the O-ion irradiation. [82]*

Initially, the irradiation of non-magnetic oxygen ions was conducted [82]. The superconducting properties of MgB_2 films with varying thicknesses were investigated before and after implantation with 50 keV O-ions.

To examine the energy dependence, an 850 nm-thick film was additionally implanted at energies of 20, 50, 150, and 200 keV. Results in Figure 1.12 showed that at 2T and 5 K, the J_c of the film implanted at 200 keV reached approximately 10^5 Acm^{-2}, which is two orders of magnitude higher than that of the pristine film. This enhancement is comparable to improvements achieved using other impurity-based methods in MgB_2 films. In contrast, the self-field J_c remained unchanged when the ion penetration depth was up to 320 nm (corresponding to 200 keV). These results suggest that implantation energies exceeding 200 keV may further enhance the high-field J_c.

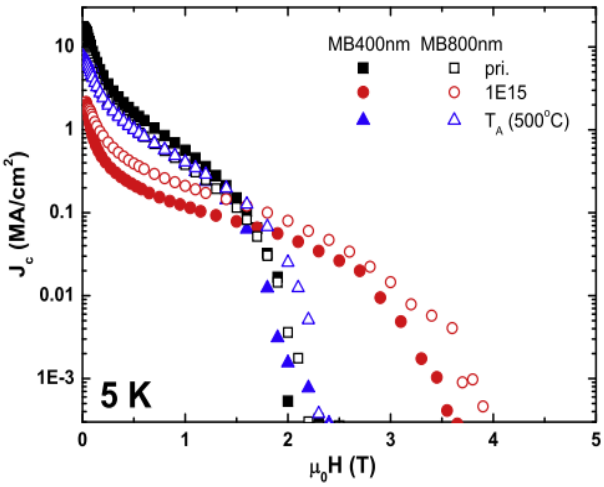


Figure 1.13. *Enhanced field performance of J_c in irradiated MB400nm and MB800nm films.*

(Magnetic field dependence of J_c measured at 5 K for films in pristine, irradiated 1×10^{15} C ions/cm² (1E15) and annealed 500 °C states [45].)

To study the effect of ion irradiation on the flux pinning properties, the influence of carbon-ion irradiation using the relatively higher ion energies of ~ 350 keV on the superconducting critical properties of MgB_2 thin films was studied. Films

with two different thicknesses, 400 nm (MB400nm) and 800 nm (MB800nm), were irradiated with 350 keV carbon ions over a wide dose range of 1×10^{13} to 1×10^{15} ions/cm^2. The mean projected range (R_p) of 350 keV carbon ions in MgB_2 is approximately 560 nm; therefore, the ions fully traverse the MB400nm films, while they are largely retained within the MB800nm films. T_c, B_{c2}, c-axis lattice parameter, and corrected residual resistivity (ρ_{corr}) exhibit similar trends as a function of fluence for both film thicknesses. However, distinct behavior in the superconducting phase transition is observed in the MB800nm films at doses exceeding 1×10^{14} ions/cm^2. This difference arises from the coexistence of irradiated and non-irradiated regions within the thicker films, which possess different values of T_c.

As presented in Figure 1.13, a large self-field J_c in the pristine films, along with its rapid decrease under applied magnetic fields, indicates the high quality of the MB400nm and MB800nm samples. The field dependence of J_c in both irradiated films is significantly improved compared to the pristine state, due to additional flux pinning centers introduced by carbon-ion irradiation. However, a noticeable reduction in J_c at zero magnetic field is observed, which can be attributed to the suppression of superconducting regions and a decrease in the T_c. Furthermore, the value of J_c of the irradiated MB800nm film is slightly higher than that of the irradiated MB400nm film, likely due to the presence of a non-irradiated layer in the MB800nm structure. [45]

If the initial investigations mainly focused on the usage of non-magnetic ions. The recent studies on magnetic ions have been conducted [44, 45, 43, 107] as revealed in Figure 1.14. However, the results on enhancements of J_c were not widely reported.

Field dependence of J_c for the pristine and Co-ion irradiated MgB_2 films measured at T = 5 K and T = 20 K were given in Figure 1.14. Value of J_c was found to be relatively large at zero field, and obviously decreased as increasing the applied field. By using the Co-ion irradiation, the clear in-field enhancements of J_c were obtained.

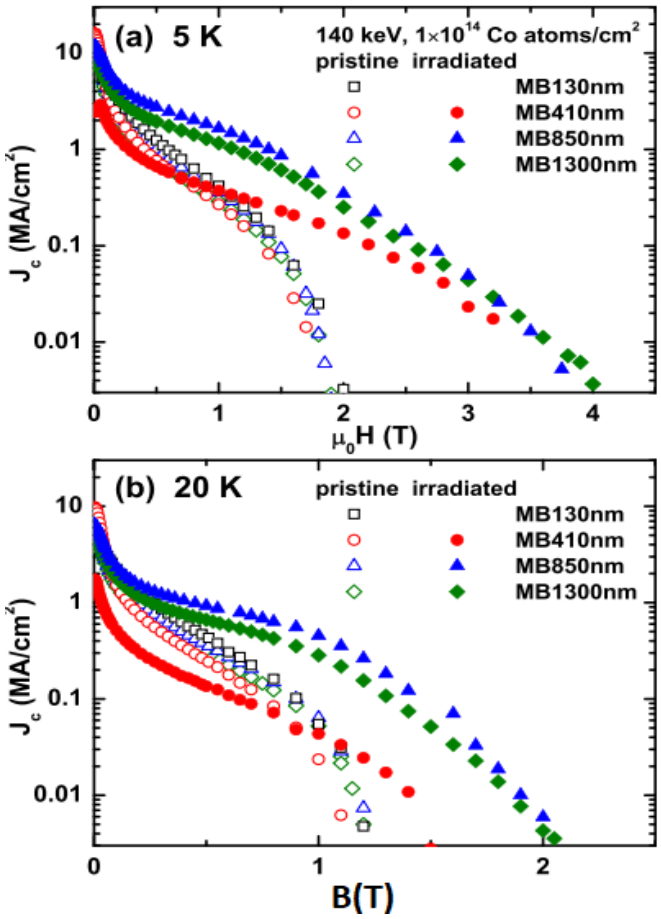


***Figure 1.14**. Enhancements of J_c in MgB_2 films by using the Co-ion irradiation. [43]*

1.4 Motivation

In comparison to other superconductors, the MgB_2 superconductor possesses a number of benefits, such as a low cost, two energy gaps, a simple crystal structure, and a high value of self-field J_c. Nevertheless, its practical applications remain limited due to rapid decline of J_c under magnetic fields. After reviewing the recent studies on the improvements of critical parameters of B_{c2} and J_c in MgB_2 materials, it is evident that the irradiation technique offers distinct advantages over alternative methods. Motivated by these established findings, this dissertation will focus on the improvements of critical parameters of MgB_2 bulk samples and thin films by utilizing both addition and ion irradiation methods. By altering the types of ions, varying the projected ranges as well as ion doses, different interaction dynamics between ions and the crystal structure are induced, which directly generate controlled point-like

defects in MgB_2 superconductors. As a result, enhanced superconducting properties of the MgB_2 superconductors are achieved. To achieve these objectives, the dissertation is structured as follows:

- Fabrication and evaluation of enhancements in the critical parameters of bulk MgB_2 superconductors: By systematically varying the percentage of SiC within co-added (Mg+SiC) from 0% to 20%, the superconducting in bulk samples before and after addition are investigated to identify the correlation between dopant concentrations and performance enhancements of superconductivity

- Fabrication and evaluation of enhancements in the critical parameters of the MgB_2 thin film superconductors: pristine MgB_2 superconducting films are fabricated via the HPCVD method. While irradiated films are processed using Ni and Nb ion bombardment. By adjusting the irradiation doses, the superconducting properties are investigated before and after irradiation to achieve the highest performance enhancement in thin films.

- Analysis of crystal structure variations in MgB_2 films: Variations in the crystal structure of MgB_2 before and after ion irradiation are evaluated using the X-ray diffraction (XRD), Raman spectroscopy, and atomic force microscopy (AFM) measurements. The effects of ion irradiations are characterized by critical structural responses: (i) the expansion of the *c*-axis lattice parameter in the irradiated films, consistent with the irradiation trajectory, (ii) the developments of the phonon density of states (PDOS) in the ion irradiated MgB_2 films with increasing ion dose, and (iii) the changes in the surface morphology of the ion irradiated MgB_2 films. Through investigating the variations in crystal structure, these sections explain why these variations influence on the superconductivity of the materials.

Chapter 2. EXPERIMENTS

2.1 Sample fabrications

2.1.1 Fabrication of pure bulks from ex situ powder MgB_2

To synthesize pure bulk MgB_2, commercially sourced MgB_2 powder (Alfa Aesar, 99.0% purity) was used. Using this powder, the fabrication process illustrated in Figure 2.1 was carried out to produce pure bulk MgB_2. The powder was pressed into round pellets measuring approximately 13 mm in diameter and 1 mm in thickness. A stainless steel tube was then filled with these pellets and sealed at both ends. The tube underwent heat treatment in a tube furnace, where it was heated under a continuous flow of argon gas, as shown in Figure 2.1 below:

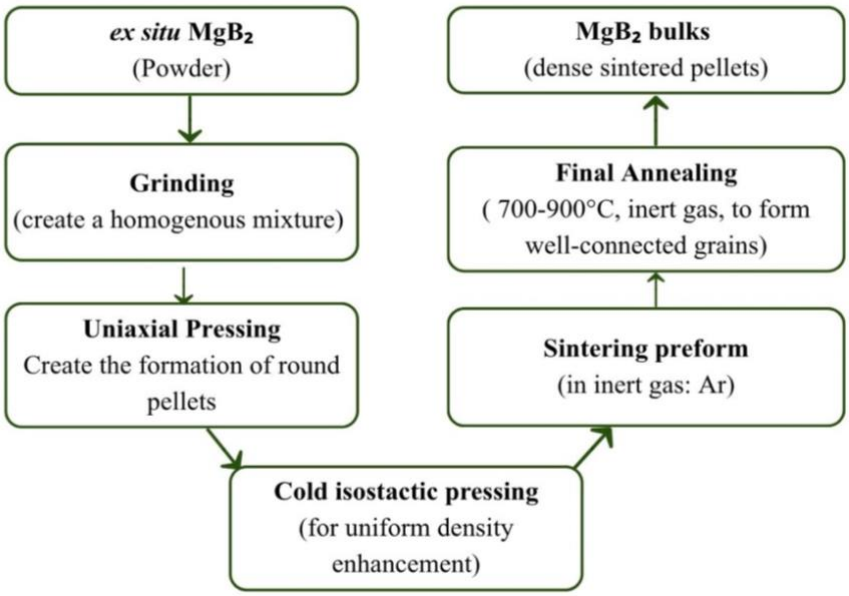


Figure 2.1. *Scheme of fabrication of pure MgB_2 bulks.*

In these experiments, the pure MgB_2 bulks are created by using a sintering temperature of 900 °C for one hour.

2.1.2 Fabrication of (Mg + MgB_2) bulks

Following a procedure similar to that used for the pure bulk MgB_2, samples with Mg addition were fabricated. The starting materials included ex-situ MgB_2 (Alfa

Aesar, 99.0% purity) and Mg (> 99%, R&M Chemicals). These bulk samples were prepared according to the stoichiometry of (Mg + MgB_2). To prepare the Mg-added mixture, 1 mol of ex-situ MgB_2 powder was blended with 0.5 mol of Mg.

To fabricate the Mg-added bulk MgB_2 the powders were thoroughly mixed, compressed into pellets, and then sintered at 900 °C for one hour. These steps are summarized in Figure 2.2.

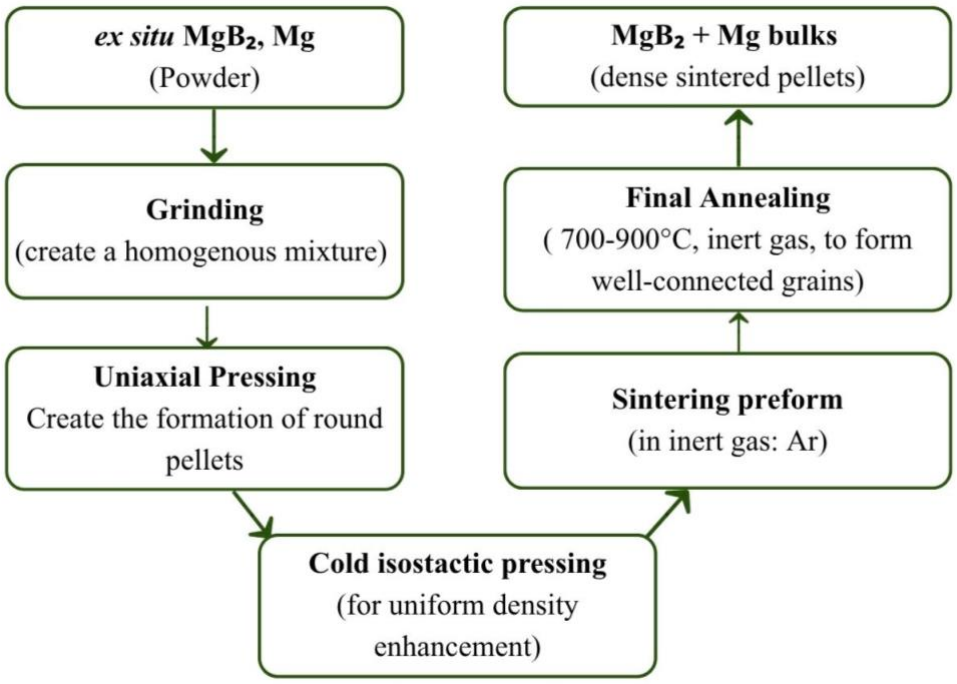


***Figure 2.2**. Scheme of fabrication of (Mg + MgB_2) bulks*

2.1.3 Fabrication of the (y wt.% SiC + Mg + MgB_2) bulks

The starting materials consisted of ex-situ MgB_2 (Alfa Aesar, 99.0% purity), Mg (> 99%, R&M Chemicals), and SiC (99%, 15 nm, nanostructured and amorphous). The fabrication process was identical to that of the (Mg + MgB_2) bulk samples, with the addition of SiC in different proportions. The samples were prepared according to the nominal stoichiometry of (y wt.% SiC + Mg + MgB_2) for y = 0.0, 5.0, 10.0, 15.0, and 20.0.

The respective powders were mixed by hand grinding using a mortar and pestle. The mixture was then pelletized using a press, resulting in pellets of approximately 13 mm in diameter. The density of the green pellets at this stage was approximately 1.8 g/cm^3. The pellets were loaded and sealed into a stainless-steel tube for sintering at 900 °C for 1 h under a continuous argon gas flow. The heating and cooling rates were maintained at 10 °C/min (see Figure 2.3).

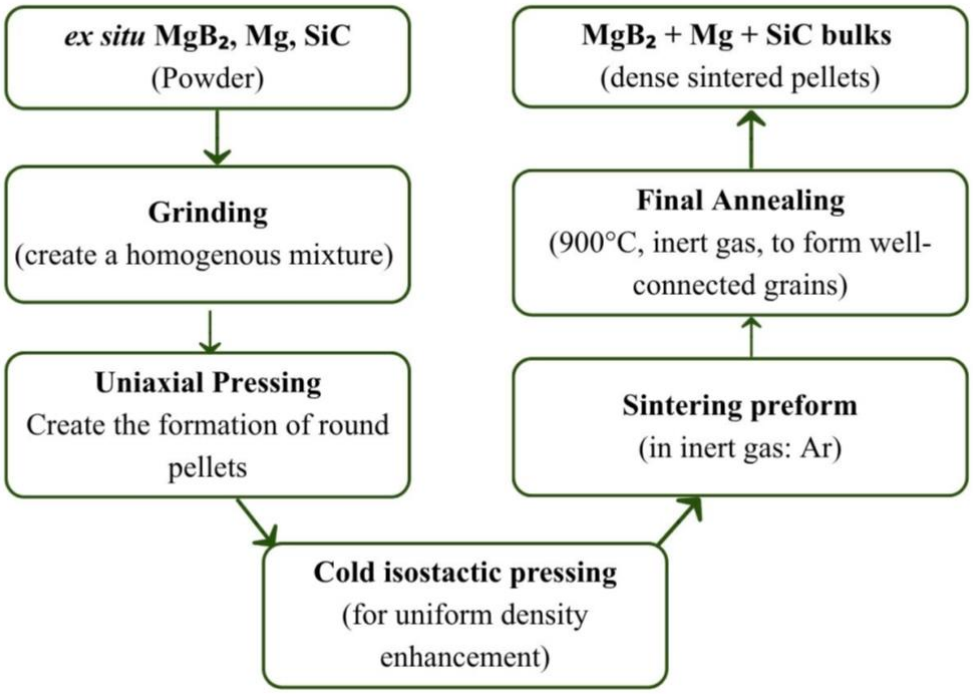


Figure 2.3. *Scheme of fabrication of (y wt.% SiC + Mg + MgB_2) bulks*

The selection of heat treatment conditions is based on previous research aimed at improving grain coupling in the samples. Samples cut into rectangular bars for transport measurements have dimensions of approximately 5 mm × 1.5 mm × 1 mm.

In summary, the prepared sample series include: pure bulk MgB_2, (Mg + MgB_2), and (y wt.% SiC + Mg + MgB_2) configurations for systematic investigation. The research results presented in this dissertation are based on the analysis of sample systems sintered at 900 °C for 1 h, as detailed in Table 2.1.

Table 2.1. *MgB_2 bulks and fabricated conditions*

No	Bulks	Sintering
1	Pure MgB_2	(900 °C - 1 hour)
2	Mg +MgB_2	(900 °C - 1 hour)
3	5% wt. SiC + Mg + MgB_2	(900 °C - 1 hour)
4	10% wt. SiC + Mg + MgB_2	(900 °C - 1 hour)
5	15% wt. SiC + Mg + MgB_2	(900 °C - 1 hour)
6	20% wt. SiC + Mg + MgB_2	(900 °C - 1 hour)

2.2 Fabrication of MgB_2 films

For subsequent investigations, a series of MgB_2 thin films were prepared. The ~400 nm thick MgB_2 films were fabricated on c-cut Al_2O_3 substrates by using the hybrid physical-chemical vapor deposition (HPCVD) technique. The Al_2O_3 substrates and high-purity (99.99%) Mg pieces were placed on a susceptor. The susceptor was inductively heated to 700 °C at 80 Torr under a pure H_2 carrier gas flow at a rate of 80 sccm. Once the temperature stabilized, B_2H_6 gas (5% diluted in H_2) was introduced at a flow rate of 20 sccm to initiate film deposition.

2.2.1 Deposition of pristine MgB_2 films

In this study, the MgB_2 thin films were fabricated using the hybrid physical-chemical vapor deposition (HPCVD) technique, which is widely recognized as a highly effective method for producing high-quality MgB_2 thin films. This technique combines both physical and chemical vapor deposition (PVD and CVD) mechanisms. The HPCVD technique, pioneered by *Xi et al*., enables the high Mg vapor pressure necessary to preserve the thermodynamic stability of the MgB_2 phase at high temperatures.[110,111]

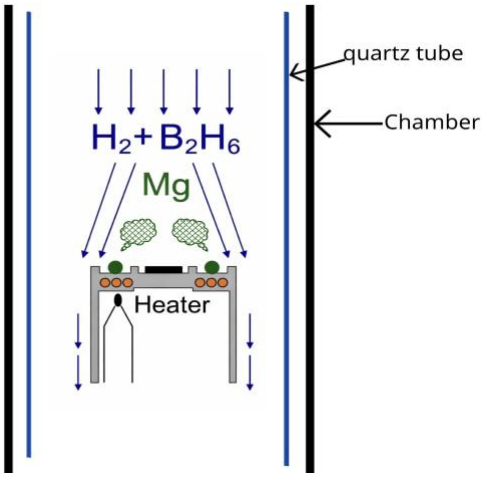


***Figure 2.4**. The scheme of fabricating MgB_2 films in the chamber*

As shown in Figure 2.4, the HPCVD system consists of several key components: a load-lock chamber, an inductively coupled heater, a vertical quartz tube reactor with a bell-shaped inner diameter of 65 mm and a height of 200 mm, a gas inlet and flow control system, a pressure maintenance system, a temperature control system, and a gas exhaust and purification system. The main process chamber is connected to the load-lock chamber at its base, and an induction heater is positioned around and coupled to the exterior of the main process chamber. A susceptor, fabricated from molybdenum (or stainless steel), is positioned coaxially inside the reactor chamber. A gate valve is used to isolate the process chamber from the load-lock chamber. This valve prevents the process chamber from being contaminated during film fabrication.

For the deposition of MgB_2 films, the HPCVD technique utilizes diborane (B_2H_6) as the boron precursor gas and magnesium pieces as the magnesium source. The schematic of the film fabrication process is illustrated in Figure 2.4.

The following is an explanation of the method for fabricating MgB_2 thin films: Initially, the process chamber was purged several times with high-purity argon (Ar) gas (99.99%). Following that, the reactor was loaded with the susceptor, the substrate, and high-purity (99.99%) magnesium chips (2 - 3 mm in diameter). Both the substrate and the magnesium chips on the susceptor were inductively heated to the deposition

temperature under a hydrogen (H_2) ambient pressure. Once the target temperature was reached, the magnesium pieces melted, generating a high vapor pressure near the substrate. After that, the B_2H_6 precursor gas (5% diluted in H_2) was introduced into the chamber, undergoing thermal decomposition at the substrate surface. The following chemical equation describes the reaction between the decomposed precursor atoms and the magnesium vapor to form MgB_2 thin films on the substrate:

$$B_2H_6 + Mg \rightarrow MgB_2 + 3H_2 \quad (2.1)$$

The deposition process was terminated by shutting off the precursor gas flow, followed by cooling the susceptor under a H_2 gas. Single-crystal Al_2O_3 (sapphire) was selected as the substrate due to its hexagonal crystal structure, which matches that of MgB_2, and its high technological relevance.

In general, the growth of the MgB_2 thin films follows the Volmer-Weber (island) growth mode. In this mode, the smallest stable clusters nucleate on the substrate surface and develop in three dimensions, a process known as island formation. Initially, hexagonal MgB_2 islands appear on the substrate. As the process continues, these islands expand and coalesce to form a continuous, thicker film. The detailed deposition process and growth mechanisms have been documented extensively in previous literature [16,113]. This growth behavior typically results in columnar structures within magnesium diboride thin films. Nevertheless, high-quality, nearly single-crystalline MgB_2thin films were successfully fabricated by optimizing the HPCVD growth parameters. The resulting film surfaces are smooth and free of visible grain boundaries, indicating epitaxy driven by the domain-lattice matching between MgB_2 and Al_2O_3.

The specific HPCVD growth conditions setup for these nearly single-crystalline MgB_2 thin films are summarized in Table 2.2

Table 2.2. *Conditions for fabricating of pristine MgB_2 thin films*

Temperature (°C)	710
Pressure (Torr)	210
Flow rate (sccm) H_2 - B_2H_6	100 - 50
Deposition time (minutes)	5
Magnesium amount (g)	2.5
Thickness (nm)	400 - 412

Considering these conditions, the interfacial adhesion between MgB_2 grains and the substrate is enhanced, which in turn assists in the formation of larger single-crystal domains. To undertake a methodical and precise examination into the effects of disorder, it is necessary to utilize high-quality superconducting samples with minimal structural defects. Using these nearly single-crystalline MgB_2 thin films as pristine samples, the primary focus of this study is to investigate the impact of disorder on vortex dynamics. The pristine MgB_2 thin films were fabricated at Sungkyunkwan University (Korea), and their detailed characteristics are presented in the subsequent chapters. Subsequently, the samples were irradiated at the Hanoi University of Science, Vietnam. The technical details of this irradiation process are described in Section 2.2.2.

2.2.2. Ion irradiation of the MgB_2 films

Prior to the laboratory experiments, simulations of the ion irradiation process were performed with two primary objectives: to optimize the irradiation parameters and to predict the defect profiles within the MgB_2 films. The simulations were performed using the licensed Stopping and Range of Ions in Matter (SRIM) software.

Subsequently, the ion irradiation experiments were carried out at room temperature using the HUS-5SDH-2 tandem pelletron accelerator system at the VNU-University of Science, Vietnam, as illustrated in Figure 2.5. The ion energy was

maintained at 1 MeV, with fluences systematically varied at 3×10^{13}, 5×10^{13}, 7×10^{13}, and 9×10^{13} ions/cm^2. The sample designations and detailed specifications of the fabricated films are listed in Table 2.3.



Figure 2.5. *The HUS-5SDH-2 tandem pelletron accelerator system*

Table 2.3. *Ni-ions and Nb-ions irradiated MgB_2 films and ion doses details*

No.	Doses (ions/cm^2)	Film names	Film names
1	0	Pristine	Pristine
2	3×10^{13}	Ni - 3E13	Nb - 3E13
3	5×10^{13}	Ni - 5E13	Nb - 5E13
4	7×10^{13}	Ni - 7E13	Nb - 7E13
5	9×10^{13}	Ni - 9E13	Nb - 9E13

2.3 Sample investigations

2.3.1 X-ray diffraction measurement

X-ray diffraction (XRD) is a method used to analyze the crystalline structure of substances. When X-rays are directed at a crystalline substance, they interact with the atoms in the crystal lattice, resulting in the diffraction or scattering of the X-rays in various directions. The distribution of scattered X-rays may be identified and

examined to ascertain the atomic configuration inside the crystal lattice. Bragg's Law delineates the fundamental link among the wavelength of incoming X-rays, the angle of incidence, and the distance between atomic crystal lattice planes: $n.\lambda_{Cu-K\alpha} = 2\,d.\sin(\theta)$, where n is the reflection order, $\lambda_{Cu-K\alpha}$ is the radiation wavelength, d is the interplanar spacing of the crystal and θ is the angle of incidence.

The crystallite sizes were calculated by Scherrer's formula:

$\tau = \frac{0.9\lambda_{Cu-K\alpha}}{B.\cos\theta}$, ($\tau$ is crystallite size, $\lambda_{Cu\text{-}K\alpha}$ is Cu-K_α wavelength, B is the full width at half maximum (FWHM) and θ is the diffraction angle of the XRD peak).

The lattice constants of MgB_2 were determined for a hexagonal structure by Bragg's law and Miller's indices:

$$\frac{1}{d_{hkl}^2} = \frac{4}{3}\left(\frac{h^2+h.k+k^2}{a^2}\right) + \frac{l^2}{c^2} \qquad (2.2)$$

(d_{hkl} is the interplanar spacing, h, k, l are Miller's indices and a, c are lattice constants)

The XRD patterns of the samples were investigated from 10° to 70° of 2θ using Bruker D8 Advance model using Cu–K_α radiation in VNU University of Science, with wavelength $\lambda_{Cu-K\alpha}$ = 1.5418 Å.

2.3.2 Atomic force microscopy (AFM)

Atomic force microscopy (AFM) is a sophisticated imaging method employed to examine surfaces at the nanometer and atomic scale. In contrast to optical microscopes, which are constrained by light's wavelength, AFM utilizes mechanical interactions between a sharp probe and a sample's surface, enabling exceptionally high spatial resolution. An AFM comprises a cantilever with a finely pointed tip—typically just a few nanometers in width - affixed at its terminus. As the tip traverses the sample surface, forces including van der Waals interactions, electrostatic forces, or repulsive contact forces induce bending of the cantilever. A laser beam reflected from the cantilever detects this minute deflection onto a photodetector. By observing these deflections during raster scanning of the surface, a comprehensive three-dimensional topographic image is generated.

The AFM measurements were performed at the University of Science and Technology of Hanoi, Vietnam Academy of Science and Technology. The obtained topographic images were utilized to investigate the structural alterations within the crystal lattice while confirming that the surface morphology remains virtually unchanged after irradiation.

2.3.3 Resistivity vs. temperature measurement

A Physical Property Measurement System (PPMS, Quantum Design) was used to characterize the transport properties of both bulk and thin-film MgB_2 samples. This system enables the application of magnetic fields up to ±9 T, with a continuously adjustable temperature range from 1.9 K to 400 K. To perform electrical transport measurements, the standard resistivity option of the PPMS was utilized. The resistivity puck configuration accommodates up to twelve independent channels for sample connections. Following the installation of the samples onto the puck, the PPMS probe was subsequently mounted into the system. Furthermore, angle-dependent transport signals can be monitored using a horizontal rotatable puck, allowing precise orientation of the applied magnetic field relative to the sample plane.

2.3.4 Magnetization measurements

Temperature- and field-dependent magnetization measurements were conducted using a cryogen-free PPMS. High magnetic fields and low temperatures were achieved via its integrated superconducting magnet and cryostat, while various measuring probes allowed the recording of multiple physical properties. From the obtained magnetization hysteresis (M - H) loops, the critical current density J_c was derived using Bean's critical state model.

According to Bean's model, superconducting filaments either carry their full critical current or no current at all. As the external magnetic field increases and overcomes the surface barrier, magnetic flux penetrates the sample, inducing critical currents in filaments progressively closer to the center. When the field is reduced to zero, trapped flux maintains current flow throughout the filaments. Applying a

magnetic field in the opposite direction gradually reverses the direction of these critical currents.

By using the Ampere's law: $\boldsymbol{\nabla} \times \mathbf{B} = \mu_0 \mathbf{J_c}$ and the magnetic flux density expression: $B = \frac{1}{V}\int Hdv$, the Bean's formula was defined as J_c = 30 ΔM/d, where $\Delta\mathbf{M} = \mathbf{M}^+ - \mathbf{M}^-$ represents the width of the hysteresis loop, and d is the characteristic length.

For the bulks, the Bean's model has been revised as follows[6]

$$J_c = \frac{20\Delta M}{a\left(1-\frac{a}{3b}\right)} \tag{2.3}$$

where a and b represent the sample dimensions perpendicular to the magnetic field. The practical estimate of $\mathbf{M^+}$, $\mathbf{M^-}$, and $\mathbf{\Delta M}$ was delineated inside the hysteresis loop..

For the thin film samples, the Bean's model has been revised as follows [6]

$$J_c = \frac{30\Delta M}{r} \tag{2.4}$$

where r denotes the radius associated with the entire area of the film surface oriented perpendicular to the magnetic field, and ΔM represents the height of the M-H curves.

In this work, PPMS measures are taken in the Center of Nano and Energies, Faculty of Physics, VNU-Hanoi University of Science.

2.3.5 Raman spectroscopy

Even though the boron plane is the source of MgB_2 superconducting capabilities, the Raman active mode, which is denoted by the symbol E_{2g}, has a significant connection to the electronic transport of bands. It is thus possible to conduct an efficient investigation of the E_{2g} mode by using the Raman spectrum, which has the potential to provide useful information on crystal symmetry, particle size, and impurities. Using an incident green laser with a wavelength of 531.97 nm, a grating of 600 g/mm, and a Raman shift range of 200 - 1000 cm^{-1}, the WITec Micro-Raman Spectrometer System (model ALPHA300 M) was used in order to analyze the Raman spectra at room temperature.

According to the McMillan formula [71], the average phonon frequency and critical temperature are inversely related. Therefore, the active frequency of the phonon of the E_{2g} mode in MgB_2 has an analogous effect on T_c fluctuation. The BCS theory was assessed using the McMillan formula, which has been updated by Allen-Dynes, in order to fully comprehend the contribution of the E_{2g} mode to the T_c value in our MgB_2 samples:

$$T_c = \frac{\langle \omega_{log} \rangle}{1.2} \exp\left(-\frac{1.04(1+EPC)}{EPC-\mu^*(1+0.62\times EPC)}\right) \quad (2.5)$$

where $\langle \omega_{log} \rangle = (690 \times \omega^2 E_{2g} \times 390)^{0.25}$ is the E_{2g} mode average phonon frequency, with a value of 390 cm^{-1} along with 690 cm^{-1} being the phonon frequency of the other modes in the MgB_2 superconductor system. EPC illustrates the electron -phonon coupling (EPC) constant, and the value of μ*, the Coulomb pseudo potential, is assumed to be 0.13, see Meletov et al. [73]

2.4 Conclusion of chapter 2

In this chapter, the fabrication of the MgB_2 samples for the research, including three bulk and film samples were presented. Additionally, the measurements required to investigate the crystal and superconducting properties, such as XRD, Raman spectroscopy, measurements performed on PPMS were introduced. The results will be presented in the following chapters, sequentially according to the gradual improvement of the material's superconductivity.

Chapter 3. ENHANCEMENTS OF SUPERCONDUCTING PROPERTIES IN MAGNESIUM DIBORIDE BY CO-ADDITION OF MAGNESIUM AND SILICON CARBIDE

As introduced in Chapter 1, magnesium diboride (MgB_2) has attracted significant attention for large-scale practical applications, including the fabrication of superconducting wires and cables, magnetic resonance imaging (MRI) systems, fault current limiters (FCLs), and next-generation wind turbine generators. In recent years, extensive research efforts have been dedicated to overcoming the intrinsic limitations of pure MgB_2, particularly the rapid degradation of its critical current density J_c under high external magnetic fields. To mitigate this issue, researchers have focused on modifying the material's chemical composition and microstructure through various chemical doping strategies, aiming to introduce effective artificial pinning centers and alter the upper critical field (B_{c2}) [1,7]. Recent literature has demonstrated that chemical additives play a multi-functional role in the matrix. For instance, the concurrent insertion of B_4C and Dy_2O_3, combined with an excess of 5 mol Mg, has been proven to significantly improve the overall superconducting characteristics of MgB_2 [6]. The excess Mg compensates for the volatility of magnesium during high-temperature sintering, thereby reducing the formation of unwanted secondary phases and improving grain connectivity. Furthermore, rare-earth oxide doping, such as the incorporation of Sm_2O_3 into MgB_2 wires, has shown prominent success within the medium temperature range of 15 K to 30 K. This additive induces localized microstructural modifications, generating nanoscale defects that enhance flux pinning efficiency and consequently accelerate the enhancement of J_c. [28].

Among various dopants, silicon carbide (SiC) remains one of the most effective agents for introducing intra-grain defects. When SiC-added MgB_2 wires are processed under high isostatic pressure (HIP), the combined effects of chemical substitution and mechanical pressing result in a substantial increase in core density,

the complete elimination of microscopic voids, and the facilitation of tiny secondary phase precipitates [30]. These nanoscale precipitates serve as highly powerful pinning sites that effectively constrain vortex motions in intense magnetic fields. Beyond material-level doping, structural and thermal management at the coil level also represents a critical research direction; for example, the impregnation of MgB_2 coils with solid nitrogen (SN_2) has emerged as a novel solution. This approach markedly enhances the thermal stability and mechanical integrity of the superconducting coils, ensuring that they maintain outstanding electrical performance even when subjected to thermal fluctuations or excessive operating temperatures. [79]

Comprehensive literature reviews on the historical development of MgB_2 superconductors reveal that chemical adding remains the primary and most viable methodology for enhancing the superconducting performance of bulk samples. Historically, investigations into the ion irradiation of bulk MgB_2 largely concluded around 2013[17]. A critical synthesis of over 30 research outcomes from that era demonstrated that physical irradiation yielded no substantial improvements in MgB_2 bulks. This lack of efficacy is fundamentally attributed to a significant dimensional mismatch: the projected penetration range of accelerated ions is restricted to mere thousandths of the total bulk thickness, leaving the vast majority of the inner material matrix unaffected. Consequently, physical ion bombardment is structurally inefficient for three-dimensional bulk forms, shifting the scientific focus entirely toward uniform chemical modification.

Despite these processing constraints, MgB_2 bulks continue to be an active area of contemporary research and industrial development. This enduring interest is driven by its immense potential for practical applications, underscored by significant advantages in economic feasibility, low raw-material costs, and straightforward fabrication technologies. Numerous studies have established that adding MgB_2 with carbon-based compounds introduces strong intra-grain pinning defects, which dramatically enhances in-field flux pinning capability. Moving beyond binary systems, this research investigates a synergistic dual-doping strategy by

simultaneously incorporating both excess Mg and nanostructured SiC into the MgB_2 bulks. The inclusion of excess Mg is strategically intended to compensate for magnesium volatility during high-temperature processing, thereby optimizing grain connectivity and suppressing the formation of non-superconducting secondary phases. Concurrently, the addition of nanostructured SiC is utilized to introduce nanoscale structural defects and localized lattice strain, which significantly reinforces flux pinning efficiency and enhances mechanical integrity for industrial conductor manufacturing.

Building upon prior investigations conducted on grain boundary coupling optimization, a specific, highly controlled heat treatment profile was established as the baseline for sample processing, see [20]. The comprehensive sample configurations and designations investigated in this chapter are systematically summarized in Table 3.1. To ensure structural homogeneity and consistent phase evolution, the sintering parameters for all synthesized sample series were strictly maintained at a fixed temperature of 900 °C for a continuous duration of 1 h under an inert atmosphere.

Table 3.1. *The series of bulk MgB_2 and fabrication conditions*

No	Bulk MgB_2	Conditions of sintering
1	Pure MgB_2	900 °C - 1 hour
2	Mg + MgB_2	900 °C - 1 hour
3	5% wt. SiC + Mg + MgB_2	900 °C - 1 hour
4	10% wt. SiC + Mg + MgB_2	900 °C - 1 hour
5	15% wt. SiC + Mg + MgB_2	900 °C - 1 hour
6	20% wt. SiC + Mg + MgB_2	900 °C - 1 hour

This section evaluates the collective influence of adding 0.5 mol Mg in conjunction with various weight percentages of SiC to systematically investigate their effects on the superconducting properties of MgB_2 bulks focusing specifically on the evolution of critical parameters such as J_c, T_c, and B_{c2}. In comparison to pure MgB_2, the baseline values of T_c, J_c, and B_{c2} for the (Mg + MgB_2) bulk configuration exhibit noticeable elevation.

However, experimental findings indicate that the J_c of the co-added samples diminishes with an increase in the SiC adding concentration. Furthermore, upon a detailed comparison of the B_{c2} trends, the (Mg + MgB_2) bulk exhibits the highest magnitude of B_{c2} values among all bulk samples. Properly adjusting these chemical design parameters and understanding the variation of these characteristics may substantially refine the in-field performance of MgB_2 bulk superconductors, providing a more robust framework for developing efficient superconducting parameters for practical industrial applications, [50,58].

3.1 Investigation of critical temperature in (SiC + Mg + MgB_2) bulks

To systematically evaluate the thermodynamic and electronic response of the co-added magnesium diboride system, the temperature dependence of electrical resistivity ρ(T) was characterized under various external magnetic fields (B) up to 6T, applied perpendicular to the sample surface. Figure 3.1 illustrates the in-field ρ(T) curves for both the pristine reference and the co-added (y wt.% SiC + Mg + MgB_2) bulk configurations. As observed in Figure 3.1, the T_c exhibits a monotonic shift toward lower temperatures with increasing magnetic field strength. This field-induced suppression of T_c is fundamentally governed by the orbital depairing mechanism typical of Type-II superconductors. The external magnetic field penetrates the material matrix in the form of quantized flux vortices; as the field strength intensifies, the density of these vortices increases, which progressively suppresses the superconducting order parameter and reduces the density of superconducting Cooper pairs until superconductivity is completely extinguished near the B_{c2}.

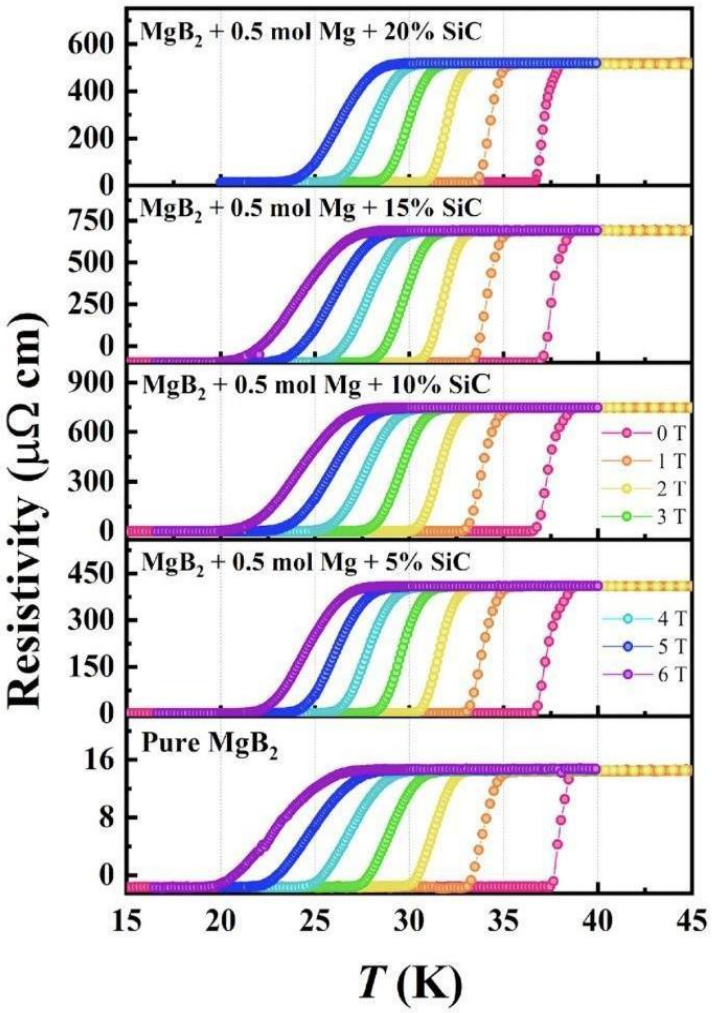


Figure 3.1. *Plot of in-field resistivity versus temperature of MgB_2 bulks*

According to the evaluation methodology shown in Figure 3.2, the T_c values were determined at the onset of the electronic transition from the normal metallic state to the zero-resistance superconducting state. The experimental data reveals that the (Mg + MgB_2) bulk displays the maximum T_c of approximately 38.57 K. This elevated transition temperature indicates that the addition of 0.5 mol excess Mg successfully compensates for the volatile loss of magnesium during high-temperature solid-state sintering. By mitigating the formation of magnesium vacancies within the crystal lattice, the nominal stoichiometry is preserved, which enhances inter-grain connectivity and minimizes the presence of non-superconducting secondary phases.

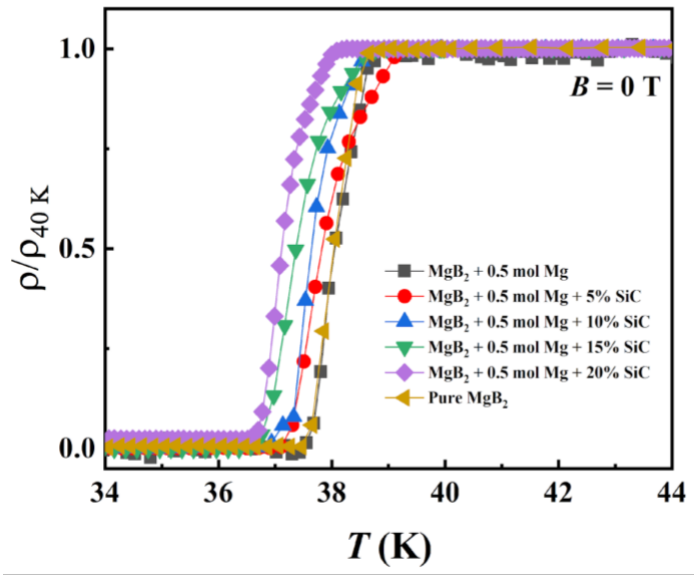


Figure 3.2. *Normalized zero-field resistivity ($\rho/\rho_{40\,K}$) versus temperature of the MgB_2 bulks*

Conversely, the introduction of nanostructured SiC induces a systematic decline in T_c, reaching the lowest value of approximately 37.12 K for the highest doping concentration (20 wt.% SiC + Mg + MgB_2). This concentration-dependent degradation of T_c can be explained through two distinct physical mechanisms. First, at the atomic level, a portion of the carbon atoms from the decomposed SiC replaces boron atoms within the honeycomb lattice layers $Mg(B_{1-x}C_x)_2$. Because MgB_2 is a two-band superconductor driven by two distinct energy gaps (the strong two-dimensional σ-band and the weaker three-dimensional π-band), the substitution of carbon introduces extra electrons into the system. This electron doping alters the filling of the σ-band and introduces structural disorder, which accelerates intraband and interband electron scattering, thereby reducing the superconducting pairing strength. Second, at the microstructural level, the excess Si and unreacted carbon tend to aggregate at the grain boundaries, leading to the formation of secondary impurity phases such as Mg_2S_i and MgB_4. As summarized in Table 3.2, these secondary phases induce a substantial drop in grain size, a reduction in grain connectivity, and a noticeable degradation in overall crystallinity.

Nevertheless, it is highly crucial to note that this reduction in T_c remains remarkably small, with all dual-doped samples maintaining a T_c above 37 K. This value is exceptionally close to both the pure sample and the theoretical bulk limit of 39 K. The preservation of such a high transition temperature demonstrates that the dual-doping technique successfully limits excessive carbon substitution into the lattice core while utilizing the nanostructured defects effectively. Consequently, this well-balanced compromise between defect engineering and phase purity represents a significant success in maintaining high-T_c performance for practical superconductivity applications.

3.2 Enhancements of upper critical fields of (SiC + Mg + MgB_2) bulks

The physical mechanism driving the enhancement of the B_{c2} in the (SiC+Mg+ MgB_2) bulks, despite the slight degradation of T_c, can be comprehensively explained through the dirty-limit superconductor theory within the Ginzburg-Landau framework.

According to the standard Ginzburg-Landau relation, MgB_2 is inversely proportional to the square of the superconducting coherence length (ξ), expressed as $B_{c2}(0) = \Phi_0/2\pi\xi^2$., where Φ_0 represents the flux quantum.

In pure MgB_2, the material behaves as a relatively clean-limit superconductor with a long electron mean free path l. However, when nanostructured SiC is introduced, the thermal decomposition of SiC facilitates the atomic substitution of carbon into the boron lattice sites, forming $Mg(B_{1-x}C_x)_2$. This substitution introduces a high density of structural disorder and local lattice strain within the boron honeycomb layers. At the electronic level, this intra-grain disorder induces strong intraband scattering, particularly within the two-dimensional σ-band, which drastically shortens the electron mean free path l.

When l becomes significantly shorter than the intrinsic coherence length ($l \ll \xi(0)$), the superconductor transitions into the "dirty limit." In this regime, the effective coherence length is governed by the dirty-limit approximation, ξ =

$\sqrt{\xi(0).l}$. Consequently, the substantial reduction in the electron mean free path l forces a contraction of the effective superconducting coherence length ξ. Because B_{c2} is inversely related to ξ^2, this spatial contraction of the Cooper pair coherence scales up the material's ability to withstand intense external magnetic fields, thereby leading to a dramatic enhancement of B_{c2} at low temperatures. This successful manipulation of the scattering rates demonstrates that defect engineering via SiC addition effectively optimizes high-field performance, making the material highly suitable for practical high-field industrial applications.

The two-band Ginzburg - Landau (GL) hypothesis provided a description of all $B_{c2}(T)$ curves [3]:

$$B_{c2} = B_{c2}(0)\frac{\theta^{1+\alpha}}{(1-(1+\alpha)\omega+l\omega^2+m\omega^3)} \quad (3.1)$$

where $\theta = \left(1-\frac{T}{T_c}\right)$; $\omega = (1+\alpha)\theta^{1+\alpha}$, and B_{c2} (0) is the value of B_{c2} at T = 0 K. Through the process of experimentation, the simple expressions α, l, and m are discovered [2]. For the best possible fit, the values of m = -1, l = 3, and α = 0.23 are achieved. It is necessary to use a resistivity threshold that is equivalent to fifty percent of the superconducting transition in order to ascertain the values of B_{c2}. [15]. For the pure and (SiC + Mg + MgB_2) bulks that were supplied, the B_{c2} of each sample is presented versus T in Figure 3.3.

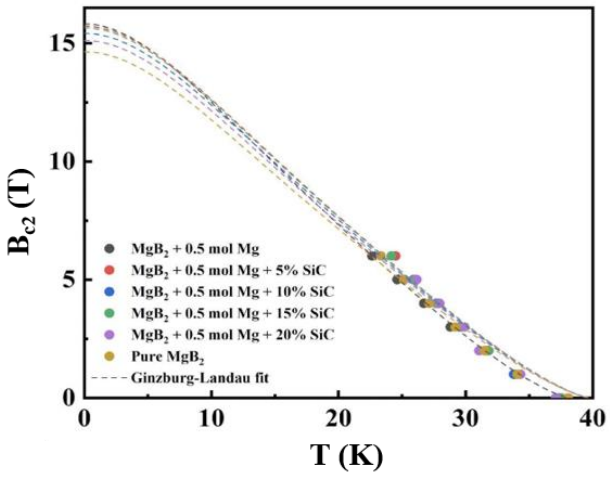


Figure 3.3. *The B_{c2} versus temperature for pure and (SiC + Mg + MgB_2) bulks*

The solid lines that represent the B_{c2} (T) fitting curves of all bulks are shown in Figure 3.3. By projecting the B_{c2} (T) curves to a temperature of 0 K, the value of B_{c2} (0) for pure MgB_2 bulk is determined to be 14.64T. The B_{c2} value in (y wt.% SiC + Mg + MgB_2) bulks falls as the wt.% SiC rises, particularly from 15.72T for (5% SiC + Mg + MgB_2) bulk to 15.12T for ((20% SiC + Mg + MgB_2) bulk (Table 3.2). This value reached its highest point of 15.82T for the bulk of (Mg + MgB_2) bulk. One possible explanation for this is that the impurity scattering rate has risen as a consequence of co-additions. On the other hand, the increasing inter- and intra-band scattering is responsible for the shortening of the mean free path and the coherence length, which is why the values of B_{c2} of all added samples are increased.

***Table 3.2**. T_c and B_{c2} of pure and (SiC + Mg + MgB_2) bulks*

No	Bulks	T_c (K)	B_{c2} (T)
1	Pure MgB_2	38.09	14.64
2	Mg + MgB_2	38.57	15.82
3	5% wt. SiC + Mg + MgB_2	37.83	15.72
4	10% wt. SiC + Mg + MgB_2	37.64	15.42
5	15% wt. SiC + Mg + MgB_2	37.37	15.65
6	20% wt. SiC + Mg + MgB_2	37.12	15.12

3.3 Enhancements of critical current density in (SiC + Mg + MgB_2) bulks

The values of J_c of pure and (SiC + Mg + MgB_2) bulks are deduced by analyzing the magnetization hysteresis loops measured at T=10 K, 15 K, 25 K, and 30 K, applying the modified Bean's model [7,6,14]. The magnetic response of the sample is measured during this procedure, which is carried out when the sample is exposed to an external magnetic field. In particular, the equation that has to be employed to compute is as follows:

$$J_c = \frac{20\Delta M}{\left[a\left(1-\frac{a}{3b}\right)\right]} \tag{3.2}$$

where ΔM represents the breadth of the magnetization hysteresis, and a and b represent the diameters of the cross-section of rectangular bulks that are perpendicular to the magnetic field that is being applied. In Figure 3.4, the magnetic field dependence of J_c is depicted on a double-logarithmic scale for both the pure and (SiC + Mg + MgB_2) bulks at various values of T. This displays the relationship between J_c and the magnetic field.

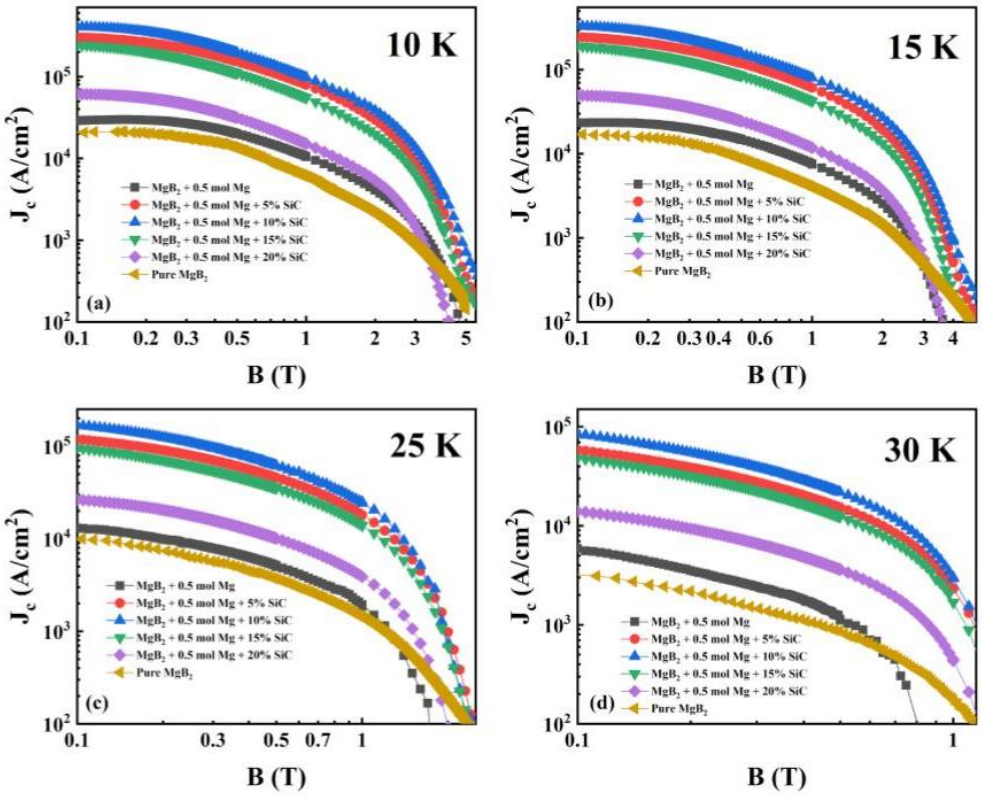


Figure 3.4. *J_c of pure and (SiC + Mg + MgB_2) bulks at 10 K, 15 K, 25 K, and 30 K*

Clear increases of in-field J_c were recorded at all temperatures where the experiment was conducted. The value of in-field J_c in the (Mg + MgB_2) bulk sample is much larger when compared to the value of pure MgB_2. The values of J_c of the (y wt.% SiC + Mg + MgB_2) bulk samples showed a prominent rise when SiC was introduced as a second impurity. This enhancement was clearly observed in configurations where 5 wt.% and 10 wt. % of SiC was present.

On the other hand, the value of J_c began to decline in the bulks when adding more SiC, for example J_c of (15%SiC + Mg + MgB_2) bulk and (20%SiC + Mg + MgB_2) tend to decrease toward the J_c of the pure bulk. In the presence of a significant quantity of impurity, the amount of superconducting phase is diminished, or weak pinning centers are produced.

3.4 Pinning mechanism in the pure and (SiC + Mg + MgB_2) bulks

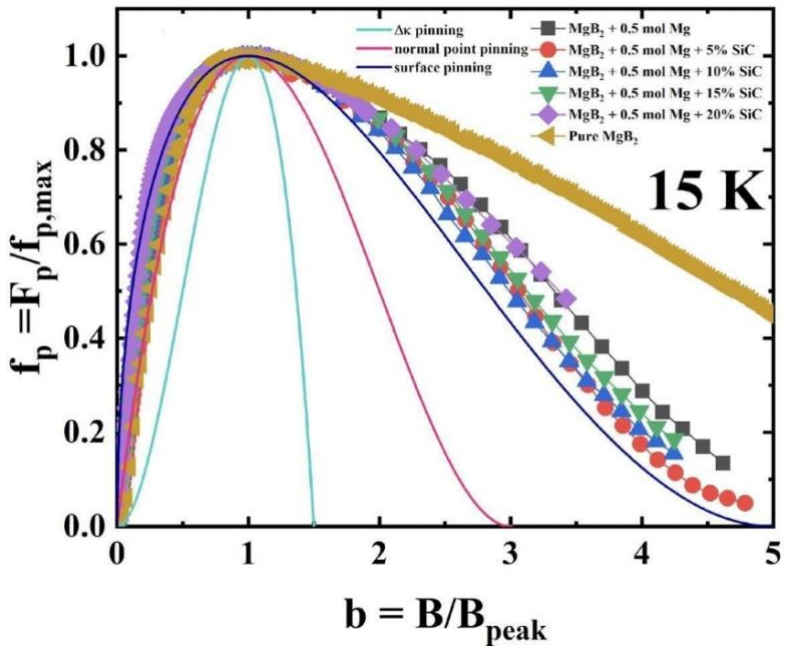


Figure 3.5. *Normalized pinning force density $f_p = F_p/F_{p,max}$ versus reduced field b ($b = B/B_{peak}$) of pure and (SiC + Mg + MgB_2) bulks at 15 K*

The magnetic field dependence of the flux pinning force density, F_p, in MgB_2 bulks superconductors under a variety of sample preparation conditions is evaluated in order to get a comprehensive understanding of the impact that doping SiC has on the characteristics of flux pinning in MgB_2 bulks. One may acquire the F_p values by using the formula $F_p = B \times J_C$, which F_p is derived from the data of $J_c(B)$. The theoretical model was used in order to explore the pinning mechanism in both the pure and (SiC + Mg + MgB_2) bulks. The normalized pinning force density (f_p =

$F_p/F_{p,max}$) is shown in Figure 3.5 as a function of the normalized magnetic field (b = B/B_{peak}). The magnetic field B_{peak} represents the magnetic field in which the flux pinning force ($F_{p,max}$) reached its highest value. The most relevant study on $F_p(b)$ identified the primary pinning mechanism, in addition to the fact that it boosted strength. In order to characterize the three distinct types of pinning, the following equations are provided.

The following equations describe the three different kinds of pinning [36]:

For surface pinning:

$$f_p(h) = \frac{25}{16}\sqrt{h}\left(1 - \frac{h}{5}\right)^2 \tag{3.3}$$

For normal point pinning:

$$f_p(h) = \frac{9}{4}h\left(1 - \frac{h}{3}\right)^2 \tag{3.4}$$

For ΔK pinning:

$$f_p(h) = 3h^2\left(1 - \frac{2h}{3}\right) \tag{3.5}$$

In the pure and (Mg + MgB_2) bulks, the curves of $F_p(b)$ at T = 15 K deviated from the three pinning models that were described before. This was due to the implications of vortex-vortex interactions as well as the absence of pinning centers. By increasing the amount of doping, it was discovered that the pinning mechanism progressively shifted to surface pinning at a temperature of 15 K. For samples that were doped with SiC, surface pinning proved to be an excellent method for determining the $f_p(b)$ at 15 K, particularly for the (10% SiC + Mg + MgB_2)) bulk.

In order to get the comparison, the pinning process is re-confirmed by using the Dew-Hughes model with the formula of $f_p = Ab^p(1\text{-}b)^q$ [19] In this model, the normalized field b is assumed to be equal to B/B_{irr}, while p and q are fitting parameters that indicate the dominant pinning [57]. In order to calculate the value of B_{irr}, which stands for irreversibility field, the field at which J_c is 100 A/cm^2 is used. The core pinning was supposed to correspond to the value of q = 1, according to the

theory. The core surface pinning was represented by the value of p = 0.5, while the core point pinning was represented by the value of q = 1.

The results of the fitting are shown in Figure 3.6. The recorded value of bpeak is around 0.22, while the average value of p is approximately 0.65, which is derived from the curves that provide the best match. When the values that were obtained are compared, it is found that they are somewhat compatible with the assumption that core surface pinning exists. Based on these findings, it can be concluded that surface pinning, which is mostly associated with grain boundaries, is the predominant form of pinning in the samples that include SiC [32,33,38,80].

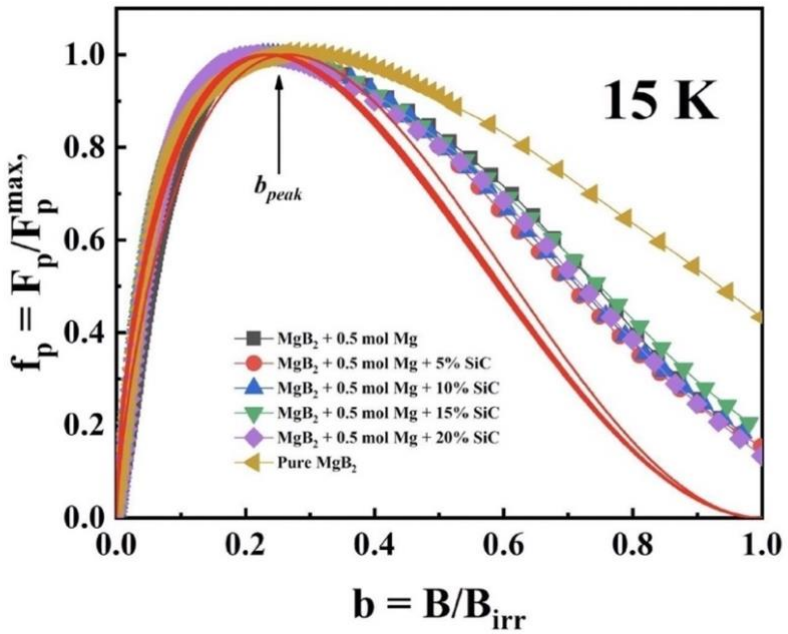


Figure 3.6. *Flux-pinning mechanism in pure and (SiC + Mg + MgB_2) bulks fitted by Dew-Hughes model*

The natural form of the intrinsic pinning centers is pinned by the grain boundaries in MgB_2 polycrystalline materials, as shown by prior study[80]. It is possible that the addition of 10% SiC may boost the effect of surface pinning. This is because the additive will fill the gaps and improve the connection between the MgB_2 grains.

3.5 Conclusion of chapter 3

The superconductivity of MgB_2 bulks improve in all of samples:

The critical temperature T_c peaks in the (Mg + MgB_2) bulk, then decreases as % wt. SiC concentration rises, reaching its minimum at 20% SiC. The slight decreasing of T_c approximately of pure bulk when co-added SiC and Mg indicates the ability to maintain T_c more than 30 K after addition, relative high quality.

Similarly, the upper critical field B_{c2} reaches a maximum of 15.82T in the (Mg + MgB_2) bulk and remains at higher values as the % wt. SiC rises, when compared to this value of the pure bulk sample.

The J_c in all samples after co-added SiC+Mg reveals the enhancements, especially in the samples which %SiC change from 5-15%. The highest enhancement of J_c was witnessed in (10% wt. SiC + Mg + MgB_2) bulk.

At 15 K, after addition, the dominated pinning mechanism is surface pinning. This mechanism fits well with the reduced pinning force $f_p(b)$ for the (y % wt. SiC + Mg + MgB_2) bulks, particularly for the (10% wt. SiC + Mg + MgB_2) bulk.

To sum up, this research can enhance the superconductivity of materials. However, these materials do not have superior superconducting properties because the surface pinning indicates enhancement of J_c in low-fields, these are the causes and motivations to conduct other research later to more enhance J_c in high fields of MgB_2 for practical application.

Chapter 4. INVESTIGATION OF THE CRYSTAL STRUCTURE AND SUPERCONDUCTING PROPERTIES IN MAGNESIUM DIBORIDE USING IRRADIATION OF NIOBIUM IONS

In the previous chapter, series of studies in MgB_2 bulks were conducted. These studies may contribute to various applications. However, in recent years, many modern medical machines require devices that behave with high superconducting properties, especially high value of J_c and B_{c2}. Therefore, it is necessary to acquire better results in enhancements of superconductivity by fabricating MgB_2 films. Fortunately, the trendy methods known globally as "irradiation" have proven to yield a number of superior results in advanced materials. Thus, this advanced method was used to fabricate a series of defects, that contributed as pinning centers in MgB_2 films.

Regarding MgB_2, this material has T_c ~ 39 K, along with its uncomplicated hexagonal crystal structure, low mass, and robust resistance to chemical substitutions and structural imperfections, has significantly enhanced its appeal as a low-temperature superconductor [75,100,104]. Consequently, MgB_2 has gained significant popularity. Conversely, MgB_2 often exhibits reduced efficiency due to its inadequate intrinsic vortex pinning. The value of J_c diminishes rapidly when the magnetic field intensifies due to these processes [23,88]. The grain boundaries and lattice defects in pure MgB_2 superconductors are considered the principal factors contributing to the substantial pinning mechanism in these materials. When these defects are subjected to significant Lorentz forces, they are inadequate to immobilise vortices [23,88]. This is often the case. The creation of artificial pinning centers (APCs) by chemical doping, nanoparticle incorporation, mechanical deformation, and particle irradiation has been extensively researched to circumvent this limitation. APCs, composed of non-superconducting inclusions, strain fields, and defect clusters, serve as efficient vortex pinning sites when their characteristic size aligns with the superconducting coherence length (ξ) or the London penetration depth (λ). This approach leads to a substantial improvement in the field-dependent J_c, as seen in

references [22,25]. Ion irradiations have evolved into a highly successful technology that allows for complete control by the user. This approach aims to produce APCs in MgB_2. The choice of irradiation ions is crucial for precisely assessing the density of produced flaws. This advantage is due to the accurate specification of fault density. This benefit is also due to Nb ions' capacity to produce regulated lattice disorder and establish effective pinning sites in MgB_2 films. Consequently, they are used for irradiation purposes. The films do this while maintaining their overall crystal structure and inherent superconducting characteristics. When electronic stopping mechanisms are used, heavy ions with high atomic numbers may suffer significant energy loss. Ion tracks and lattice aberrations are two examples of defect structures that may arise from this potential. Both structures exemplify flaws. Light ions, including hydrogen, oxygen, and iron, mostly contribute to the majority of produced flaws. The predominant types of these faults are point defects. Conversely, it is anticipated that denser ions, such as nitrogen, would lead to the development of defect structures that are more spatially extended. The typical widths of these flaws are increasingly approaching the superconducting coherence length, indicating their growing use for vortex inversion. Moreover, the defect density of Nb ions is much lower than that of other heavy ions, such as Fe [107] or Sn [63]. This facilitates the identification of a compromise between preserving superconductivity and improving flux pinning. Empirical research has proven that irradiation with heavy ions has similar effects on many functional materials, including piezoelectric and oxide systems. These effects have also been seen to be analogous. Stress fields and defect tracks are generated in these systems due to processes induced by electrical halting. These mechanisms are fundamental to the issue. The material's physical characteristics are substantially modified due to these transformation processes. The irradiation of thin films composed of $MgB_2$with niobium ions is expected to create a defect landscape that may be optimised to provide superior superconducting performance [89,102].

This study aims to identify the optimal defect concentrations that may decrease T_c suppression while enhancing high-field performance. This will be achieved by a thorough examination of the magnetic-field dependence of J_c under various Nb-ion irradiation conditions. Furthermore, XRD and several spectroscopic methods are used to enhance the comprehension of the structural disorder induced by irradiation. A correlation exists between the lattice disorder resulting from this scientific activity and the alterations in superconducting properties. This study aims to assess the effectiveness and scalability of Nb-based defect engineering for thin-film and device applications by comparing Nb ion irradiation with current APC procedures. The assessment will be conducted to evaluate the efficacy of Nb-based flaw engineering. The methods used in these activities include chemical doping, irradiation with iron and tin ions, and other analogous approaches.

In this chapter, the most important results include the following: I investigate the effects of Nb ion irradiation on the electron - phonon coupling, as well as the structural and flux pinning characteristics of MgB_2 thin films that have been deposited on c-cut Al_2O_3 substrates using hybrid physical chemical vapour deposition (HPCVD). The MgB_2 films, measuring around 400 nm in thickness, undergo Nb-ion irradiation with 1 MeV at doses ranging from 3×10^{13} to 9×10^{13} ions/cm². All manufactured MgB_2 films are demonstrated to be orientated along the c-axis through the analysis of the XRD pattern. Raman spectroscopy reveals that as ion dose increases, the E_{2g} phonon mode diminishes, while the features of the phonon density of states rise. This indicates a reduction in the interaction between electrons and phonons, along with an increase in lattice disorder. The value of T_c was defined as the onset temperature for superconductivity, which decreases from 39.56 K in the pristine MgB_2 film to 36.25 K at the highest level of irradiation dose. Even with the reduction of T_c, the Nb-ion irradiations significantly enhance the value of J_c of at high field regions. For irradiation doses of 3×10^{13} and 5×10^{13} ions/cm², the values of J_c of the Nb-ion irradiated films surpass that of the pristine film at crossover fields of approximately 2 - 2.5T and around 3T, respectively. The examination of the

pinning force shows a gradual shift from primarily surface pinning in the unaltered film to a combination of surface and point pinning in the irradiated films, linked to the creation of point-like defects due to irradiation. The results indicate that Nb ion irradiation serves as an effective method for modifying vortex pinning in MgB_2 thin films, thereby improving their performance in strong magnetic fields through the introduction of controlled defects.

4.1 Simulation of the Nb-irradiation processes

To prepare for the experiment, it is required to simulate the irradiation of MgB_2 films with a thickness of around 400 nm. The licensed SRIM software facilitates this simulation.

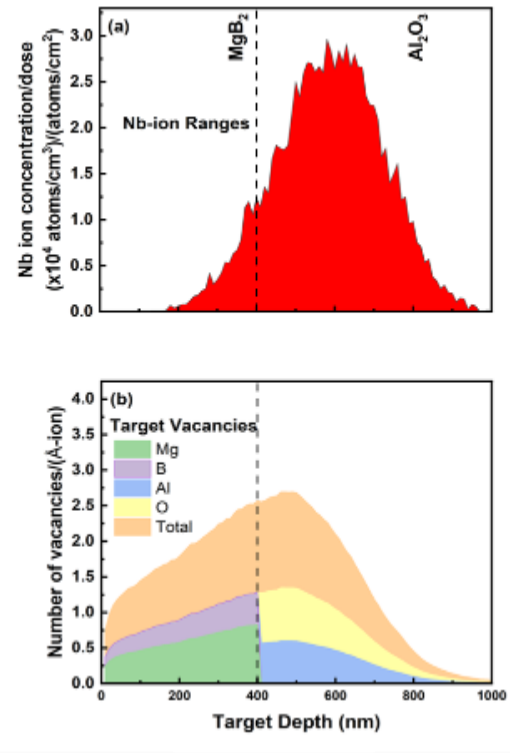


Figure 4.1. *(a) Mean projected range and (b) vacancy depth profile for 1 MeV Nb-ion irradiated MgB_2 film on c-cut Al_2O_3 substrate.*

The production of Nb ions is critical for carrying out this simulation. The simulation has a density of 2.57 g/cm³, and the Nb ion, which is energising at 1 MeV. The anticipated ion range (R_p) is calculated using the same approach as the film

thickness, as illustrated in Figure 4.1(a). This suggests that a significant proportion of the Nb ions fail to completely penetrate the MgB_2 films, conserving their energy inside. Most of the Nb ions lie on the substrate at the depth of about 600nm, near the films. This Nb distribution reveals that a significant number of Nb ions may lie in the films, therefore the films may have uneven point defects. Simulation in films also showed that irradiation-induced defects are mostly associated with lattice variations and atomic displacements inside the MgB_2 films, as shown by these reflections, which suggest that any damage caused by irradiation is quite modest. Figure 4.1(b) illustrates that the number of vacancies in irradiated films may be uneven; they gather more in the depth of film near the substrace. Therefore, the investigations of crystal structure also may not give clearly results. Due to the presence of such strain and distortions may be introduced into the crystal lattice, which might potentially have effects on the superconducting properties. The interaction of high-energy ions with thin films induces lattice energy transfer, driving structural alterations without necessarily generating significant vacancy concentrations. It is possible for Mg and B atoms to be displaced or replaced by Nb ions in MgB_2 films that have been bombarded with Nb without suffering from a considerable rise in the vacancy density. Thanks to the simulation, the time and finance for experiments may be saved. Finally, the irradiated films are listed in Table 4.1

Table 4.1. *Name of films and the doses for Nb-ion irradiations*

No	Name of films	Dose (ions/cm^2)
1	Pristine	0
2	Nb-3E13	3×10^{13}
3	Nb-5E13	5×10^{13}
4	Nb-7E13	7×10^{13}
5	Nb-9E13	9×10^{13}

4.2 Variations of the crystal structure in MgB_2 films before and after irradiation by Nb ions

4.2.1 Phase formation, crystallinity of pristine and Nb-ion irradiated MgB_2 films

X-ray diffraction (XRD) examinations were conducted to investigate the alterations in the crystallinity of MgB_2 films. Figure 4.2(a) displays the comparable diffraction patterns before and after irradiating on samples. The pristine MgB_2 film exhibits excellent crystalline quality and phase purity, with distinct diffraction peaks corresponding to the (*0001*) and (*0002*) orientations of MgB_2 phase, beside a pronounced Al_2O_3 substrate peak.

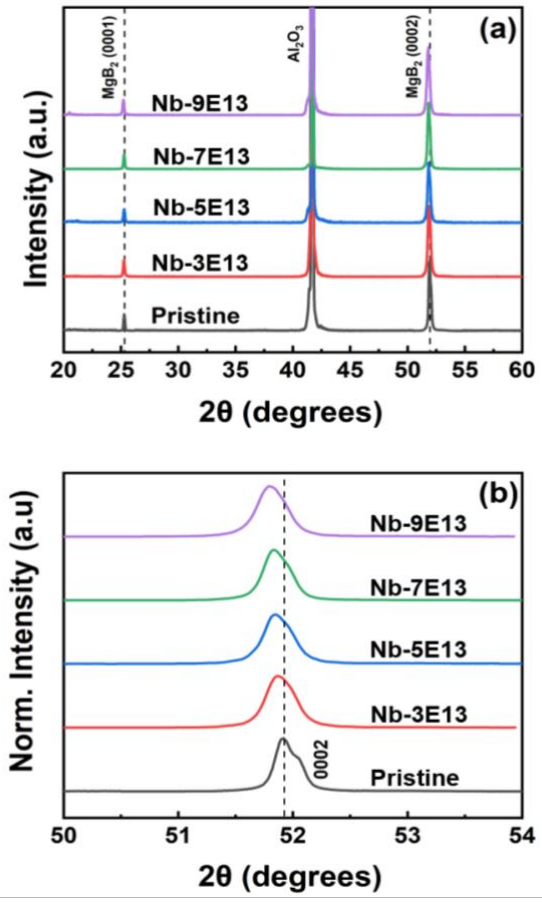


Figure 4.2. *XRD diagram of the pristine and Nb-ion irradiated MgB_2 films.*

((a) Pure c-axis oriented MgB_2 films before and after Nb-irradiation. (b) Structural shift of MgB_2 peaks to lower 2θ angles.)

All diffraction peaks remain detectable after Nb-ion irradiations, confirming that the general crystal structure of MgB_2 is maintained even at the highest dose of Nb-ion. Nonetheless, a steady change in peak intensity is seen with increasing Nb-ion dose. The pronounced widening and decreased intensity of the (*0002*) MgB_2 peaks relative to the pristine MgB_2 films signify irradiation-induced lattice deformation and defect generation. Figure 4.2(b) presents an enlarged depiction of the (*0002*) MgB_2 peak to illustrate structural alterations. The (*0002*) MgB_2 peak is seen to trend towards lower values of 2θ as Nb-ion dose increases. The value of full width at half maximum (FWHM) of the (*0002*) MgB_2 peak, indicative of the crystal quality of the MgB_2 films, increases with Nb-ion dose. The FWHM increases from 0.257° to 0.32°, indicating a progressive decline in crystallinity. The peak widening is attributed to lattice disorder generated by Nb-ion irradiations.

All MgB_2 diffraction peaks consistently change to lower values of 2θ after Nb-ion irradiation, indicating an expansion of the lattice along the *c*-axis direction. The findings indicate that the Nb ion dose significantly modifies the lattice structure and induces strain without leading to total amorphization or phase breakup. These phenomena pertain to irradiation-induced lattice disorder and atomic displacements, resulting in minor *c*-axis expansion and diminished crystallinity. The Raman data corroborate this explanation indicating heightened disorder with Nb-ion dose. XRD analysis confirms that Nb-ion dose induces regulated lattice disruption and defect formations in MgB_2 thin films, significantly influencing its superconducting capabilities while preserving its crystal structure.

Due to an intensity approximately six times greater than the *(0001)* MgB_2 peak, the *(0002)* reflection was prioritized for lattice parameter evaluation. The lattice constants of MgB_2 were determined for a hexagonal structure by Bragg's law and Miller's indices:

$$\frac{1}{d_{hkl}^2} = \frac{4}{3}\left(\frac{h^2+h.k+k^2}{a^2}\right) + \frac{l^2}{c^2} \tag{4.1}$$

Since MgB_2 exhibits a hexagonal crystal framework, the (0002) reflection corresponds to the Miller indices (h k -(h+k) l), where (h=0, k=0), and (l=2). Table 4.2 presents the calculated *c*-axis parameters obtained from the *(0002)* peaks.

Table 4.2. The results of calculated the c-axis parameters

No	Films	*c*-axis parameter (Å)
1	Pristine	3.5210
2	Nb-3E13	3.5213
3	Nb-5E13	3.5228
4	Nb-7E13	3.5277
5	Nb-9E13	3.5245

A little alteration in the *c*-axis lattice parameter is seen with increased Nb ion dose. In comparison to the pristine film (3.5210 Å), the *c*-axis exhibits overall rises, attaining a peak value of 3.5277 Å at Nb-7E13 film, thereafter experiencing a little decrease at the maximum dose (3.5245 Å) [46]. The minor fluctuations indicate that the (*0002*) peak's movement towards lower values of 2θ signifies a quantifiable expansion in interplanar spacing along the *c*-axis. This phenomenon is due to lattice deformation and atomic displacements generated by irradiation. As Nb ion irradiation occurs approximately parallel to the c-axis, collisions between the incident ions and Mg and B atoms may induce local displacements and structural diminishment, leading to minor lattice expansion. At high irradiation doses, conflicting phenomena such as defect formation and localized structural relaxation may influence the observed non-monotonic behavior. Comparable alterations in lattice properties have been shown in prior investigations of ion-irradiated MgB_2 materials [56,101].

The tensile strain (ε) caused in MgB_2 films is another characteristic derived from the alteration of MgB_2 diffraction peaks. The values of ε determined by the

Williamson-Hall model (Table 4.3). A consistent increase in ε is found with escalating Nb-ion irradiation, indicating irradiation-induced tensile deformation in the MgB_2 sheets. Ion irradiation is recognized for inducing disorder in the crystal lattice of MgB_2, leading to minor misorientation of crystallites and an increase in the density of point defects. These flaws induce lattice distortion and account for the observed increase in tensile strain ε and the concurrent deterioration of the crystallinity of MgB_2 films.

In addition, the Williamson - Hall technique is used to determine the average crystallite size (τ) and ε by using the X-ray diffraction (XRD) statistics. This study is based on the FWHM of the (*0001*) and (*0002*) reflections of MgB_2, which are used in the process of generating the Williamson - Hall plot for the MgB_2 phase [109].

$$\beta \cos\theta = 4.\varepsilon.\sin\theta + \frac{K\lambda}{\tau} \tag{4.2}$$

In the equation, β represents the value FWHM of the diffraction peak, θ stands for the Bragg angle, K (= 0.9) is the crystallite form factor, and λ is the wavelength of the Cu-K_α radiation. The values of τ fall progressively from 28.65 nm for the pure sample to 26.05 nm for the sample with the maximum irradiation doses, as shown in Table 4.3. On the other hand, the value of ε rises from 0.045% to 0.758%. Irradiation-induced tensile deformation in the MgB_2 films is shown by the observation of a consistent increase in ε as the amount of Nb-ion irradiation increases throughout the experiment. It is well known that ion irradiation causes disorder to be introduced into the crystal lattice of MgB_2, which leads to a modest change in the orientation of crystallites and an increase in the density of point-like defects. These defects are responsible for the rise in the value of ε and the concomitant loss of the crystallinity of MgB_2 films. They are also responsible for the lattice distortion that is seen.

Table 4.3. *The results of calculating the tensile strain (ε)*

No	Films	ε (%)
1	Pristine	0.191
2	Nb-3E13	0.388
3	Nb-5E13	0.538
4	Nb-7E13	0.633
5	Nb-9E13	1.084

4.2.2 Surface morphology of pristine and Nb-ion irradiated MgB_2 films

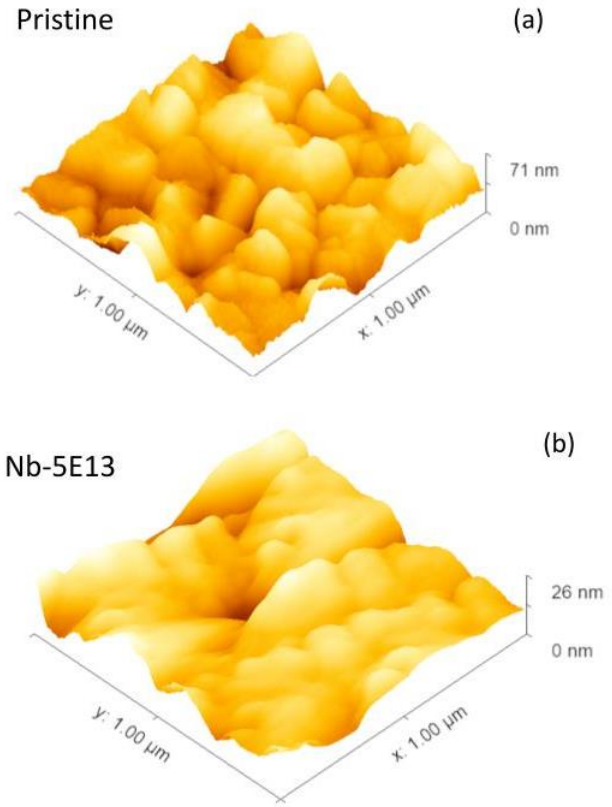


Figure 4.3. *AFM images: (a) pristine and (b) Nb-5E13 films*

Atomic force microscopy (AFM) is used to investigate the influence of Nb-ion irradiation on the surface morphology of MgB_2 films, as seen in Figure 4.3. In Figure 4.3(a), the pristine film has a distinct grain characteristics, indicating homogenous growth and high crystalline quality. Following Nb-ion irradiation at a dose of 5×10^{13} ions/cm² (Figure 4.3(b)), noticeable alterations in the surface morphology are seen. The irradiation film exhibits a minor alteration in surface roughness and a modification of the grain structure, characterized by the degradation grain boundaries. These variations may be attributed to ion-induced atomic displacements and lattice distortion, resulting in surface restructuring without total amorphization.

The observed morphological change reveals the development of lattice distortions and defects on the film's surface. These characteristics align with defect production generated by irradiation and may serve as supplementary pinning points for vortices. The findings align well with the flux pinning analysis presented in section 4.4.3, whereby the Dew - Hughes model suggests a partial shift from normal surface pinning in the pristine film to normal point pinning after Nb-ion irradiation.

4.2.3 Crystal structure variations of pristine and Nb-ion irradiated MgB_2 films

Figure 4.4 illustrates the room-temperature Raman spectra of all MgB_2 films, including both pristine and Nb-ion irradiated MgB_2 film. Raman spectroscopy is used to examine the development of diseases and structural defects in MgB_2 films induced by Nb-ion irradiation. Four optical phonon modes, E_{2g}, E_{1u}, B_{1g} and A_{2u} have been identified in MgB_2 films. Of them, only the E_{2g} mode is Raman-active and significantly influences superconductivity because of its robust interaction with charge carriers. A large and powerful Raman signal centered at 600.87 cm^{-1} is seen in the pristine MgB_2 film. This peak pertains to the E_{2g} phonon mode (denoted as ω_2), which is associated with the in-plane vibrations of boron (B) atoms. The E_{2g} mode's location and its value of FWHM are influenced by strain, lattice disorder, and defects. Consequently, these factors indicate the robustness and structural integrity of EPC [53,59]

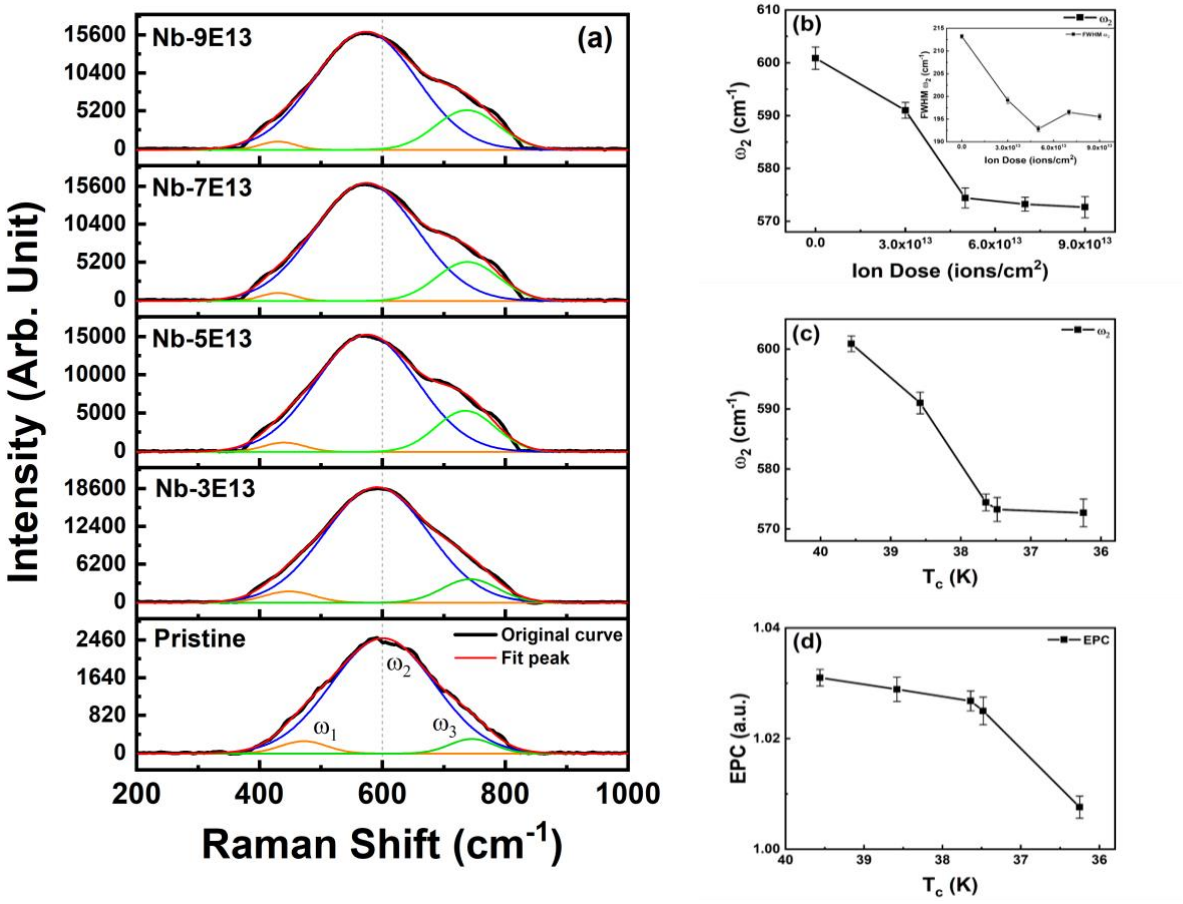


Figure 4.4. *Raman spectroscopy and parameter analysis of pristine and Nb-irradiated MgB_2 films*

(a) *Raman spectra of pristine and Nb-ion irradiated films with Gaussian fitting for E2g (ω2) and PDOS modes.* ***(b)*** *Raman shift as a function of Nb-ion dose. Correlation of Tc with* ***(c)*** *Raman shift and* ***(d)*** *electron-phonon coupling (EPC).*

In the pristine film, the E_{2g} peak is positioned at 600.87 cm^{-1} with a substantial value FWHM of 213.22 cm^{-1}, indicating pronounced electron-phonon coupling in MgB_2 . All experimental data are fitted using Gaussian peak functions to study the development of the Raman spectra. In addition to the dominant E_{2g} peak (ω_2), two weak peaks located at approximately 471.91 cm^{-1} (ω_1) and 745.47 cm^{-1} (ω_3) are

involved to develop fitting accuracy. These feeble behaviors are mostly associated with vibrational modes, lattice deformation, and disorder. The retrieved E_{2g} peak locations and value FWHM values are used to assess the relative variations in EPC strength, as shown in Table 4.4. The Nb-ion dose significantly alters the Raman spectra of irradiated MgB_2 thin films. As the Nb-ion dose increases, the E_{2g} phonon mode consistently transitions to lower wavenumbers, indicating phonon softening. At the maximum ion dose of 9×10^{13} ions/cm², the E_{2g} peak location and FWHM attain their minimum values of 572.68 cm^{-1} and 195.54 cm^{-1}, respectively [110]. Despite ion irradiation causing lattice disorder and defects, the observed shortening of the E_{2g} linewidth indicates a decrease in strength of EPC, which prevails over the widening effects generated by disorder. Competing effects between disorder and EPC have been previously shown in irradiated and chemically replaced MgB_2 systems.

The influence of ω_1 on Raman spectra has been previously documented as minimal, so its impact is not elaborated upon here. Conversely, the ω_3 peak becomes more apparent with increasing Nb-ion doses. This characteristic pertains to phonon density of states (PDOS) contributions resulting from the relaxation of Raman momentum selection criteria in disordered systems. The amplification of the ω_3 peak signifies heightened lattice disorder and strain caused by ion irradiation, facilitating the emergence of PDOS-related characteristics in the Raman spectra.

The reduction in T_c of MgB_2 films has a clear correlation with EPC and phonon frequency. The relationship among these factors may be articulated by the McMillan formula [71,93]:

$$T_c = \frac{\langle\omega\rangle}{1.2} \exp\left(-\frac{1.04(1+\lambda)}{\lambda-\mu^*(1+0.62\lambda)}\right) \tag{4.3}$$

where $\langle\omega\rangle$ represents the average phonon frequency, μ^* is the Coulomb pseudopotential (0.13) [76], λ defines the EPC constant. The average phonon frequency is computed using the relation $\langle\omega\rangle = (\omega_1 \times \omega_2^2 \times \omega_3)^{0.25}$ and listed in Table 4.4 [68]. Based on the obtained values of $\langle\omega\rangle$, the Debye temperature (Θ_D) is determined using the relation:

$$\Theta_D = \frac{\langle\omega\rangle}{1.2} \times 1.45 \quad (4.4)$$

All estimated values are shown in Table 4.4. The value of λ for pristine MgB_2 film is determined to be 1.0499. With Nb-ion irradiated MgB_2 film, the value of EPC consistently decreases to 1.0289 and 1.0076 as the ion dose increases from 3×10^{13} ions/cm² to 9×10^{13} ions/cm². The little decrease value of λ, coupled with the fall in T_c, indicates that electron-phonon coupling significantly influences the superconducting characteristics of MgB_2. The T_c is very sensitive to λ and the characteristic phonon frequency, wherein a reduction in λ results in an exponential fall of T_c [71]. The current work reveals a progressive reduction in λ from 1.0499 to 1.0076 as Nb-ion dose increases, which aligns with the observed fall in T_c from 39.56 K to 36.25 K. This reflection pertains to irradiation-induced lattice disorder, which alters phonon dynamics and diminishes the electron - phonon interaction. The link between λ and T_c indicates that the suppression of superconductivity is intimately associated with the decrease in the value of EPC. The BCS theory posits that superconductivity results via the creation of Cooper pairs facilitated by phonon-induced lattice distortions. Lattice vibrations significantly mitigate Coulomb repulsion, hence promoting an attractive contact between electrons. When the temperature decreases below T_c, individual electrons form pairs, leading to the superconducting state. The value of EPC may also differentiate contributions from the σ and π bands. Prior research indicates that the values of EPC for the σ and π bands are roughly 1.02 and 0.45, respectively [15,67]. The acquired EPC values indicate that the σ band is the principal contributor to superconductivity in both pristine and Nb-ion irradiated MgB_2 films, corroborating our earlier findings [101]. The observed decrease in the value of EPC is probably due to crystal structural flaws and lattice distortions caused by Nb-ion irradiation. The value of Θ_D decreased from 721.35 K for the pristine MgB_2 film to 686.28K for the Nb-ion irradiated MgB_2 films subjected to a dose of 9×10^{13} ions/cm², as shown in Table 4.4.

Table 4.4. *Values of Raman peak centers, FWHM of E_{2g} peak, electron-phonon coupling, and Θ_D of the pristine and Nb-ion irradiated MgB_2 films*

Films	ω_1 (cm^{-1})	ω_2 (E_{2g}) (cm^{-1})	ω_3 (cm^{-1})	*FWHM* E_{2g} (cm^{-1})	*EPC* (λ)	Θ_D (K)
Pristine	471.91	600.87	748.62	213.22	1.0499	721.35
Nb-3E13	448.59	591.01	742.84	199.16	1.0289	705.78
Nb-5E13	440.36	574.43	735.29	192.87	1.0268	690.83
Nb-7E13	430.50	573.25	738.63	196.50	1.0250	687.01
Nb-9E13	430.05	572.68	737.73	195.54	1.0076	686.28

4.4 Superconductivity of pristine and Nb-ion irradiated MgB_2 films

4.4.1 Critical temperature of pristine and Nb-ion irradiated MgB_2 films

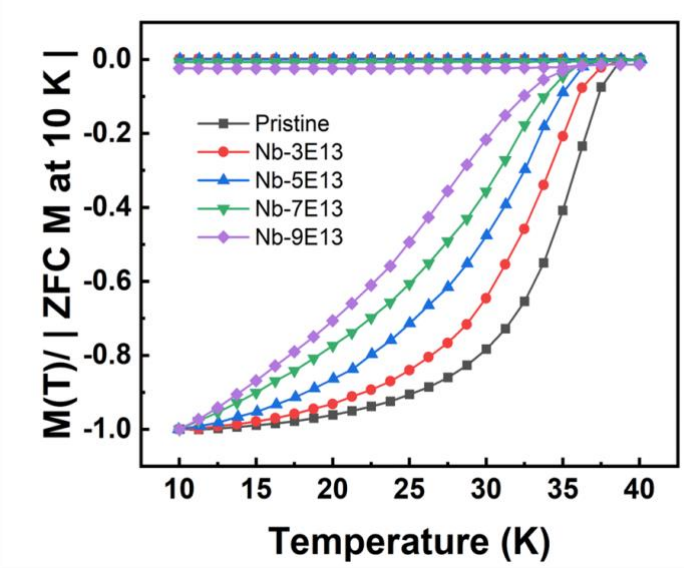


Figure 4.5. *Magnetization versus temperature (M-T) curves of the pristine and Nb-ion irradiated MgB_2 films.*

Zero-field cooled (ZFC) and field-cooled (FC) magnetization versus temperature (M-T) curves of the pristine and Nb-ion irradiated MgB_2 films. The

superconducting transitions are observed for all films, and T_c is defined as the temperature of the merging point in the M-T curves.

Figure 4.5. illustrates the temperature dependence of the field cooling (FC) and zero-field cooling (ZFC) magnetization curves for both pristine and Nb-ion irradiated MgB_2 films, assessed in a perpendicular magnetic field of 10 Oe. The transition to superconductivity is analyzed by varying the temperature from 50 K to 10 K. The applied magnetic field is less than the value B_{c1} of MgB_2 (2800 Oe), indicating that the measured magnetic response is not influenced by field-induced suppression of superconductivity.

A substantial difference is seen between the FC and ZFC curves for all samples. Under FC circumstances, partial magnetic flux penetration may arise via thin film geometry, surface imperfections, and irradiation-induced disorder, leading to vortex pinning during cooling and a diminished diamagnetic response. Conversely, in ZFC circumstances, the magnetic field is mostly ejected at low temperatures due to the Meissner effect, resulting in a pronounced diamagnetic signal. Both pristine and Nb-ion irradiated MgB_2 films bombarded with Nb ions exhibit distinct superconducting transitions in the ZFC mode, indicating that the films maintain relatively high crystallinity and strong homogeneity despite irradiation [63,86]. The acquired T_c values are shown in Table 4.5.

The pristine MgB_2 film exhibits the value of T_c of around 39.56 K, with a progressive decline in T_c seen as the Nb-ion irradiation dose increases, culminating in the lowest value at elevated ion doses. As temperature rises, a consistent widening of the superconducting transition is seen in the irradiated samples relative to the pristine film. This discovery indicates the increased disorder and defect density resulting from Nb ions irradiation, which diminishes intergranular connection and elevates the thermal activation of vortices. Comparable decreases in T_c have been previously seen in MgB_2 films subjected to ion irradiation, often ascribed to irradiation-induced structural deterioration and defect generation [102].

Table 4.5. *T_c of pristine and Nb-ion irradiated MgB_2 films*

Films	T_c (K)	T_c (Nb-ions) / T_c (pristine) (%)
Pristine	39.56	100
Nb-3E13	38.07	96.2
Nb-5E13	37.51	94.8
Nb-7E13	36.86	93.2
Nb-9E13	36.25	91.6

4.4.2. Critical current density of pristine and Nb-ion irradiated MgB_2 films

Figure 4.6 illustrates the magnetic field dependency of J_c for both pristine and Nb-ion irradiated films at temperatures ranging from 7 K to 30 K. In all samples, J_c attains its peak in the self-field area and decreases monotonically with the application of an increasing magnetic field, a behavior typical of type-II superconductors due to vortex motion. Irradiation induced defects mostly alter flux pinning, hence influencing the relative J_c performance of Nb-ion irradiated MgB_2 films, especially in the high-field region.

At low magnetic fields, the Nb-ion irradiated MgB_2 films exhibit reduced values of J_c compared to the pristine film. The reduction of J_c after irradiation may be attributed to the degradation of superconducting connection due to disorder. In the middle and high-field areas, the irradiation films exhibit a more gradual reduction in J_c, indicating improved flux pinning. A crossover phenomenon is noted in which the irradiated samples exhibited superior performance compared to the unirradiated film. This crossover is contingent upon irradiation dose and temperature.

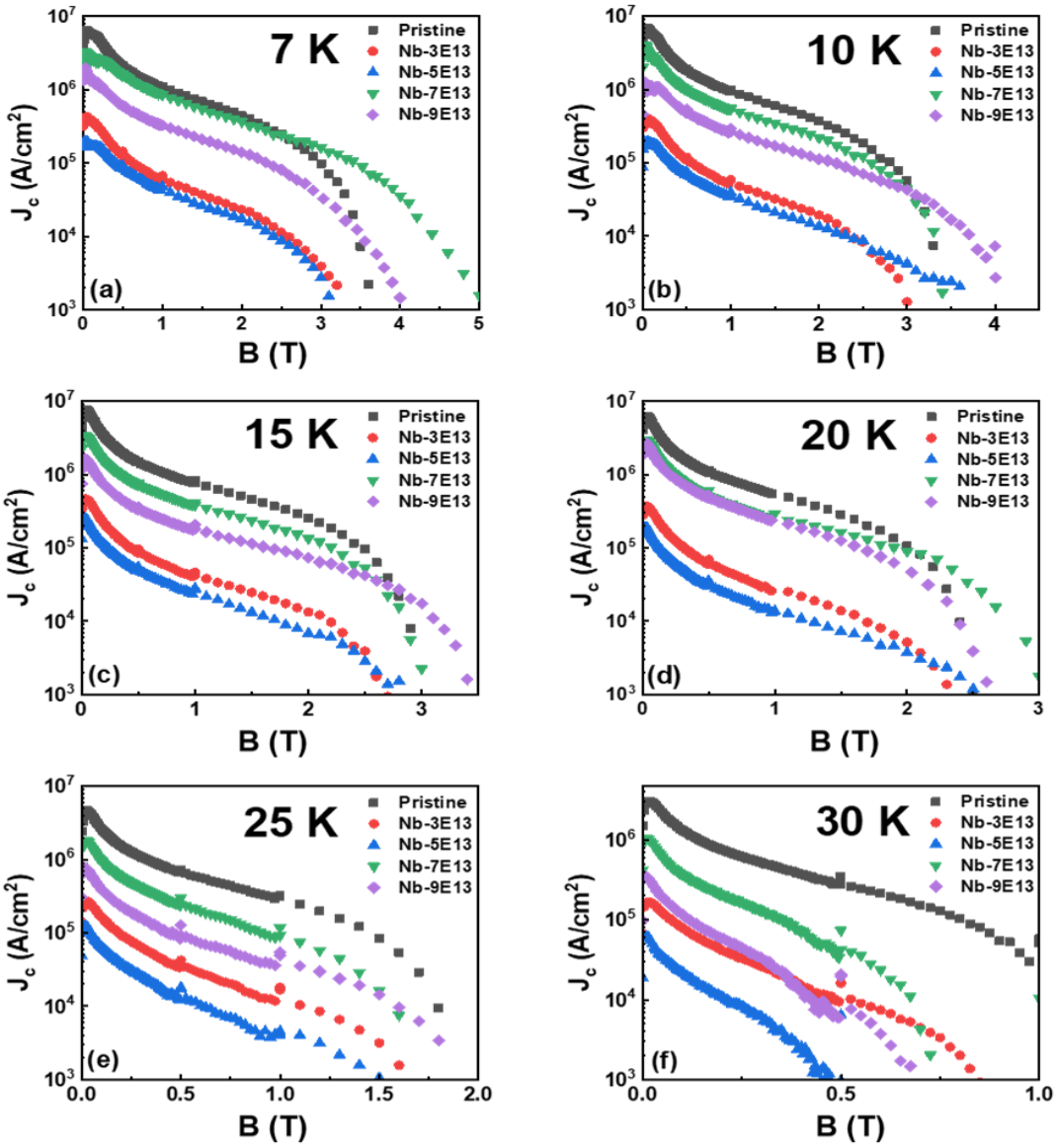


Figure 4.6. *J_c versus magnetic field of pristine and Nb-ion irradiated MgB_2 films measured at (a) 7 K, (b) 10 K, (c) 15 K, (d) 20 K, (e) 25 K and (f) 30 K.*

The magnetic field at which the J_c of Nb-ion irradiated MgB_2 films surpassed that of the pristine film is roughly 2 - 2.5 T for the 3×10^{13} ions/cm² film and around 3T for the 5×10^{13} ions/cm² films. At the temperature of 7 K, 10 K, and 15 K, the Nb - ion irradiated MgB_2 films with the dose of 3×10^{13} and 5×10^{13} ions/cm² demonstrate the most significant enhancement in the high-field area. The enhanced value of J_c in the irradiation samples are still visible, but when T = 20 K to 30 K, thermal activation causes the magnitude of J_c to decrease and the crossover to move

toward lower magnetic fields. The findings indicate that the enhancement of J_c is significantly influenced by both defect density and the ion penetration depth inside the film. In contrast to other irradiation investigations using O [82] , Fe [107], and Sn [63] ions, Nb ion irradiation in this study results in a significant augmentation of J_c, particularly in high magnetic fields. This discovery may be ascribed to the characteristics of the pinning centers generated by irradiation [29]. In the low-field region, vortex pinning is primarily influenced by normal surface pinning centers (2D), including grain boundaries. In contrast, in the high-field region, normal point pinning centers (0D), characterized by ion traces and dislocations, prevail. The ion irradiation in MgB_2 films generates point-like defects that contribute to the observed increase in J_c at high magnetic fields. As seen in Figure 4.1, Nb ions with an energy of 1 MeV do not completely pass the whole film thickness, leading to a heterogeneous distribution of irradiation-induced defects and a comparatively elevated concentration of vacancies in the irradiated area. The density of point-like pinning defects created by Nb ion irradiation is inferior to that produced by Fe-ion or Sn-ion irradiation, resulting in a more restricted magnetic-field range for sustained enhancement. The collective pinning model accurately delineates the field dependencies of J_c in superconducting films.

Figure 4.7 presents the double-logarithmic plots of J_c as a function of the magnetic field. Two distinct performances for the J_c behaviors are seen. In the low-field region, the vortex density is smaller than the effective density of pinning centers, leading to individual pinning of vortices and a virtually field-independent J_c. This area is designated as the singular vortex pinning region. In the intermediate field area, the density of penetrating vortices becomes higher, and vortex-vortex interactions gain significance, leading to a power law decay of $J_c \approx H^{-\beta}$, where the exponent β indicates the pinning strength [42]. The derived values of β are shown in Table 4.6.

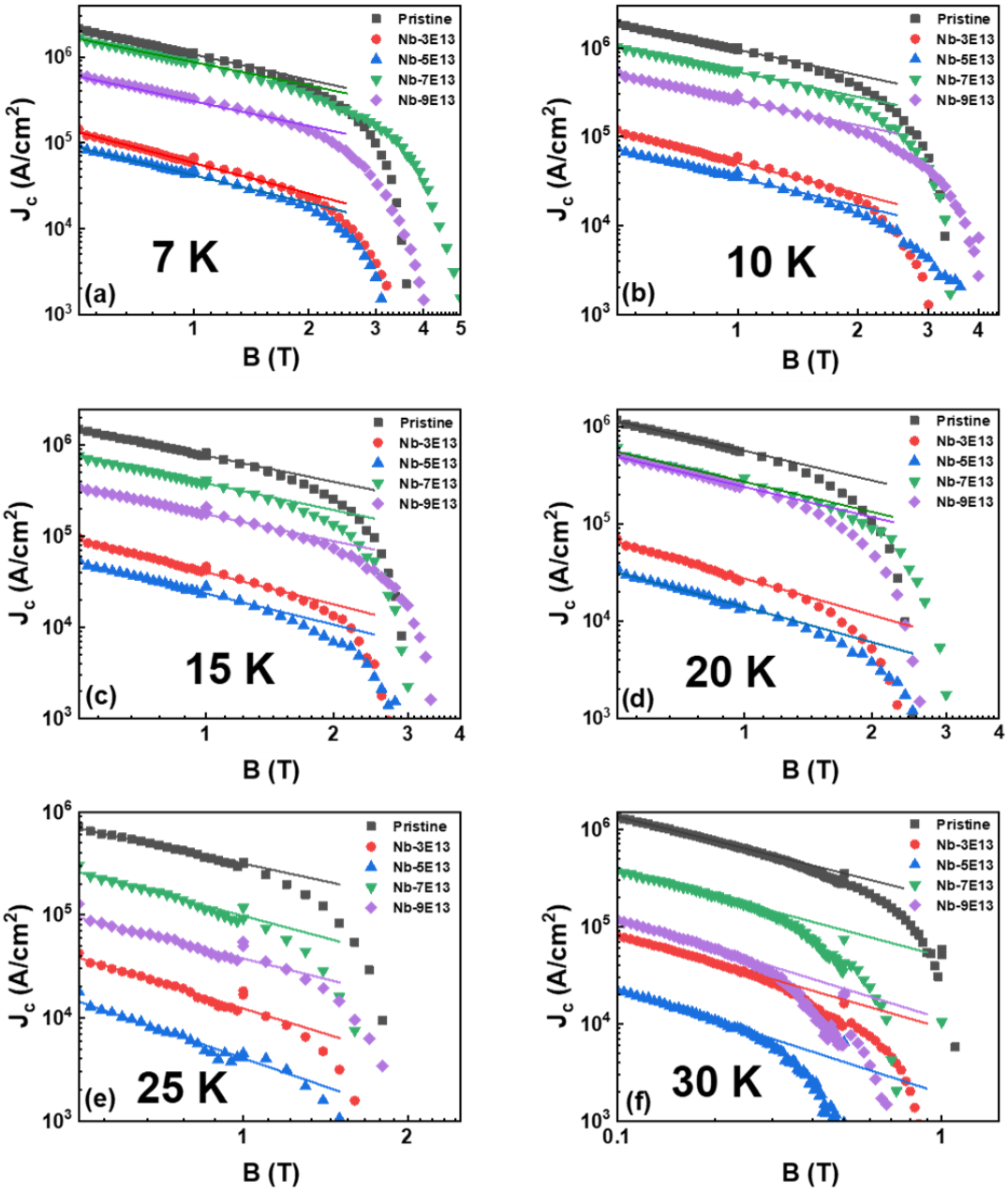


Figure 4.7. *Double logarithmic scaled field dependence of evolution of the J_c under applied magnetic field for Nb-ion irradiated MgB_2 films*

(at: (a) 7 K, (b) 10 K, (c) 15 K, (d) 20 K, (e) 25 K and (f) 30 K. Straight lines are overlaid to emphasize the systematic variation of the field response with irradiation dose and temperature)

Table 4.6. *The β values for pristine and Nb-ion irradiated MgB_2 films*

Films	β					
	7 K	**10 K**	**15 K**	**20 K**	**25 K**	**30 K**
Pristine	0.99	0.96	0.95	0.87	1.14	0.83
Nb-3E13	1.19	1.17	1.17	1.24	1.64	0.96
Nb-5E13	1.07	1.05	1.13	1.20	1.83	1.08
Nb-7E13	0.94	0.93	0.97	1.06	1.41	0.90
Nb-9E13	0.96	0.95	0.98	1.04	1.32	1.03

For all temperatures, the strength pinning seems to be weak pinning, with the the β values staying about 1 for all samples. Among these samples, the Nb-7E13 has the minimum β when compared to other irradiated samples. This result may indirectly prove the best enhancement of flux pinning in the dose of 7×10^{13} ions/cm^2, therefore improving the Jc in the fields.

4.4.3. Flux pinning mechanisms in pristine and Nb-ion irradiated MgB_2 films

The impact of Nb-ion irradiations on the pinning characteristics of MgB_2 films is examined by assessing the field dependency of the pinning force density (F_p) and the normalized pinning force density ($f_p = F_p/F_{p,max}$). The F_p is calculated using the equation $F_p = B \times J_c$. The normalized field is expressed as $b = B/B_{irr}$, where B_{irr} represents the irreversibility field (at J_c = 1000 A/cm²) [42]. The obtained values of B_{irr} are similar to those previously reported in HPCVD MgB_2 films [44].

Figure 4.8 illustrates the correlation between the normalized pinning force density F_p and the normalized field b for the examined MgB_2 films. To determine the dominant pinning mechanism, the data are investigated using the Dew-Hughes model [19]. Crucially, this approach facilitates identifying geometric pinning centers,

including surface or point defects, while shedding light on how irradiation modifies vortex pinning behavior within MgB_2 films:

$$f_p = Ab^p(1-b)^q \quad (4.5)$$

A: represents a field-independent constant; p and q: fitting parameters characterizing the pinning type.

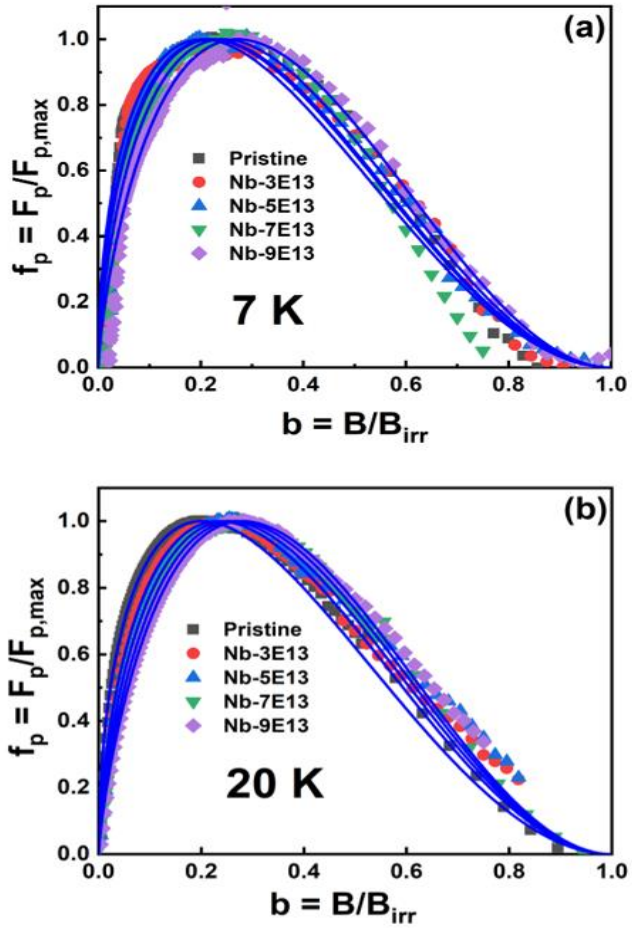


Figure 4.8. *Plot of normalized volume pinning force f_p, on normalized field b of the pristine and Nb-ion irradiated MgB_2 films*

(where $f_p = F_p/F_{p,max}$, $b = B/B_{irr}$, and measured at (a) 7 K and (b) 20 K)

This model well represents the experimental data, especially in the low field area. For each film, the parameters p and q, together with the accompanying $b_{peak} = p/(p+q)$, are determined at both temperatures. The q value is consistently

measured at 2 for all samples across both temperatures, indicating that point pinning is the predominant mechanism [44]. The p and b_{peak} values are analyzed to more accurately ascertain the nature of core pinning. In MgB_2, magnetic flux exists as vortices that must be impeded by defects to sustain a high J_c. In pristine films, pinning is primarily influenced by surface (2D) defects like grain boundaries, which are effective at low fields but diminish in efficiency as vortex density rises. Nb-ion irradiation induces localized lattice disorder, resulting in point-like (0D) defects that serve as effective pinning locations, especially under elevated magnetic fields. Consequently, the pinning process shifts to enhance point-pinning contributions, so elevating high-field J_c while marginally reducing T_c due to a disorder generated by irradiation. At T = 7 K, p ≈ 0.50 and b_{peak} = 0.2 for the pristine MgB_2 film, aligning with the predominant surface (2D) pinning [63]. This behavior is characteristic of *c*-axis oriented MgB_2 films, where grain boundaries aligned with the ab-plane serve as efficient surface pinning locations when a magnetic field is applied perpendicular to the film surface.

Surface pinning in the pristine MgB_2 films arise from broad defects, such as grain boundaries, which predominate at low magnetic fields. In contrast, Nb-ion irradiation induces localized point defects that progressively enhance vortex pinning at elevated magnetic fields. Notable alterations in the values of p and b_{peak} are seen in the Nb-ion irradiated MgB_2 films, particularly at high dose of 7×10^{13} and 9×10^{13} ions/cm^2. The results rise to p = 0.71, b_{peak} = 0.26 and p = 0.77, b_{peak} = 0.26, respectively. Despite these values being below the optimal thresholds for pure point pinning (p = 1, q = 2, and b_{peak} = 0.33), their persistent escalation signifies a distinct divergence from surface pinning behavior. This tendency is confirmed by numerous experimental research results. XRD study reveals lattice deformation and peak widening due to irradiation, while Raman spectroscopy indicates heightened disorder and contributions to the phonon density of states. The structural modifications align with the development of localized defect structures that may function as point-like pinning locations. Furthermore, the rise in J_c in the high-field area with escalating

irradiation dose provides further evidence that irradiation-induced defects improve vortex pinning. The pinning behavior transitions from predominant surface pinning in the pristine film to a state characterized by an increasing influence of point-like pinning centers after Nb-ion irradiation. The Dew-Hughes model indicates that the pinning landscape is influenced by surface defects and irradiation-induced point abnormalities, rather than by extensive defect structure. The findings indicate the simultaneous presence of surface and point pinning processes in the Nb-ion irradiated MgB_2 films.

4.5. Conclusions of chapter 4

Regarding the structural properties, Nb ion irradiation primarily causes lattice distortions and ion tracks rather than vacancy accumulation, while successfully maintaining the MgB_2 crystallinity up to a dose of 9×10^{13} ions/cm². XRD analysis reveals an expansion in the c-axis lattice constant (3.5210 Å to 3.5245 Å), evidenced by the expanding and slight shifting of the *(0002)* peak. Furthermore, Raman spectroscopy shows a consistent decline in both the E_{2g} phonon mode and its FWHM, directly indicating a weakened electron-phonon coupling (EPC) constant as the ion dose increases. These findings substantiate the formation of irradiation-induced point-like defects via ion tracking.

In terms of superconductivity, the induced lattice distortions lead to a slight reduction of the T_c from 39.56 K to 36.25 K and the EPC constant slightly declines from 1.0499 in the pristine sample to 1.0076 in Nb-9E13 sample. The decrease T_c appears in almost studies of MgB_2 in the world; when compare to other studies, these redutions were not significant. However, there were enhancements of the J_c under high fields by the partial shift of the pining mechanism from normal surface pinning to normal point pinning after irradiation. The investigation also found the best enhancement of J_c achieved in the Nb-7E13 sample.

Chapter 5. INVESTIGATION OF THE CRYSTAL STRUCTURE AND SUPERCONDUCTING PROPERTIES IN MAGNESIUM DIBORIDE USING IRRADIATION OF NICKEL IONS

After doing a number of experiments with both MgB_2 bulks and films in previous chapters, the advantages of MgB_2 in the real applications were recognized. For example, bulks were convenient and cheaper for practical applications to make the power-in-tube wire, which has been classified as the 1st generation (1G) of superconducting cable, however J_c in MgB_2 films are higher, and can be used for the 2nd generation (2G) superconducting cables or the high quality devices. As a result, more research into MgB_2 films by irradiation with additional ions is required. The motivation from chapter 4, this chapter presents research findings involving another ion: Ni - magnetic ion - which shows the greatest improvement of J_c in my dissertation. Furthermore, no comprehensive investigation on this scientific subject has been conducted in Vietnam. This inspired me to perform experiments to come into MgB_2 films irradiated by magnetic ions.

In fact, there are many attempts at improving flux-pinning properties in MgB_2 films by irradiating non-magnetic ions such as protons [12,81,89], neutrons [24,99,115], O [40,82,106], Sn [63], He [4], and C [45,46] have been mostly successful. J_c values are clearly obtained, and the dominance of point-like pinning has been proven. The research ideas are then driven to the use of magnetic ions. Fe-ion irradiations have been performed on MgB_2 films [102]. The local structures and optical properties of the samples are presented. Nonetheless, no research has largely concentrated on the flux-pinning characteristics of magnetic-ion irradiated MgB_2 films, hence presenting a substantial opportunity for investigation. My study examined the impact of Ni-ion irradiation on the crystal structure and flux-pinning characteristics of about 400 nm-thick MgB_2 films. Furthermore, my research indicates that the irradiation of MgB_2 films using Ni ions provides a unique chance

to examine the impact of defects and lattice distortions on the structural and superconducting characteristics of the material.

As mentioned in chapter 2, using the hybrid physicochemical vapor deposition (HPCVD) approach, I have successfully produced MgB_2 films with a thickness of ~ 400 nm on Al_2O_3 substrates. At VNU University of Science, the HUS-5SDH-2 tandem Pelletron accelerator was used in order to carry out the process of Ni-ion irradiations. The energy of the Ni-ion beam was held constant at 1 MeV, and the ion doses that were 3×10^{13}, 5×10^{13}, 7×10^{13}, and 9×10^{13} ions/cm^2. The samples of MgB_2 films that corresponded to the pristine condition were designated as Ni-3E13, Ni-5E13, Ni-7E13, and Ni-9E13, respectively (Table 5.1).

Table 5.1. *Name of films and the doses for Ni-ion irradiations*

No	**Films**	**Dose (ions/cm^2)**
1	Pristine	0
2	Ni-3E13	3×10^{13}
3	Ni-5E13	5×10^{13}
4	Ni-7E13	7×10^{13}
5	Ni-9E13	9×10^{13}

Within the MgB_2 films, the use of 1 MeV Ni-ion energy allowed for the production of defects that were both deep and rather uniform. These flaws served to promote point-like defects that enhanced flux pinning while simultaneously preventing excessive lattice damage that may potentially weaken superconductivity. The Monte Carlo simulation tool known as SRIM (Stopping and Range of Ions in Matter) was used in order to estimate the mean projected range (R_p) of the Ni ions [116,117]. R_p is defined as the average distance that an ion travels along the original

beam direction before falling to rest in the target. Through the process of irradiation, the Ni-ion beam was positioned such that it was perpendicular to the surface of the film and aligned with the crystallographic c-axis. The lists of samples are used in these studies in Table 5.1.

After created samples, I conducted investigations of the impact that Ni-ion irradiation had on the structural and flux-pinning characteristics of MgB_2 films, with a particular emphasis on the role that Raman spectroscopy played in the process. In order to characterize the crystallinity and electron-phonon coupling (EPC), X-ray diffraction (XRD) and Raman spectroscopies were used. Additionally, magnetization measurements were utilized in order to get insights into the superconducting characteristics. The detailed conditions for the sample measurements are as follows:

(a) The magnetic field that was applied during the measurements of magnetization was directed in a direction that was perpendicular to the surface of the film in order to guarantee that it was aligned with the c-axis.

(b) The crystallinity of the MgB_2 films was determined by the use of X-ray diffraction (XRD), and Raman spectroscopy was carried out at room temperature with the assistance of a MAPLE II spectrometer equipped with a green laser operating at 532 nm.

(c) Magnetization versus temperature (M-T) measurements were used to deduce the value T_c.

(d) At 5 K and 20 K, the values of J_c were obtained by using the magnetization versus field curves. This was accomplished by employing Bean's model, which states that $J_c = 30.\Delta M/r$, where r represents the sample radius and ΔM represents the magnetization difference at each applied field. Every single measurement of M-T and M-H was carried out with the assistance of a PPMS (Quantum Design, EverCool, Model 6000), with the field being applied in a direction that was perpendicular to the surface of the film.

X-ray diffraction investigation has shown a little increase in the c-axis lattice constant due to the irradiation-induced defects from 3.5210 Å (pristine) to 3.550 Å

(Ni-9E13). This rise may be caused by lattice expansion. The value of FWHM of the (0002) peak increased from 0.257° to 0.479°, which indicates a reduction in crystallinity and the development of lattice disorder as a function of time. The T_c is shown to decrease with increasing Ni-ion dose in accordance with the increasing defect density and lattice disorder. The value of EPC constant was dropping from 1.0499 (pristine) to 0.9599 (Ni-9E13). This is indicative of fading of superconductivity. The findings of Raman spectroscopy indicated that the lattice distortion was increased, which was confirmed by the shift of the E_{2g} peak from 598 cm^{-1} to 560 cm^{-1} and the reduction of FWHM from 213 cm^{-1} to 198 cm^{-1}. The $J_c$was shown to be improved in high-field region for Ni-ion irradiated MgB_2 films, especially for the doses of 3×10^{13} to 7×10^{13} ions/cm^2. This was ascribed to the formation of point-like pinning centers responsible for the augmentation of flux pinning. Using AFM images, it was found that the definition of the grain boundary had been substantially weakened. This was associated with the observed increase in the surface roughness, and also indicated the formation of localized disordered regions beneficial for vortex pinning. In summary, irradiation of MgB_2 films with Ni-ions leads to a trade-off between the degradation of the T_c and the enhancement of flux pinning, providing the potential for improved performance in high-field applications.

5.1. Simulation of the Ni-irradiation processes

In a completely similar manner to Chapter 4, before irradiating with Ni ions, the simulations of the irradiation process was performed. The simulation of the irradiation process of Ni-ions on MgB_2 films deposited on the c-cut Al_2O_3 substrates was carried out by licensed SRIM program [116,117]. Using the input data of an energy of 1 MeV Ni, a density of MgB_2 of 2.57 g/cm^3, the mean projected range (R_p) was well above 900 nm as shown in Figure 5.1.

In comparison with the thickness of MgB_2 film of ~ 400 nm in this work, it would be highly expected that most of the Ni ions thoroughly passed the MgB_2 film and stopped at the substrate (see figure 5.1(a)). Almost all of the Ni ions seem to stay

on the substrate at the depth of nearly 900 nm. Due to the presence of such strain and distortions may be introduced into the crystal lattice, which might potentially have effects on the superconducting properties. The results might reveal that the ion track during the Ni ion irradiation process effectively generates point defects and lattice distortion [63].

Figure 5.1(b) illustrates that the number of vacancies in irradiated films seems relative uniform, they gather more in the depth of substrace (around 800-900nm), so in the films, the distribution of vacancies seems to be relatively even, and therefore, it will witness the different effects compared to Nb ion irradiation. The investigations of crystal structure in later sections may reveal the clear results.

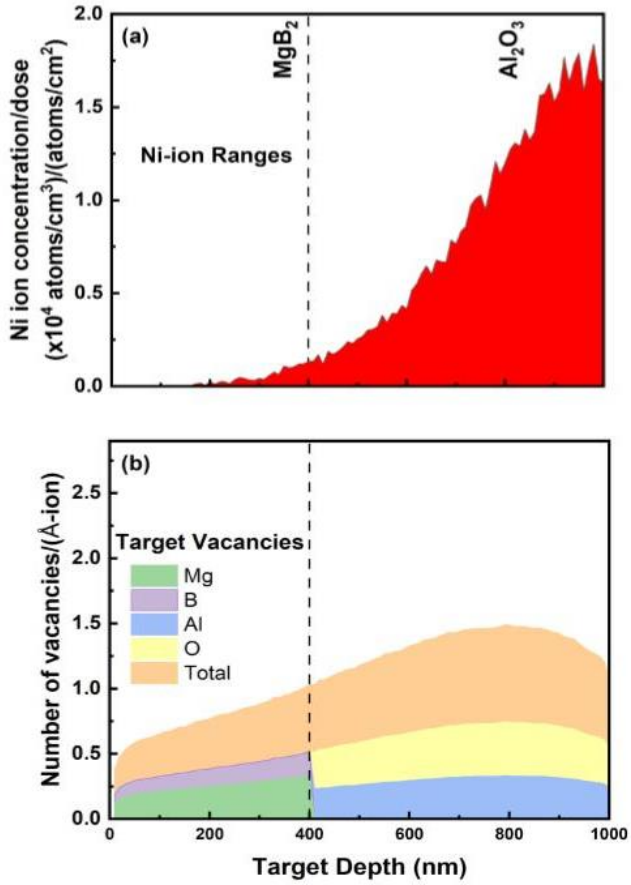


Figure 5.1. *(a) Mean projected range and (b) vacancy depth profile for 1 MeV Ni-ion irradiated MgB_2 film on c-cut Al_2O_3 substrate.*

5.2. Variations of the crystal structure in MgB_2 films before and after irradiation by Ni ions

5.2.1 Phase formation, crystallinity of pristine and Ni-ion irradiated MgB_2 films

To study the structure of samples, the XRD was investigated. The XRD diagrams of the pristine and Ni-ion irradiated MgB_2 films using different ion doses are revealed in Figure 5.2(a).

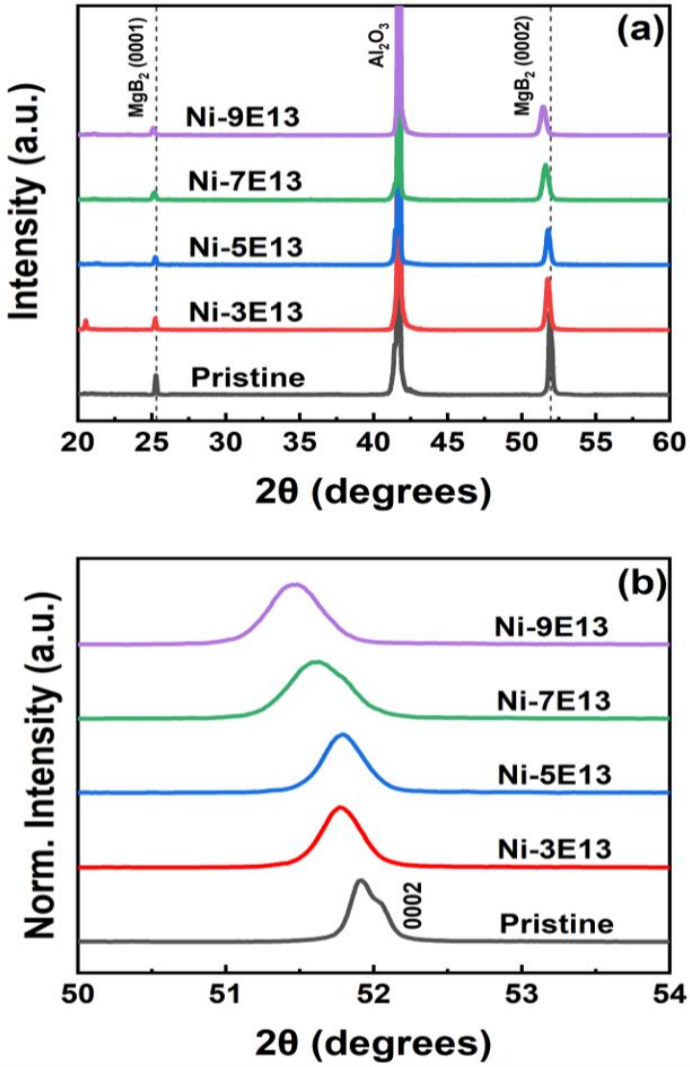


Figure 5.2. *XRD diagram of the pristine and Ni-ion irradiated MgB_2 films.*

((a) Pure c-axis oriented MgB_2 films before and after Ni-irradiation.

(b) Structural shift of MgB_2 peaks to lower 2θ angles.)

It would be clearly seen that all MgB_2 films were highly *c*-axis oriented with only two sharp dominant peaks (*0001*) and (*0002*). The impurity peaks were obviously absent. This image demonstrates that the MgB_2 films were fabricated with high quality, thanks to the good conditions.

The possible variation in the films' crystallinity was examined by comparing the value of FWHM of the MgB_2 films before and after Ni-ion irradiations as presented in Figure 5.2(b). The value of FWHM of the (*0002*) peak was observed to be 0.257° for the pristine MgB_2 film. For the Ni-ion irradiated MgB_2 films, that value of the (*0002*) peaks were increased to 0.479°. The results might suggest the degradation in crystallinity of MgB_2 films by Ni-ion irradiations.

Additionally, the slight shifts of the (*0001*) and (*0002*) peaks to lower values of 2θ were observed in all Ni-ion irradiated MgB_2 films, which might reflect the increase in the *c*-axis parameters. Among the two (*0001*) and (*0002*) peaks, the (*0002*) peak was chosen since its intensity was approximately 6 times larger than that of the (*0001*) peak. The value of *c*-axis parameter was calculated by using Bragg's law and Miller's indices:

$$\frac{1}{d_{hkl}^2} = \frac{4}{3}\left(\frac{h^2+h.k+k^2}{a^2}\right) + \frac{l^2}{c^2} \quad (5.1)$$

Because the crystal structure of MgB_2 is hexagonal, the (*0002*) peak would be presented as (*h k* - (*h* + *k*) *l*), where values of *h*, *k*, and *l* were 0, 0, and 2. The value of the *c*-axis parameter calculated from the (*0002*) peak was given in Table. 5.2. From Table 5.2, it would be clearly seen that the *c*-axis was slightly increased from 3.521 Å for the pristine MgB_2 film to 3.550 for the Ni-9E13 film. Geometrically, the irradiation process was carried out nearly along the c-axis of the MgB_2 films, and the collision of Ni ions with Mg or B in that direction possibly caused the extension of the c-axis, which was compared to be similar to other observations [54,101]. The defects and lattice disorders formed during the Ni ion irradiation process might affect the scattering between π and σ bands in MgB_2 and might produce the changes in superconductivity in MgB_2 films.

Table 5.2. *The results of calculating the c-axis parameters*

No	Films	*c*-axis parameter (Å)
1	Pristine	3.5210
2	Ni-3E13	3.5327
3	Ni-5E13	3.5305
4	Ni-7E13	3.5423
5	Ni-9E13	3.5500

5.2.2 Surface morphology of pristine and Ni-ion irradiated MgB_2 films

Atomic force microscopy (AFM) was utilized to investigate the morphological changes in MgB_2 films induced by irradiation, as illustrated in Figure. 5.3.

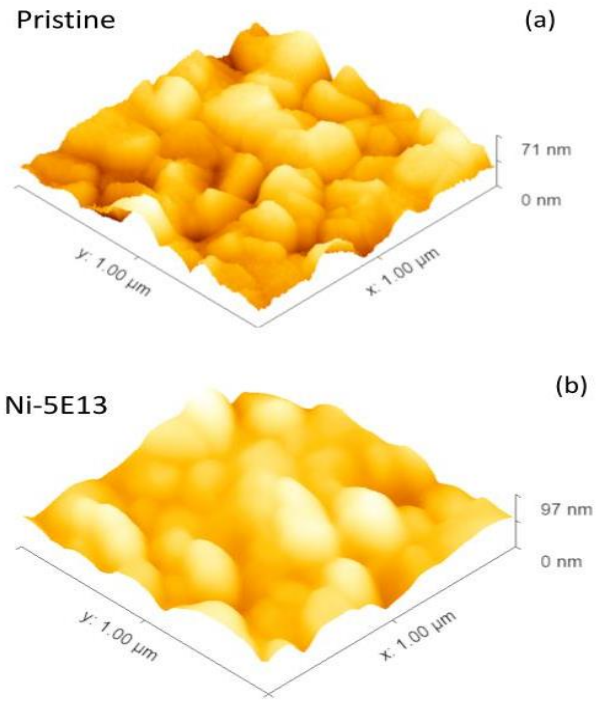


Figure 5.3. *AFM images: (a) pristine and (b) Ni-5E13 films*

Following Ni-ion irradiation at a dose of 5×10^{13} ions/cm^2, AFM images demonstrate a significant change in grain boundary definition. The observed reduction in grain boundary clarity indicates a partial amorphization of the surface, aligning with irradiation-induced defect accumulation documented in other single-crystalline systems [9]. The altered grain morphology suggests the development of localized disordered regions that may function as efficient flux pinning centers. Although AFM is sensitive to surface characteristics and cannot directly detect subsurface amorphization, the deterioration of grain boundary definition serves as compelling evidence for structural distortions by irradiation. The surface modifications are expected to enhance vortex pinning; however, further nanoscale characterization is necessary to elucidate their depth distribution and relationship to bulk properties in future studies.

5.2.3 Crystal structure variations of pristine and Ni-ion irradiated MgB_2 films

These studies performed the Raman spectroscopy at room temperature. Among the optical modes of MgB_2 consisting of E_{2g}, E_{1u}, B_{1g} and A_{2u} the E_{2g} phonon mode has been revealed to be the only initial-order active mode [9,115]. The E_{1u}, B_{1g} and A_{2u} modes would be dominant if the content of crystal defects or impurities was relatively high [73,106,114]. Hence, the Raman spectra have been shown to provide deep insight of the electron-phonon coupling, crystal defects, lattice disorder and impurities. Figure 5.4(a) shows the room temperature Raman spectra of pristine and Ni-ion irradiated MgB_2 films. The strong dependence of Raman spectra on the Ni ion dose was observed.

To quantitatively investigate dependence, the Gaussian fits were applied to experimental data. In overall, all experimental spectra have been shown to be well fitted with three peaks: ω_1, ω_2, and ω_3. Among the three main peaks, the $\omega_1$located at ~ 420 cm^{-1} was not going to be deeply discussed due to its small intensity and have relatively small influence on the overall Raman spectra. From the previous classification, the E_{2g} mode for the simple hexagonal structure of MgB_2 was characterized by the central peak ω_2, and the lattice distortion was identified by the

ω_1 and ω_3 peaks [9,37,70,78]. Two important things might be emphasized from the ω_2 peak for E_{2g} mode, which consisted of the peak position and the value of FWHM. The values of these parameters were listed in Table 5.3 and presented in Figure 5.4 (b-d). It would be clearly seen that both peak position and value of FWHM were changed with increasing the Ni ion doses.

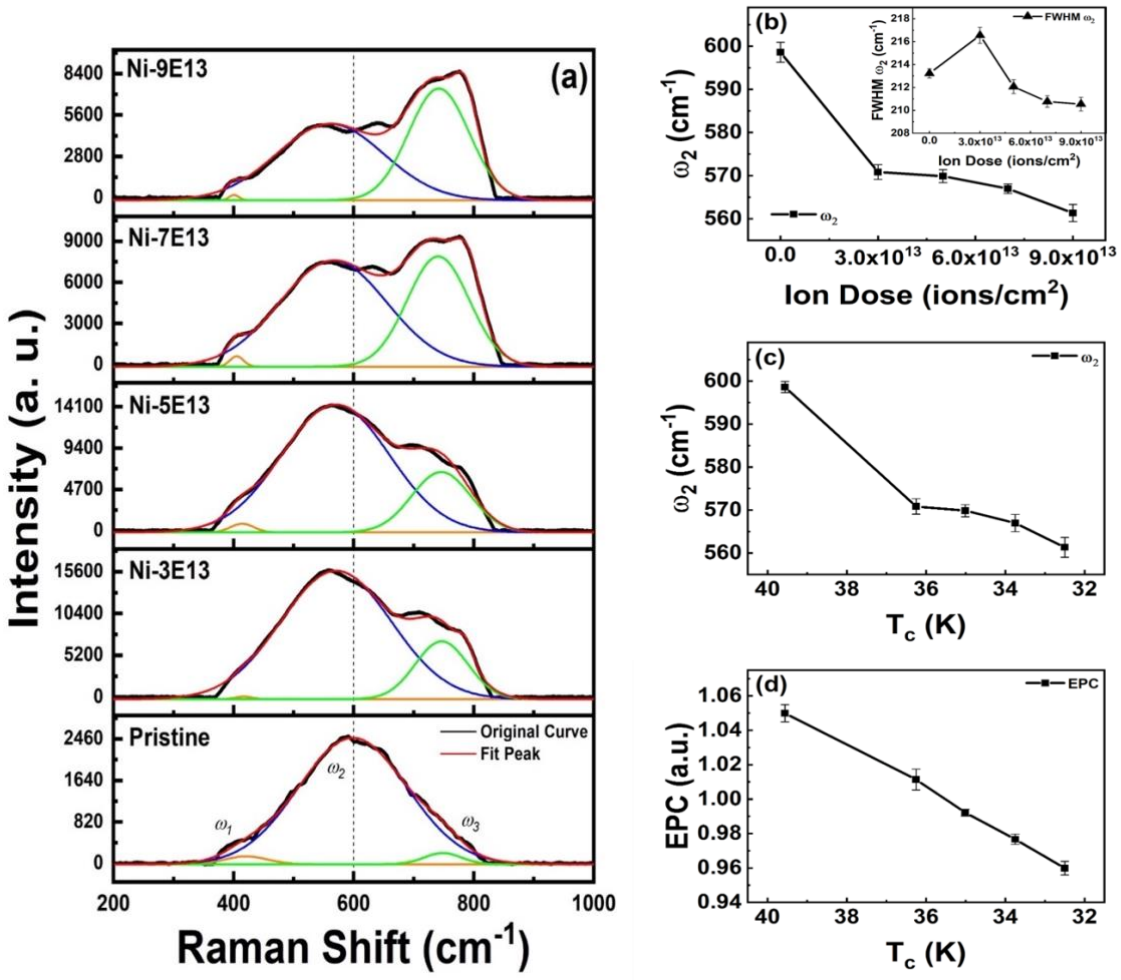


Figure 5.4. *Raman spectroscopy and parameter analysis of pristine and Ni-irradiated MgB_2 films*

(a) *Raman spectra of pristine and Nb-ion irradiated films with Gaussian fitting for E_{2g} (ω_2) and PDOS modes.* ***(b)*** *Raman shift as a function of Ni-ion dose. Correlation of Tc with* ***(c)*** *Raman shift and* ***(d)*** *electron-phonon coupling (EPC).*

The position of E_{2g} peak was observed at ~ 598 cm^{-1} for the pristine film, and it gradually shifted to the lower values as the increasing of Ni ion doses. The position was shifted to 560 cm^{-1} for the Ni-9E13 film. The value of FWHM of E_{2g} peak around 200 cm^{-1} might reflect the strong electron-phonon coupling in the MgB_2 films here and it was in agreement with other results [67,84,114]. More details, the value of FWHM of E_{2g} peak was decreased from ~ 213 cm^{-1} for the pristine MgB_2 film to ~ 210 cm^{-1} for the Ni-9E13 film. The slight decrease in the value of FWHM of E_{2g}peak might be partially attributed to the degradation in T_c as increasing the Ni ion dose.

While the E_{2g} peak was obviously found to get broaden, the additional peak well fitted by ω_3 became dominant. The growth of this peak was previously observed in MgB_2 samples with chemical substitution or irradiation [64,101,102,106]. In the strongly disordered systems or crystal defective systems, the momentum selection rule was likely to be violated leading to the development of phonon density of states (PDOS) [78,115]. In this work, the lattice distortion and strains in MgB_2 films were induced by Ni-ion irradiations. The increased dominance of ω_3 with increasing the Ni ion doses might imply the PDOS, which would also contribute to degrade superconductivity in MgB_2 films.

The relation between T_c, phonon frequency and electron-phonon coupling were expressed by using the McMillan formula with the revision of Allen-Dynes [71].

$$T_c = \frac{\langle\omega\rangle}{1.2} exp\left(-\frac{1.04(1+\lambda)}{\lambda-\mu^*(1+0.62\lambda)}\right) \quad (5.2)$$

where the average phonon frequency $\langle\omega\rangle$ was estimated as $\langle\omega\rangle = (\omega_1 \times \omega_2^2 \times \omega_3)^{0.25}$ [3,59], μ^* is the Coulomb pseudopotential, taken as equal to 0.13 [34], and λ was the electron-phonon coupling constant. Another parameter, the Debye temperature Θ_D was possibly deduced from the $\langle\omega\rangle$ by using the relation:

$$\Theta_D = \frac{\langle\omega\rangle}{1.2} \times 1.45 \quad (5.3)$$

The value of EPC of the pristine MgB_2 film was 1.0499, and it was monotonously decreased to 0.9599 as increasing the Ni ion dose. The electron-phonon interaction was explained by the Bardeen-Cooper-Schrieffer (BCS) theory.

The attraction between two electrons has been established by exchanging virtual phonons. The obtained reduction in EPC was then attributed to the decrease in T_c. Besides, MgB_2 has been reported to show two superconducting gaps consisting of σ-band and π-band. The electron-phonon coupling for each band was calculated to be 1.02 for σ-band and 0.45 for π-band [15,59,66]. The calculated values of the mentioned parameters were all listed in Table 5.3:

Table 5.3. *Values of Raman peak centers, FWHM of E_{2g} peak, electron-phonon coupling, and Θ_D of the pristine and Ni-ion irradiated MgB_2 films*

Films	ω_1 **(cm^{-1})**	ω_2 (E_{2g}) **(cm^{-1})**	ω_3 **(cm^{-1})**	**FWHM** E_{2g} **(cm^{-1})**	**EPC (λ)**	Θ_D **(K)**
Pristine	471.91	600.87	748.62	213.22	1.0499	721.35
Ni-3E13	417.21	570.83	746.79	216.55	1.0114	682.07
Ni-5E13	414.48	569.87	745.97	212.07	0.9922	680.19
Ni-7E13	405.23	566.98	741.02	210.76	0.9767	673.52
Ni-9E13	400.82	561.33	742.08	210.54	0.9599	668.57

The results presented in our work reflect that the superconductivity in pristine and Ni-ion irradiated MgB_2 films came from the σ-band. It might be concluded that the Ni-ion irradiation induced lattice distortion and defects, hence weakening the electron-phonon coupling and T_c. However, value of Θ_D was found to decrease from 721.35 K for the pristine MgB_2 film to 668.57 K for the Ni-9E19 film. These calculated values were compared to be in agreement with the range of 600 K - 750 K from other reports [96,102].

5.3 Superconductivity of pristine and Ni-ion irradiated MgB_2 films

5.3.1 Critical temperature of pristine and Ni-ion irradiated MgB_2 films

To examine the variation in superconductivity in the MgB_2 films with increasing the Ni ion doses, the zero - field cooling (ZFC) and field cooling (FC) magnetization versus temperature (M-T) curves of the samples were measured. The ZFC and FC curves were given in Figure 5.5.

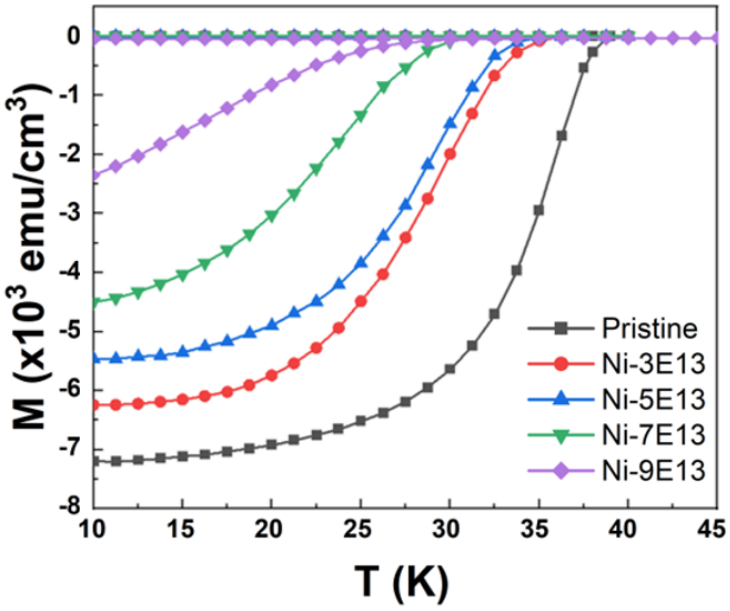


Figure 5.5. *Magnetization versus temperature (M-T) curves of the pristine and Ni-ion irradiated MgB_2 films,*

(the values of T_c were defined as the temperature of the merging point in the M-T curves)

Since the values of lower critical field (B_{c1}) of MgB_2 was reported to be ~ 2800 Oe, the field along the c-axis of the film in the experiment was set up to be 10 Oe. It has been well-known that the superconducting state was established as the temperature was below T_c. In the ZFC mode, the applied field of 10 Oe was totally excluded out of the MgB_2 films, which produced the dia-magnetization behaviors below T_c. In the FC mode, the applied field of 10 Oe was trapped in the form of vortices inside the MgB_2 films, which led to weaker magnetization than that of ZFC mode. When it comes to the stems, the possible reason for the decrease in T_c in

superconductors was widely attributed to the addition of impurities or formation of disorders and crystal defects [34,65,98]. Hence, it would be predicted that the disorders or defects formed by ion track as a result of Ni ion irradiation might be the main cause for the decrease in T_c in Ni-ion irradiated MgB_2 films. Value of T_c was determined as the temperature of the merger point in the normalized M-T curves [63,82,94] The obtained value of T_c versus Ni ion dose was given in Table 5.4.

Table 5.4. *T_c of pristine and Ni-ion irradiated MgB_2 films*

Films	**T_c (K)**	**T_c (Ni-ions) / T_c (pristine) (%)**
Pristine	39.56	100
Ni-3E13	36.25	91.6
Ni-5E13	35.01	88.5
Ni-7E13	33.75	85.3
Ni-9E13	32.50	82.2

It would be compared that value of T_c was decreased from 39.56K for the pristine MgB_2 film to 32.5 K for the Ni-9E13 film. When it comes to the values of T_c in bulks samples (in chapter 3), T_c in pristine MgB_2 films seem to be approximately theoretical value (39K) while in pure MgB_2 bulks this value is 38.09K. Certainly, it can be explained by the optimal fabricated processing as mentioned above.

Compared with recent global studies on magnetic ion irradiation, specifically regarding Fe-ion irradiation (see Table 5.5) [102], the results obtained from Table 5.4 and Table 5.5 demonstrate that our fabricated materials exhibit a superior enhancement in T_c. By elevating T_c to a higher temperature range, these materials offer significantly broader potential for practical applications.

Table 5.5. *T_c in the recent work using Fe magnetic-ions [102]*

Films	T_c (K)	T_c (Fe-ions) / T_c (pristine) (%)
Pristine	38.33	100
Fe-5E13	20.97	54.7
Fe-1E14	14.57	38.0
Fe-2E14	3.02	7.8

5.3.2 Critical current density of pristine and Ni-ion irradiated MgB_2 films

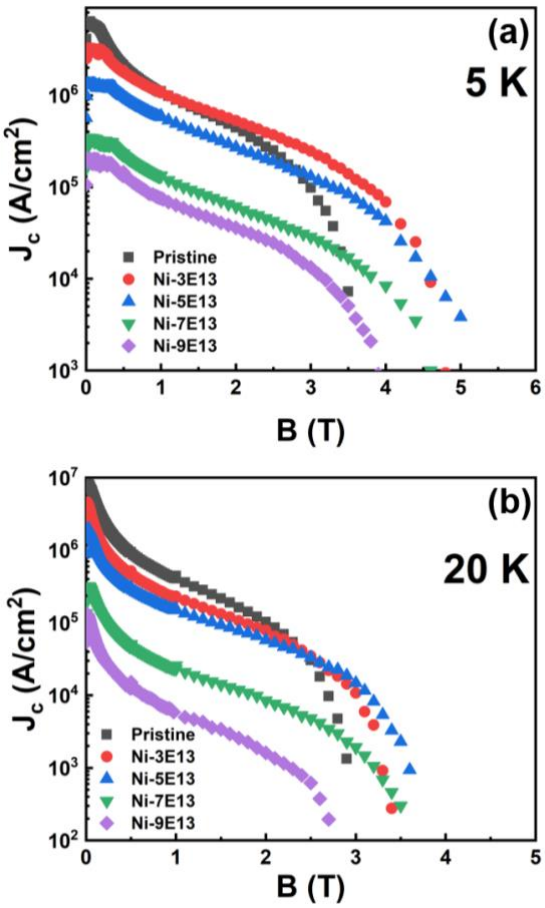


Figure 5.6. *J_c versus magnetic field of the pristine and Ni-ion irradiated MgB_2 films (a) 5 K, (b) 20 K*

Although the formation of defects and lattice disorders in Ni-ion irradiated MgB_2 films gave the suppression in T_c of the MgB_2 film, they were expected to have

positive effects on the behaviors of J_c. The field dependences of J_c at 5 K and 20 K of pristine and Ni-ion irradiated MgB_2 films were presented in Figure 5.6 (a-b).

The variations of J_c with increasing the Ni-ion dose at different fields, in which the enhancements of J_c were observed at high field regions are showed in Figure 5.7 (a-b). The overall reduction of J_c as an increasing field was found for all films. By irradiation of Ni ions, the values of J_c values were clearly enhanced for the dose of 3 × 10^{13}, 5 × 10^{13}, and 7 × 10^{13} ions/cm^2 at high field regions.

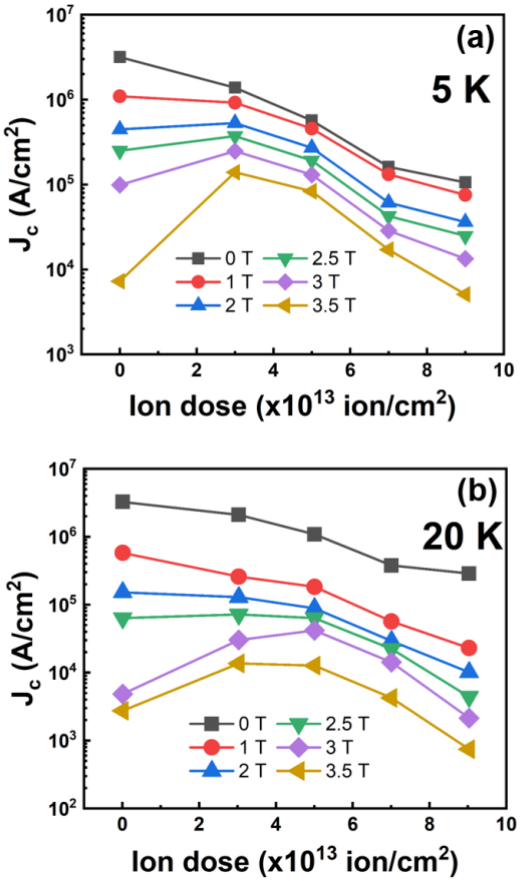


Figure 5.7. *Variations of J_c at 5 K (a) and 20 K (b) with increasing Ni-ion dose across different fields, showing high-field enhancements*

To quantitatively analyze the enhancements of J_c, the plots of J_c vs. fields using the double-logarithmic scale were given in Figure 5.8 (a-b). Two distinct regimes might be classified. The single vortex pinning existed at low field region, in which all penetrated vortices were individually pinned, and revealed by the field

independence of J_c. The collective pinning regime at the intermediate field region, in which the vortex-vortex interaction becomes dominant, and described by the field dependence of $J_c \sim H^{-\beta}$. The exponent β has been reported to reflect the pinning strength in type-II superconductors [42,45].

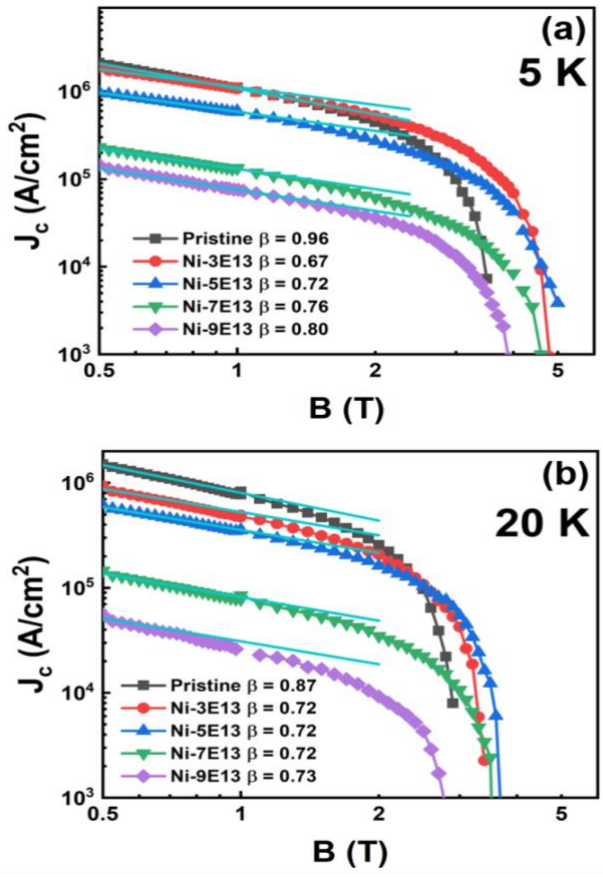


Figure 5.8. *Double logarithmic scaled field dependence of evolution of the J_c under applied magnetic field for Ni-ion irradiated MgB_2 films*

(in figure 5.8 the power law $J_c \sim H^{-\beta}$ was applied in the intermediate field region (a) 5 K, and (b) 20 K)

In the Table 5.6, at T = 5 K, value of β was decreased from 0.96 for the pristine MgB_2 to the minimum of 0.67 for Ni-3E13 film. A similar tendency was also observed at T = 20 K. Theoretically, the weak and strong pinning mechanisms were characterized by β = 1 and β = 0.5, respectively [17,44]. Therefore, in this work, the decrease in β might be used as evidence for the partial shift from weak to strong

pinning mechanisms via systems of distortions and defects caused by the Ni-ion irradiations.

Table 5.6. *The β values for pristine and Ni-ion irradiated MgB_2 films*

Films	**β**	
	5 K	**20 K**
Pristine	0.96	0.87
Ni-3E13	0.67	0.72
Ni-5E13	0.72	0.72
Ni-7E13	0.76	0.72
Ni-9E13	0.80	0.73

5.3.3 Flux pinning mechanisms in pristine and Ni-ion irradiated MgB_2 films

Next, the investigation of the nature of pinning in the pristine and Ni-ion irradiated MgB_2 films were performed. The pinning force density F_p was calculated from the field dependent J_c data by using the relation $F_p = B \times J_c$. Typically, J_c and F_p of type-II superconductors rapidly vanished at B_{irr}. Hence, B_{irr} has been widely used to define the normalized field b ($b = B/B_{irr}$,). Plots of the pinning force density f_p of all samples ($f_p = F_p/F_{p,max}$) versus b are provided in Figure 5.9.

Scaling behavior of the flux pinning in the MgB_2 films were analyzed by using the Dew-Hughes model [19]:

$$f_p = Ab^p(1-b)^q \tag{5.4}$$

where A was a parameter that was independent of the applied field, p and q were the fitting parameters reflecting the type of pinning.

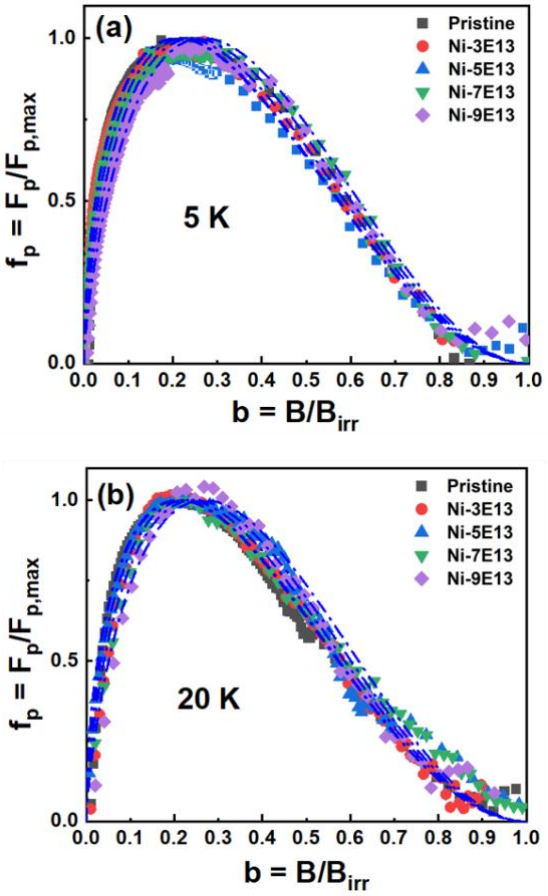


Figure 5.9. *Plot of normalized volume pinning force f_p ($f_p = F_p/F_{p,max}$, on normalized field b, $b = B/B_{irr}$, of the pristine and Ni-ion irradiated MgB_2 films at (a) 5 K and (b) 20 K)*

It would be said that the experimental data were well fitted with the theoretical model at low field region. Values of p, q and b_{peak}= p/(p+q) were estimated. For all of the MgB_2 film, the value of q was found to be maintained as 2, which might indicate the existence of core interaction [19,44,93,107]. The finding would be used as solid evidence for the idea that core interaction has been identified to be the dominant interaction in type-II superconductors. Values of p and b_{peak} were then considered to identify the details of core pinning types in the MgB_2 films. For the pristine MgB_2 film, p was ~ 0.53 and b_{peak} was ~ 0.21, which suggested that the normal core surface pinning was dominant. Experimentally, the MgB_2 samples fabricated by using the HPCVD were nearly single crystal films as discussed in the XRD results. When the

field was applied parallel to the c-axis of the films, the grain boundaries would serve effectively as the surface pinning centers. For the Ni-ion irradiated MgB_2 films using low ion doses (Ni-3E13 and Ni-5E13 samples), the slight increases in values of both p and b_{peak}were obtained. However, the increases were remarkable, reaching p ~ 0.73 and b_{peak}~ 0.27 when using high ion doses (Ni-7E13 and Ni-9E13 samples). According to the classification of Dew-Hughes, theoretical values of p = 1 and q = 2 belong to normal point pinning. In previous studies, the existence of normal point pinning in MgB_2 films were likely to be attributed to the distortion in crystal structure, lattice mismatch, or incomplete growth of superconducting grains [42,44,45,82,85].

In this work, the Ni ions were irradiated throughout the film thickness. The irradiation process was believed to generate point defects such as ion tracks, lattice distortion... homogeneously distributed inside the MgB_2 films. As a result, the partial shift from normal surface to normal point pinning was possibly obtained, which led to the co-existence of two pinning mechanisms in Ni-7E13 and Ni-9E13 samples.

5.4. The best enhancement of J_c in MgB_2 bulks and films

Depend on the results in enhancements of J_c, this section shows a comparison of the maximum enhancement of J_c in the dissertation. The condition for the strongest increase in J_c was when the MgB_2 films were irradiated with Ni ions at a dose of 3×10^{13} ions/cm^2 and Nb ions at a dose of 7×10^{13} ions/cm^2. Beside, thanks to the co-addition of SiC and Mg into MgB_2 pure bulks, the greatest J_c enhancement of J_c was obtained for the sample with 0.5 mol Mg + 10 wt.% SiC sintered at 900 °C for 1 h. The highest value of J_c in films and bulk were depicted in Figure 5.10.

In Figure 5.10, the value J_c of MgB_2 films are much larger than that of MgB_2 bulk, especially in MgB_2 films irradiated by Ni-ion, the J_c reaches maximum value. It has been widely proposed that the J_c of the films is usually higher than that of the bulks if the same superconductor is used. Possible reasons for this higher value of J_c have been attributed to the elimination of samples' porosity leading to the reduction of weak links between the superconducting grains; strengthening of 2D pinning, and

an increase in the vacancies. The better performance of J_c in the case of Ni-ion irradiations might be explained by (i) the magnetic properties of Ni ion, which probably induced the stronger attraction and pinning effect to the vortices; and (ii) the higher projected range of Ni leading to the fact that most of Ni ions passed through the MgB_2 film thickness. As a result, the higher density of point-like defects was obtained in the case of Ni-ion irradiations, which generate the stronger enhancement of J_c at high field region

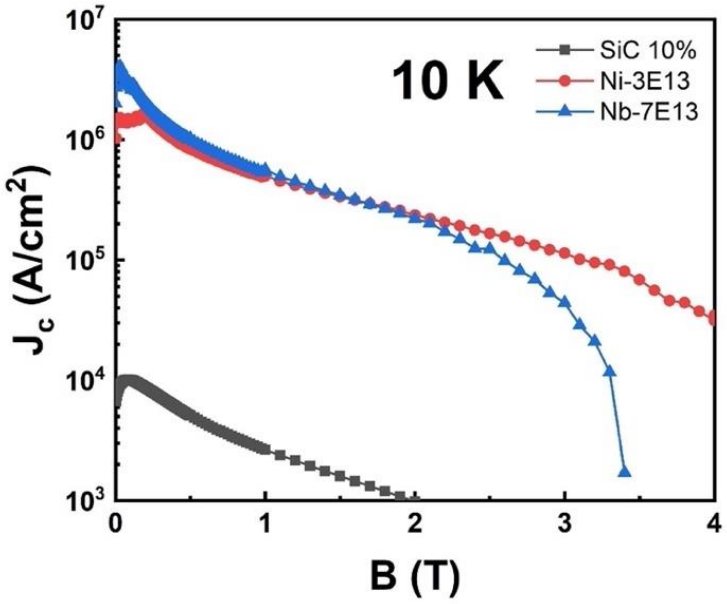


Figure 5.10. *The best enhancements of J_c in MgB_2 bulks and films at 10 K*

Regarding the applications of materials, the most prominent advantage of MgB_2 bulk lies in its practicality and manufacturability. From an economic standpoint, MgB_2 bulk is far more accessible. The raw materials - magnesium and boron - are abundant and inexpensive, and the synthesis process, typically involving solid-state reaction or diffusion methods, is straightforward and scalable. This ease of fabrication translates directly into high practical applicability. MgB_2 bulks can be readily formed into wires, tapes, and complex shapes using standard powder-in-tube (PIT) techniques, making it a leading candidate for large-scale industrial applications such as magnetic resonance imaging (MRI) magnets, power transmission cables, and

magnetic levitation systems. Its cost-effectiveness and established manufacturing routes give it a decisive edge in sectors where large volumes of material are required. However, this practicality comes with a trade-off regarding superconducting performance. MgB_2 bulks often suffer from porosity, weak grain connectivity, and the presence of impurities introduced during the pressing and sintering processes. These microstructural imperfections act as pinning centers but also limit the J_c, particularly in the presence of external magnetic fields. Consequently, while bulk forms are sufficient for many low-to-moderate field applications, their performance tends to degrade more rapidly under high-field conditions. In contrast, MgB_2 thin films represent the pinnacle of the material's intrinsic superconducting properties. Grown through sophisticated techniques (such as HPCVD), thin films can achieve high density and exceptional crystallinity. These characteristics result in superconducting parameters, including significantly higher enhanced J_c. For research purposes and high-frequency applications, such as superconducting radio-frequency (SRF) cavities or sensitive superconducting quantum interference devices (SQUIDs), the performance of thin films is unmatched. In summary, the choice between MgB_2 bulks and films is defined by the specific application requirements. Bulks MgB_2 serve as the primary cornerstone of this class; they are cost-effective and straightforward to fabricate, and highly practical for large-scale devices, though they sacrifice some superconducting performance. MgB_2 films, on the other hand, offer state-of-the-art superconducting properties but are hindered by high production costs and significant challenges in scaling up to conductor lengths, limiting their use to specialized, performance-driven applications.

5.5. Conclusions of chapter 5

In terms of structural variations, 1 MeV Ni-ion irradiation preserves the fundamental hexagonal crystal structure of the MgB_2 films. However, increasing the Ni-ion dose induces structural distortions, characterized by a slight expansion in the c-axis lattice parameter and a concurrent decrease in electron-phonon coupling. These alterations provide evidence for the generation and growth of point-like defects

through ion tracks during the Ni-ion irradiation process: The c-axis lattice constant increased from 3.521 Å (pristine) to 3.550 Å (Ni-9E13), indicating lattice expansion; The FWHM of the (0002) XRD peak increased from 0.257° (pristine) to 0.479° (irradiated), showing a degradation in crystallinity; Tensile strain was observed, with the Williamson-Hall analysis supporting increased strain with higher ion doses, which contributed to grain boundary pinning; The E_{2g} peak position tended to slightly shift from 598 cm^{-1} (pristine) to 560 cm^{-1} (Ni-9E13), showing increased lattice distortions.

In terms of superconductivity, the induced lattice distortions lead to a slight reduction of the T_c from 39.56 K to 32.5 K and the EPC constant slightly declines from 1.0499 in the pristine sample to 0.9599 in the Ni-9E13 sample. The decrease T_c appears in almost all studies of MgB_2 in the world; when compared to other studies, these reductions were not significant and still remain above 30 K. However, pinning strength (β) decreased from 0.96 (pristine) to 0.67 (Ni-3E13), reflecting a slight shift from weak pinning to stronger pinning mechanisms due to ion-induced defects. Therefore, there were enhancements of the J_c under high fields by the partial shift the pinning mechanism from normal surface pinning to normal point pinning after irradiation. The investigation also found the best enhancement of J_c achieved in the Ni-3E13 sample.

CONCLUSIONS

MgB_2 has been shown to have a variety of interesting properties for power-related applications, which consists of a medium-high value of T_c ~ 39 K, the relatively high values of B_{c2} and J_c. To explore the application area, the enhancements of B_{c2} and J_c are strongly required. In this dissertation, the improvements in J_c of MgB_2 superconductors have been presented.

First, the influence of co-additions of Mg and SiC on crystal structure and superconductivity of MgB_2 bulks are studied. The pure MgB_2 and (y wt.% SiC + Mg + MgB_2) bulks were prepared using the solid-state reaction methods. The value of T_c of the MgB_2 bulks gradually decreased after the addition; however, these values remain above 37 K, nearly the value of the pure sample (38.09 K), with the difference approximately 1 K. This is an outstanding result in maintaining T_c. Additionally, the value of B_{c2} in all of MgB_2 bulks after addition was higher than that of pure one (14.64 T). The J_c was found to increase in all the chemical added MgB_2 bulks. The pinning mechanism was found to be the normal surface pinning (with p = 0.5 and b_{peak} = 0.2) in all pure and (SiC + Mg + MgB_2) co-added bulks.

Second, the effects of Nb-ions irradiation on crystal structure and critical parameters of MgB_2 films were investigated. The pristine MgB_2 films with the average thickness of ~ 400 nm were fabricated by the HPCVD system in high quality (without impurity phases). After irradiation by Nb-ions (the energy = 1 MeV, ion beam was accelerated perpendicularly to the surface of films and the doses ranged from 3×10^{13} ions/cm^2 to 9×10^{13} ions/cm^2), the structure variations were investigated. The results not only can irradiation maintain the MgB_2 crystallinity in irradiated films, but the critical parameters also were maintained and improved. In detail, the lattice distortions lead to a slight reduction of the T_c from 39.56 K (pristine) to 36.25 K (9×10^{13} ions/cm^2), which still remains above 36 K. Meanwhile, there were enhancements of the J_c in high fields, indicated by the partial shift of the pinning mechanism from normal surface pinning to normal point pinning after irradiation.

The investigation also confirmed the best enhancement of J_c achieved in the dose of 3×10^{13} ions/cm^2.

Third, the impacts of Ni-ions irradiation on crystal structure and critical parameters of MgB_2 films were investigated. With the same irradiated conditions, the degradation of the crystallinity in the Ni-ion irradiated MgB_2 films seems higher when compared to Nb-irradiated films. The obvious evidence was revealed through the PDOS appearance in Raman spectrum, with the clearly higher peaks when the doses of irradiation rise. As a result of more structural distortions, the decrease in T_c from 39.56 K (pristine) to 32.5 K (9×10^{13} ions/cm^2) was witnessed, however still maintained above 32 K. The higher enhancements of J_c in Ni-ion irradiated MgB_2 films were revealed by comparing the value of pinning strength β, (β ~ 0.67 at 5 K, which approached the theoretical value of strong pinning β = 0.5). The finding might indicate the shift from weak to relatively strong pinning. The partial shift of the pinning mechanism from normal surface pinning to normal point pinning after irradiation proved that J_c can be enhanced in high fields. This investigation also confirmed the best enhancement of J_c achieved in the dose of 3×10^{13} ions/cm^2.

Overall, values of in-field J_c - *which are the most important results in this dissertation* - were enhanced in both MgB_2 bulks and films after addition or irradiation. The J_c in the MgB_2bulks was enhanced in the range of lower field, which possibly reflected to the fact that surface pinning was dominant in the bulk samples. Interestingly, the J_c in the Nb- and Ni-ion irradiated MgB_2 films improved in the high field, which might be attributed to the slight shift to normal point pinning. The stronger enhancement of J_c seems to be obtained in the Ni-ion irradiation, which might be explained by the higher density of the point defects in the films in the form of ion-tracks, lattice distortions.

From the main results of the dissertation, future research might expand the investigations in optimization and systematization of improving J_c in MgB_2 superconductors for practical applications.

LIST OF PUBLICATIONS

1. Duc H. Tran, **Duong T.T. Nhan*,** An T. Pham, Tien Le, Viet Cuong Le, Won Nam Kang, Dzung T. Tran, Hong Gu Lee, Jungseek Hwang, Nguyen Hoang Nam, Bui Thị Hoa, Nguyen T. Nghia, Phan Hai, Dang T.B. Hop, M. Doğruer, "Local structure, electron - phonon coupling and flux pinning properties in MgB_2 thin film using the irradiation of Nb", *Ceramics International* (2026), 52,18, 33406 - 33414.

2. Duc H. Tran, **Duong T.T. Nhan*,** An T. Pham, Nguyen Hoang Nam, Kieu Xuan Thuy, Tien Le, Viet Cuong Le, Vuong T.A. Hong, Hannoh Lee, Tuson Park, Hoo-Keong Peh, Soo-Kien Chen, M. Dogruer, "Effects of SiC and Mg co-addition on the superconducting and microhardness properties of MgB_2", *Ceramics International* (2025), 51, 19(A), 27457-27464.

3. **Duong T.T. Nhan**, An T. Pham, Tien Le, Won-Nam Kang, Dzung T. Tran, Hong-Gu Lee, Jungseek Hwang, Nguyen Hoang Nam, Ha H. Pham, Khoi M. C. Pham, Pham Ngoc Thao, Phan Hai, Soo-Kien Chen, M. Dogruer, Kieu Xuan Thuy, Duc H. Tran, "Effects of Ni irradiation on electron - phonon coupling and flux pinning in MgB_2 film via Raman spectroscopy", *J. Appl. Phys.* (2025) 138, 073901.

4. **Duong Thi Thanh Nhan**, Pham The An, Le Minh Tien, Pham Hoang Ha, Nguyen The Nghia, Nguyen Khac Man, Phan Hai, Tran Hai Duc, (2025) "Effects of Ion Irradiations on Crystal Structure and Superconducting Properties of MgB2 Films", *VNU Journal of Science: Mathematics - Physics* (2025), 41 (3), 99-106.

REFERENCES

[1] Ahmad I., Sarun P.M., (2024), "Effect of nano-Ag addition on the superconducting properties of MWCNT doped magnesium diboride superconductor", *J. Alloys Compd.* 990p. 174317.

[2] Askerzade I.N., Gencer A., G l N., Kili A., (2002), "Two-band Ginzburg Landau theory for the lower critical field Hc1 in MgB2", *Supercond. Sci. Technol.* 15(6), pp. L17–L20.

[3] Askerzade I.N., Gencer A., Güçlü N., (2002), "On the Ginzburg-Landau analysis of the upper critical field Hc2 in MgB2", *Supercond. Sci. Technol.* 15(2), pp. L13–L16.

[4] Baker A.A., Aji L.B.B., Bae J.H., Stavrou E., Beckham J.L., McCall S.K., Kucheyev S.O., (2019), "Control of superconductivity in MgB2 by ion bombardment", *J. Phys. D Appl. Phys.* 52(29), p. 295302.

[5] Bardeen J., Cooper L.N., Schrieffer J.R., (1957), "Microscopic Theory of Superconductivity", *Physical Review* 106(1), pp. 162–164.

[6] BEAN C.P., (1964), "Magnetization of High-Field Superconductors", *Rev. Mod. Phys.* 36(1), pp. 31–39.

[7] Bean C.P., (1962), "Magnetization of Hard Superconductors", *Phys. Rev. Lett.* 8(6), pp. 250–253.

[8] Blatter G., Feigel'man M. V, Geshkenbein V.B., Larkin A.I., Vinokur V.M., (1994), "Vortices in high-temperature superconductors", *Rev. Mod. Phys.* 66(4), pp. 1125–1388.

[9] Bohnen K.-P., Heid R., Renker B., (2001), "Phonon Dispersion and Electron-Phonon Coupling in MgB2 and AlB2", *Phys. Rev. Lett.* 86(25), pp. 5771–5774.

[10] Bouquet F., Wang Y., Fisher R.A., Hinks D.G., Jorgensen J.D., Junod A., Phillips N.E., (2001), "Phenomenological two-gap model for the specific heat of MgB2", *Europhysics Letters (EPL)* 56(6), pp. 856–862.

[11] Brinkman A., Golubov A.A., Rogalla H., Dolgov O. V, Kortus J., Kong Y., Jepsen O., Andersen O.K., (2002), "Multiband model for tunneling in MgB2 junctions", *Phys. Rev. B* 65(18), p. 180517.

[12] Bugoslavsky Y., Cohen L.F., Perkins G.K., Polichetti M., Tate T.J., Gwilliam R., Caplin A.D., (2001), "Enhancement of the high-magnetic-field critical current density of superconducting MgB2 by proton irradiation", *Nature* 411(6837), pp. 561–563.

[13] Campbell A.M., Evetts J.E., Dew-Hughes D., (1968), "Pinning of Flux Vortices in Type II Superconductors", *Philosophical Magazine* 18(152), pp. 313–343.

[14] Chen D.-X., Goldfarb R.B., (1989), "Kim model for magnetization of type-II superconductors", *J. Appl. Phys.* 66(6), pp. 2489–2500.

[15] Chen X.K., Konstantinović M.J., Irwin J.C., Lawrie D.D., Franck J.P., (2001), "Evidence for Two Superconducting Gaps in MgB2", *Phys. Rev. Lett.* 87(15), p. 157002.

[16] Dadiel J.L., Naik S.P.K., Pęczkowski P., Sugiyama J., Ogino H., Sakai N., Kazuya Y., Warski T., Wojcik A., Oka T., Murakami M., (2021), "Synthesis of Dense MgB2 Superconductor via In Situ and Ex Situ Spark Plasma Sintering Method", *Materials* 14(23), p. 7395.

[17] Dam B., Huijbregtse J.M., Klaassen F.C., van der Geest R.C.F., Doornbos G., Rector J.H., Testa A.M., Freisem S., Martinez J.C., Stäuble-Pümpin B., Griessen R., (1999), "Origin of high critical currents in YBa2Cu3O7−δ superconducting thin films", *Nature* 399(6735), pp. 439–442.

[18] Dariusz Czerwiński, (2013), *Modelling the Critical Parameters of High Temperature Superconductor Devices in Transient States* Lublin University of Technology, Lublin.

[19] Dew-Hughes D., (1974), "Flux pinning mechanisms in type II superconductors", *Philosophical Magazine* 30(2), pp. 293–305.

[20] Dogruer M., Gorur O., Zalaoglu Y., Ozturk O., Yildirim G., Varilci A., Terzioglu C., (2013), "Role of diffusion-annealing time on the superconducting, microstructural and mechanical properties of Cu-diffused bulk MgB2 superconductor", *Journal of Materials Science: Materials in Electronics* 24(1), pp. 352–361.

[21] Dou S.X., Soltanian S., Horvat J., Wang X.L., Zhou S.H., Ionescu M., Liu H.K., Munroe P., Tomsic M., (2002), "Enhancement of the critical current density and flux pinning of MgB2 superconductor by nanoparticle SiC doping", *Appl. Phys. Lett.* 81(18), pp. 3419–3421.

[22] Eisterer M., (2007), "Magnetic properties and critical currents of MgB_2", *Supercond. Sci. Technol.* 20(12), pp. R47–R73.

[23] Ferdeghini C., Ferrando V., Grassano G., Ramadan W., Braccini V., Putti M., Manfrinetti P., Palenzona A., (2002), "Transport properties of c-oriented MgB2 thin films grown by pulsed laser deposition", *Physica C Supercond.* 372–376pp. 1270–1273.

[24] Ferrando V., Pallecchi I., Tarantini C., Marré D., Putti M., Ferdeghini C., Gatti F., Aebersold H.U., Lehmann E., Haanappel E., Sheikin I., Orgiani P., Xi X.X., (2007), "Systematic study of disorder induced by neutron irradiation in MgB2 thin films", *J. Appl. Phys.* 101(4), .

[25] Floris A., Profeta G., Lathiotakis N.N., Lüders M., Marques M.A.L., Franchini C., Gross E.K.U., Continenza A., Massidda S., (2005), "Superconducting Properties of MgB2 from First Principles", *Phys. Rev. Lett.* 94(3), p. 037004.

[26] G B.J., Takashige.M, A M.K., (1986), "Possible High Tc Superconductivity in the Ba-La-Cu-O System", *Zeitschrift für Physik B Condensed Matter* 64pp. 189–193.

[27] G B.J., Takashige.M, A M.K., (1987), "Susceptibility Measurements Support High-Tc Superconductivity in the Ba-La-Cu-O", *System Europhys Letters* 3p. 379.

[28] Gajda D., Babij M., Zaleski A., Avci D., Karaboga F., Yetis H., Belenli I., Zasada D., Szymański D., Małecka M., Gil W., Czujko T., (2024), "The influence of Sm2O3 dopant on structure, morphology and transport critical current density of MgB2 wires investigated by using the transmission electron microscope", *Journal of Magnesium and Alloys* 12(12), pp. 5061–5078.

[29] Gajda D., Morawski A., Zaleski A.J., Häßler W., Nenkov K., Małecka M., Rindfleisch M.A., Hossain M.S.A., Tomsic M., (2016), "Experimental research of high field pinning centers in 2% C doped MgB2 wires at 20 K and 25 K", *J. Appl. Phys.* 120(11), .

[30] Gajda D., Zaleski A., Morawski A., Cetner T., Thong C.J., Rindfleisch M.A., (2016), "Point pinning centers in SiC doped MgB2 wires after HIP", *Supercond. Sci. Technol.* 29(8), p. 085010.

[31] Gao Z., Wang D., Zhang X., Ma Y., Awaji S., Nishijima G., Watanabe K., Flükiger R., (2010), "Simultaneous introduction of scattering and pinning in organic rare-earth salt doped MgB2 tapes", *Supercond. Sci. Technol.* 23(4), p. 045024.

[32] Ghorbani S.R., Farshidnia G., Wang X.L., Dou S.X., (2014), "Flux pinning mechanism in SiC and nano-C doped MgB2: evidence for transformation from Tc to pinning", *Supercond. Sci. Technol.* 27(12), p. 125003.

[33] Ghorbani S.R., Wang X.L., Dou S.X., Lee S.-I., Hossain M.S.A., (2008), "Flux-pinning mechanism in silicone-oil-doped MgB2: Evidence for charge-carrier mean free path fluctuation pinning", *Phys. Rev. B* 78(18), p. 184502.

[34] Goncharov A.F., Struzhkin V. V, Gregoryanz E., Hu J., Hemley R.J., Mao H., Lapertot G., Bud'ko S.L., Canfield P.C., (2001), "Raman spectrum and lattice parameters of MgB2 as a function of pressure", *Phys. Rev. B* 64(10), p. 100509.

[35] Hapipi N.M., Chen S.K., Shaari A.H., Kechik M.M.A., Lim K.P., Shabdin M.K., Tan K.B., Lee O.J., Miryala M., (2024), "Co-addition of nano-Si and LaB6 effects on the critical current density of MgB2 superconductor", *Journal of Alloys and Compounds Communications* 3p. 100020.

[36] Higuchi T., Yoo S.I., Murakami M., (1999), "Comparative study of critical current densities and flux pinning among a flux-grown NdBa2Cu3Oy single crystal, melt-textured Nd-Ba-Cu-O, and Y-Ba-Cu-O bulks", *Phys. Rev. B* 59(2), pp. 1514–1527.

[37] Hlinka J., Gregora I., Pokorný J., Plecenik A., Kúš P., Satrapinsky L., Beňačka Š., (2001), "Phonons in MgB2 by polarized Raman scattering on single crystals", *Phys. Rev. B* 64(14), p. 140503.

[38] Hosseinzadeh M., Ghorbani S.R., Arabi H., (2020), "On the Determination of Pinning Mechanisms and Regimes in Type-II Superconductors with Weak Thermal Fluctuations", *J. Supercond. Nov. Magn.* 33(4), pp. 971–980.

[39] Hunte F., Jaroszynski J., Gurevich A., Larbalestier D.C., Jin R., Sefat A.S., McGuire M.A., Sales B.C., Christen D.K., Mandrus D., (2008), "Two-band superconductivity in LaFeAsO0.89F0.11 at very high magnetic fields", *Nature* 453(7197), pp. 903–905.

[40] Ischenko G., Klaumünzer S., Neumüller H., Adrian H., Müller P., (1978), "Superconductivity of Nb3Sn, Nb, V, Pb and Sn after low temperature irradiation with 25 MeV oxygen ions", *Journal of Nuclear Materials* 72(1–2), pp. 212–224.

[41] Jung S., Son S., Pham D., Lim W.C., Song J., Kang W.N., Park T., (2021), "Corrigendum: Influence of carbon-ion irradiation on the superconducting critical properties of MgB2 thin films", *Supercond. Sci. Technol.* 34(12), p. 129501.

[42] Jung S.-G., Pham D., Lee J.M., Han Y., Kang W.N., Park T., (2021), "Effects of surface damage on critical current density in MgB2 thin films", *Current Applied Physics* 22pp. 14–19.

[43] Jung S.-G., Pham D., Park T.-H., Choi H.-Y., Seo J.W., Kang W.N., Park T., (2019), "Giant proximity effect in single-crystalline MgB2 bilayers", *Sci. Rep.* 9(1), p. 3315.

[44] Jung S.-G., Seong W.K., Kang W.N., (2013), "Flux Pinning Mechanism in Single-Crystalline MgB2 Thin Films", *J. Physical Soc. Japan* 82(11), p. 114712.

[45] Jung S.-G., Son S.-K., Pham D., Kang W.N., Lim W.C., Song J., Park T., (2019), "Enhanced Critical Current Density in the Carbon-Ion Irradiated MgB $_2$ Thin Films", *J. Physical Soc. Japan* 88(3), p. 034716.

[46] Jung S.-G., Son S.-K., Pham D., Lim W.C., Song J., Kang W.N., Park T., (2019), "Influence of carbon-ion irradiation on the superconducting critical properties of MgB $_2$ thin films", *Supercond. Sci. Technol.* 32(2), p. 025006.

[47] Kamerlingh-Onnes.H, (1911), "Further experiments with liquid Helium. C. On the electrical resistance of pure metals, at very low temperature, etc. VI. The resistance of pure Mercury at Helium temperatures", *Communication - Leiden* 120bpp. 261–263.

[48] Kang B., Putri W.B.K., Kang W.N., (2019), "Effect of SiC buffer layer on flux pinning property of MgB2 tapes", *Current Applied Physics* 19(6), pp. 670–674.

[49] Karapetrov G., Iavarone M., Kwok W.K., Crabtree G.W., Hinks D.G., (2001), "Scanning Tunneling Spectroscopy in MgB2", *Phys. Rev. Lett.* 86(19), pp. 4374–4377.

[50] Kaya N., (2025), "Analysis of the physical properties of MgB2 superconductor with Zn(NO3)2·6H2O addition", *Journal of Materials Science: Materials in Electronics* 36(1), p. 5.

[51] Kaya N., Çavdar Ş., Öztürk Ö., Ada H., Koralay H., (2021), "Investigation of microhardness properties of the multi-walled carbon nanotube additive MgB2 structure by using the vickers method", *Cryogenics (Guildf).* 116p. 103295.

[52] Kayed T.S., Ercan İ., Alagha O., (2013), "γ Irradiation of Bulk MgB2 Superconductor", *J. Supercond. Nov. Magn.* 26(12), pp. 3419–3422.

[53] Kim H.-J., Kang W.N., Choi E.-M., Kim M.-S., Kim K.H.P., Lee S.-I., (2001), "High Current-Carrying Capability in c -Axis-Oriented Superconducting MgB2 Thin Films", *Phys. Rev. Lett.* 87(8), p. 087002.

[54] Kim H.-J., Kang W.N., Choi E.-M., Kim M.-S., Kim K.H.P., Lee S.-I., (2001), "High Current-Carrying Capability in MgB2 Thin Films", *Phys. Rev. Lett.* 87(8), p. 87002.

[55] Kim N.K., Tan K.S., Jun B.-H., Park H.W., Joo J., Kim C.-J., (2008), "Effect of charcoal doping on the superconducting properties of MgB2 bulk", *Physica C Supercond.* 468(15–20), pp. 1375–1378.

[56] Kim S., van Duong P., Ha D., Oh Y.-H., Kang W.N., Hong S.P., Kim R., Chai J.S., (2016), "Effects of α-particle beam irradiation on superconducting properties of thin film MgB2 superconductors", *Progress in Superconductivity and Cryogenics* 18(2), pp. 8–13.

[57] Koblischka M.R., Sosnowski J., (2005), "Temperature-dependent scaling of pinning force data in Bi-based high-Tc superconductors", *Eur. Phys. J. B* 44(3), pp. 277–280.

[58] Koparan E.T., Savaskan B., Ozturk O., Kaya S., Aksoy C., Wang J., Speller S.C., Grovenor C.R.M., Gencer A., Yanmaz E., (2016), "Changes in mechanical and structural properties of Bi-2212 added MgB2 superconductors", *Journal of Materials Science: Materials in Electronics* 27(6), pp. 6060–6070.

[59] Kortus J., Mazin I.I., Belashchenko K.D., Antropov V.P., Boyer L.L., (2001), "Superconductivity of Metallic Boron in MgB2", *Phys. Rev. Lett.* 86(20), pp. 4656–4659.

[60] Kumar D., Muralidhar M., Higuchi M., Ramachandra Rao M.S., Murakami M., (2017), "Raman spectroscopy of carbon doped MgB2 prepared using carbon encapsulated boron as precursor", *J. Alloys Compd.* 723pp. 751–756.

[61] Kwok W.-K., Welp U., Glatz A., Koshelev A.E., Kihlstrom K.J., Crabtree G.W., (2016), "Vortices in high-performance high-temperature superconductors", *Reports on Progress in Physics* 79(11), p. 116501.

[62] Larkin A.I., Ovchinnikov Yu.N., (1979), "Pinning in type II superconductors", *J. Low Temp. Phys.* 34(3–4), pp. 409–428.

[63] Le T., Pham H.H., Nghia N.T., Nam N.H., Miyanaga T., Tran D.H., Kang W.-N., (2023), "Effects of Sn-ion irradiation on local structure and flux pinning properties of MgB2 thin films", *Ceram. Int.* 49(2), pp. 2715–2720.

[64] Le T., Tran D.T., Lee H.G., Choi W.S., Hwang J., Kang W.N., Park T., Miyanaga T., Yun J., Lee Y., Kim J., Thao P.N., Tran D.H., (2024), "Influence of aluminum diffusion on MgB2 films grown by hybrid physical–chemical vapor deposition using amorphous aluminum buffers", *Results Phys.* 58p. 107447.

[65] Lee S., Masui T., Yamamoto A., Uchiyama H., Tajima S., (2003), "Carbon-substituted MgB2 single crystals", *Physica C Supercond.* 397(1–2), pp. 7–13.

[66] Li W.X., Chen R.H., Li Y., Zhu M.Y., Jin H.M., Zeng R., Dou S.X., Lu B., (2008), "Raman study on the effects of sintering temperature on the Jc(H) performance of MgB2 superconductor", *J. Appl. Phys.* 103(1), .

[67] Li W.X., Li Y., Chen R.H., Zeng R., Dou S.X., Zhu M.Y., Jin H.M., (2008), "Raman study of element doping effects on the superconductivity of MgB2", *Phys. Rev. B* 77(9), p. 94517.

[68] Li W.X., Li Y., Chen R.H., Zeng R., Zhu M.Y., Jin H.M., Dou S.X., (2008), "Electron–phonon coupling properties in MgB_2 observed by Raman scattering", *Journal of Physics: Condensed Matter* 20(25), p. 255235.

[69] London F., London H., (1935), "The electromagnetic equations of the supraconductor", *Proc. R. Soc. Lond. A Math. Phys. Sci.* 149(866), pp. 71–88.

[70] Mankowsky R., Subedi A., Först M., Mariager S.O., Chollet M., Lemke H.T., Robinson J.S., Glownia J.M., Minitti M.P., Frano A., Fechner M., Spaldin N.A., Loew T., Keimer B., Georges A., Cavalleri A., (2014), "Nonlinear lattice dynamics as a basis for enhanced superconductivity in YBa2Cu3O6.5", *Nature* 516(7529), pp. 71–73.

[71] McMillan W.L., (1968), "Transition Temperature of Strong-Coupled Superconductors", *Physical Review* 167(2), pp. 331–344.

[72] Meissner W., Ochsenfeld R., (1933), "Ein neuer Effekt bei Eintritt der Supraleitfahigkeit", *Naturwissenschaften* 21(44), pp. 787–788.

[73] Meletov K.P., Kulakov M.P., Kolesnikov N.N., Arvanitidis J., Kourouklis G.A., (2002), "Raman spectra of MgB2 at high pressure and topological electronic transition", *Journal of Experimental and Theoretical Physics Letters* 75(8), pp. 406–409.

[74] Muranaka T., Akimitsu J., (2011), "Superconductivity in MgB2", *Zeitschrift für Kristallographie* 226(4), .

[75] Nagamatsu J., Nakagawa N., Muranaka T., Zenitani Y., Akimitsu J., (2001), "Superconductivity at 39 K in magnesium diboride", *Nature* 410(6824), pp. 63–64.

[76] Nik-Jaafar N.A., Abd-Shukor R., Chen S.K., (2012), "Elastic Properties of MgB2 and SiC-Doped MgB2 Superconductors", *Adv. Mat. Res.* 501pp. 304–308.

[77] Ojha N., Malik V.K., Singla R., Bernhard C., Varma G.D., (2010), "The effect of carbon and rare earth oxide co-doping on the structural and superconducting properties of MgB2", *Supercond. Sci. Technol.* 23(4), p. 045005.

[78] Osborn R., Goremychkin E.A., Kolesnikov A.I., Hinks D.G., (2001), "Phonon Density of States in MgB2", *Phys. Rev. Lett.* 87(1), p. 17005.

[79] Patel D., Qiu W., Mustapić M., Knott J.C., Ma Z., Gajda D., Shahabuddin M., Xu J., Choi S., Tomsic M., Dou S.X., Yamauchi Y., Kim J.H., Hossain M.S. Al, (2018), "Evaluation of a solid nitrogen impregnated MgB2 racetrack coil", *Supercond. Sci. Technol.* 31(10), p. 105010.

[80] Peh H.K., Chen S.K., Hapipi N.M., Kechik M.M.A., Lim K.P., Tan K.B., Shaari A.H., Shabdin M.K., Mohamed A.R.A., Lee O.J., Huy N.Q., Tran D.H., Miryala M., (2025), "Enhancement of critical current density in Mg incorporated ex-situ MgB2 via co-addition of B4C and Dy2O3", *J. Alloys Compd.* 1012p. 178233.

[81] Perkins G.K., Bugoslavsky Y., Caplin A.D., Moore J., Tate T.J., Gwilliam R., Jun J., Kazakov S.M., Karpinski J., Cohen L.F., (2004), "Effects of proton irradiation and ageing on the superconducting properties of single crystalline and polycrystalline MgB2", *Supercond. Sci. Technol.* 17(1), pp. 232–235.

[82] Pham D., Jung S.-G., Tran D.H., Park T., Kang W.N., (2019), "Effects of oxygen ion implantation on single-crystalline MgB2 thin films", *J. Appl. Phys.* 125(2), .

[83] Pham D., Van Ngoc H., Jung S.-G., Kang D.J., Kang W.N., (2018), "Enhanced critical current density of MgB2 thin films deposited at low temperatures by ZnO seed impurity", *Current Applied Physics* 18(6), pp. 762–766.

[84] Postorino P., Congeduti A., Dore P., Nucara A., Bianconi A., Castro D. Di, Negri S. De, Saccone A., (2001), "Effect of the Al content on the optical phonon spectrum in MgAlB2", *Phys. Rev. B* 65(2), p. 20507.

[85] Putra R.P., Lee Y.S., Oh J.Y., Tien L.M., Kang W.N., Miyanaga T., Kang B., (2022), "Correlation between T and local structure of MgB2 with ZnO buffer layer: X-ray absorption fine structure study", *Physica B Condens. Matter* 645p. 414234.

[86] Putra R.P., Oh J.-Y., Angga Anugrah M., Miyanaga T., Kang B., (2024), "Evidence of disordered local structure of ZnO buffered MgB2 films via polarized extended X-ray absorption fine structure analysis", *Appl. Surf. Sci.* 663p. 160210.

[87] Sai Srikanth A., Muralidhar M., Sunsanee P., Jirsa M., Sakai N., Oka T., Murakami M., (2020), "Optimization of Carbon Encapsulated Boron Doping for High-Performance Bulk Sintered MgB2", *Adv. Eng. Mater.* 22(11), .

[88] Sandu V., Craciun L., Ionescu A.M., Aldica G., Miu L., Kuncser A., (2016), "Superconductivity in MgB 2 irradiated with energetic protons", *Physica C: Superconductivity and its Applications* 528pp. 27–34.

[89] Sandu V., Craciun L., Ionescu A.M., Aldica G., Miu L., Kuncser A., (2016), "Superconductivity in MgB 2 irradiated with energetic protons", *Physica C: Superconductivity and its Applications* 528pp. 27–34.

[90] Sekkina M.M.A., Elsabawy K.M., (2002), "Two dimensional γ-irradiations for promoted structural properties of MgB2 superconductors", *Physica C Supercond.* 377(4), pp. 411–415.

[91] Serquis A., Serrano G., Moreno S.M., Civale L., Maiorov B., Balakirev F., Jaime M., (2007), "Correlated enhancement of Hc2 and Jc in carbon nanotube doped MgB2", *Supercond. Sci. Technol.* 20(4), pp. L12–L15.

[92] Shadab M., Miryala M., (2024), "Tuning grain boundaries in MgB2 through boron ultra-sonication in 1-heptanol", *Ceram. Int.* 50(13), pp. 22266–22277.

[93] Shi Z.X., Pradhan A.K., Tokunaga M., Yamazaki K., Tamegai T., Takano Y., Togano K., Kito H., Ihara H., (2003), "Flux-pinning properties of single crystalline and dense polycrystalline MgB2", *Phys. Rev. B* 68(10), p. 104514.

[94] Shigeta I., Abiru T., Abe K., Nishida A., Matsumoto Y., (2003), "Temperature and field dependence of magnetization of MgB2 polycrystals", *Physica C Supercond.* 392–396pp. 359–363.

[95] Sudesh, Kumar N., Das S., Bernhard C., Varma G.D., (2013), "Effect of graphene oxide doping on superconducting properties of bulk MgB2", *Supercond. Sci. Technol.* 26(9), p. 095008.

[96] Susner M.A., Sumption M.D., Takase A., Collings E.W., (2014), "Evidence for Zr site-substitution for Mg in PLD-deposited MgB2 thin films", *Supercond. Sci. Technol.* 27(7), p. 75009.

[97] Szabó P., Samuely P., Kačmarčík J., Klein T., Marcus J., Fruchart D., Miraglia S., Marcenat C., Jansen A.G.M., (2001), "Evidence for Two Superconducting Energy Gaps in MgB2 by Point-Contact Spectroscopy", *Phys. Rev. Lett.* 87(13), p. 137005.

[98] Takenobu T., Ito T., Chi D.H., Prassides K., Iwasa Y., (2001), "Intralayer carbon substitution in the MgB2 superconductor", *Phys. Rev. B* 64(13), p. 134513.

[99] Tarantini C., Aebersold H.U., Braccini V., Celentano G., Ferdeghini C., Ferrando V., Gambardella U., Gatti F., Lehmann E., Manfrinetti P., Marré D., Palenzona A., Pallecchi I., Sheikin I., Siri A.S., Putti M., (2006), "Effects of neutron irradiation on polycrystalline MgB2", *Phys. Rev. B* 73(13), p. 134518.

[100] Tomsic M., Rindfleisch M., Yue J., McFadden K., Doll D., Phillips J., Sumption M.D., Bhatia M., Bohnenstiehl S., Collings E.W., (2007), "Development of magnesium diboride (MgB2) wires and magnets using in situ strand fabrication method", *Physica C Supercond.* 456(1–2), pp. 203–208.

[101] Tran D.T., Le T., Lee H.G., Park T., Nghia N.T., Hoa B.T., Tran D.H., Kang W.N., Hwang J., (2024), "Infrared spectroscopic study on Nb-ion-irradiated MgB2 thin films", *Current Applied Physics* 66pp. 30–34.

[102] Tran D.T., Le T., Seo Y.-S., Tran D.H., Park T., Jung S.-G., Miyanaga T., Kim C., Yeo S., Kang W.N., Hwang J., (2023), "Roles of Fe-ion irradiation on MgB2 thin films: Structural, superconducting, and optical properties", *J. Alloys Compd.* 968p. 172144.

[103] Vajpayee A., Jha R., Srivastava A.K., Kishan H., Tropeano M., Ferdeghini C., Awana V.P.S., (2011), "The effect of synthesis temperature on the superconducting properties of n-SiC added bulk MgB2 superconductor", *Supercond. Sci. Technol.* 24(4), p. 045013.

[104] Vinod K., Kumar R.G.A., Syamaprasad U., (2007), "Prospects for MgB2 superconductors for magnet application", *Supercond. Sci. Technol.* 20(1), pp. R1–R13.

[105] Wang J., Zhuang C.G., Li J., Wang Y.Z., Feng Q.R., Zheng D.N., (2009), "Upper critical field and Raman spectra of MgB2 thin films irradiated with low energy oxygen ion", *J. Appl. Phys.* 106(9), .

[106] Wang J., Zhuang C.G., Li J., Wang Y.Z., Feng Q.R., Zheng D.N., (2009), "Upper critical field and Raman spectra of MgB2 thin films irradiated with low energy oxygen ion", *J. Appl. Phys.* 106(9), .

[107] Wang J., Zhuang C.G., Li J., Wu Z.W., Li S., Chu H.F., Feng Q.R., Zheng D.N., (2009), "Enhancement of critical current density and flux pinning in oxygen ion-irradiated MgB2 thin films", *Supercond. Sci. Technol.* 22(4), p. 045020.

[108] Wang Y., Bouquet F. d ric, Sheikin I., Toulemonde P., Revaz B., Eisterer M., Weber H.W., Hinderer J., Junod A., (2003), "Specific heat of MgB2 after irradiation", *Journal of Physics: Condensed Matter* 15(6), pp. 883–893.

[109] Williamson G.K., Hall W.H., (1953), "X-ray line broadening from filed aluminium and wolfram", *Acta Metallurgica* 1(1), pp. 22–31.

[110] Xi X.X., Pogrebnyakov A. V, Zeng X.H., Redwing J.M., Xu S.Y., Li Q., Liu Z.-K., Lettieri J., Vaithyanathan V., Schlom D.G., Christen H.M., Zhai H.Y., Goyal A., (2004), "Progress in the deposition of MgB2 thin films", *Supercond. Sci. Technol.* 17(5), pp. S196–S201.

[111] Xi X.X., Pogrebnyakov A.V., Xu S.Y., Chen K., Cui Y., Maertz E.C., Zhuang C.G., Li Q., Lamborn D.R., Redwing J.M., Liu Z.K., Soukiassian A., Schlom D.G., Weng X.J., Dickey E.C., Chen Y.B., Tian W., Pan X.Q., Cybart S.A., Dynes R.C., (2007), "MgB2 thin films by hybrid physical–chemical vapor deposition", *Physica C Supercond.* 456(1–2), pp. 22–37.

[112] Yamamoto A., Shimoyama J., Ueda S., Iwayama I., Horii S., Kishio K., (2005), "Effects of B4C doping on critical current properties of MgB2 superconductor", *Supercond. Sci. Technol.* 18(10), pp. 1323–1328.

[113] Yamazaki K., Naito M., (2013), "Deteriorated superconductivity of MgB2 films due to Al diffusion from Al2O3 substrates: Thermodynamic perspective", *Physica C Supercond.* 495pp. 84–87.

[114] Yates K.A., Burnell, Stelmashenko N.A., Kang D.-J., Lee H.N., Oh B., Blamire M.G., (2003), "Disorder-induced collapse of the electron-phonon coupling in MgB2 observed by Raman spectroscopy", *Phys. Rev. B* 68(22), p. 220512.

[115] Yildirim T., Gülseren O., Lynn J.W., Brown C.M., Udovic T.J., Huang Q., Rogado N., Regan K.A., Hayward M.A., Slusky J.S., He T., Haas M.K., Khalifah P., Inumaru K., Cava R.J., (2001), "Giant Anharmonicity and Nonlinear Electron-Phonon Coupling in MgB2 : A Combined First-Principles Calculation and Neutron Scattering Study", *Phys. Rev. Lett.* 87(3), p. 37001.

[116] Ziegler J.F., Biersack J.P., (1985), "The Stopping and Range of Ions in Matter", , *Treatise on Heavy-Ion Science*, Springer US, pp. 93–129.

[117] Ziegler J.F., Ziegler M.D., Biersack J.P., (2010), "SRIM – The stopping and range of ions in matter (2010)", *Nucl. Instrum. Methods Phys. Res. B* 268(11–12), pp. 1818–1823.